LOW-ANGLE AND BRILLOUIN LIGHT SCATTERING FROM INHOMOGENEOUS AMORPHOUS POLYMERS

Thesis for the Degree of Ph. D.
MICHIGAN STATE UNIVERSITY
HENRY KWAI-TO YUEN
1973

This is to certify that the

thesis entitled

Low-Angle and Brillouin Light Scattering From Inhomogeneous Amorphous Polymers

presented by

Henry Kwai-To Yuen

has been accepted towards fulfillment of the requirements for

Ph.D. degree in Chemistry

Jack B. Kinsinger

Major professor

Date January 5, 1973

O-7639

ABSTRACT

LOW-ANGLE AND BRILLOUIN LIGHT SCATTERING
FROM INHOMOGENEOUS AMORPHOUS POLYMERS

By

Henry Kwai-To Yuen

The scattering of light by amorphous polymethyl methacrylate and a series of its blends with amorphous polystyrene in the concentration range from 0.0001% to 0.05% has been studied photometrically as a function of scattering angle. The theory and principles originally developed by Debye and Beuche and later extended by Ross in characterizing the inhomogeneity in isotropic solids have been reviewed. The correlation function, and hence the correlation distance, the distance of heterogeneity, the volume of heterogeneity and the fractional contribution factor of the correlation function are determined from the angular distribution of the scattered radiation in each sample. By measuring the turbidity of the sample, the amplitude of the inhomogeneity as represented by the standard deviation of the refractive index is obtained as well.

The results indicate that the correlation distances are of macro size. The Debye exponential correlation function which characterizes the polymethyl methacrylate cannot

adequately describe the short-range inhomogeneity of all the blends under study. In accord with the visual opacity of the samples, the experiment also provides quantitative information on the compatibility of the blend systems. As predicted by theory, the amplitude of the inhomogeneity is found to increase with the concentration of polystyrene in the blend.

The spectral distribution of the scattered light from the samples is also investigated at a scattering angle of 90^0 by Brillouin Spectroscopy. Measurements on the Brillouin shifts and half widths indicate that the hypersonic waves of frequency in the region of 10^{10} Hz in the samples propagate and attenuate independently of the polystyrene concentration. The Landau-Placzek ratios are, however, different among the samples and are large in magnitude. The dependence of the ratio on the inhomogeneity of the sample is apparent from the results. Furthermore, the sensitivity of the ratio to structural changes is also illustrated by its gigantic value associated with the blend where phase separation is believed to have occurred. The determination of the depolarization ratio, ρ_v, from the polarized and depolarized Brillouin spectra indicates that the samples have a very high degree of molecular isotropy.

LOW-ANGLE AND BRILLOUIN LIGHT SCATTERING FROM INHOMOGENEOUS AMORPHOUS POLYMERS

By

Henry Kwai-To Yuen

A THESIS

Submitted to
Michigan State University
in partial fulfillment of the requirements
for the degree of

DOCTOR OF PHILOSOPHY

Department of Chemistry

1973

To My Father

Mr. Yun-Sum Yuen

ACKNOWLEDGMENTS

The author wishes to express his appreciation to Professor J. B. Kinsinger for his guidance, encouragement and patience during the course of this study.

Appreciation is also extended to Richard Liedtke, William Toth, Jr. and Douglas Nordhaus for their helpful discussions and assistance.

The financial support of the Chemistry Department, Michigan State University is greatly appreciated.

The author is particularly grateful to his wife, Ruby, for her constant encouragement and understanding.

TABLE OF CONTENTS

TABLE OF CONTENTS (Cont.)

LIST OF TABLES

LIST OF FIGURES

LIST OF FIGURES (Cont.)

LIST OF FIGURES (Cont.)

CHAPTER I

INTRODUCTION

General

The history of light scattering begins with the attempt to understand the blue hue present in the sky. As early as 1500, da Vinci, although he failed to explain it correctly, had attributed it to the "particles of moisture which catch the rays of the sun". It was not until 1869, when John Tyndall[1] obtained a "blue sky" by passing a beam of white light through an aerosol mixture of butyl nitrite and hydrochloric acid, before it was realized that light scattering was an ubiguitous natural phenomenon. From 1871, the"Tyndall effect" was the basis for the great body of original theoretical work by Lord Rayleigh.[2,3] His first and second formalisms developed from the principles of the elastic theory of light and electromagnetic theory respectively have, ever since, formed the foundation for modern light scattering studies.

To-day, light scattering is divided into two disciplines[4]: the study of the scattered intensity (photometry) as a function of the scattering angle and wavelength, and the study of the spectral distribution of the scattered

radiation (spectrophotometry). The former differs from the latter in that it does not take into account the modulation of the scattered light as a result of the time variation of the optical properties of the medium. It is, therefore, generally applied to the investigation of the static properties, such as size, shape and molecular structure of the medium. The study of the spectral distribution of the scattered radiation was rendered possible only recently with the development of the gas laser and the highly sophisticated improvement in interferometry and electronics.

It is now understood that the radiation scattered off a medium, the so-called Rayleigh inelastic scattering, is, in fact, composed of three components, each of which is characterized by a different frequency:

1) The center-unshifted component -- This highly polarized component[5] is generally referred to as the Rayleigh line and is the result of the completely elastic scattering off the medium. It has the same frequency as the exciting radiation, and is usually tall and narrow (~ 0.01 cm^{-1}), but can be broadened by low frequency motional and diffusional processes.

2) The two frequency shifted side components -- These two components are situated symmetrically on both sides of the Rayleigh line in the gigahertz region. They are called the Brillouin lines and when resulting from vertically polarized incident radiation they are completely vertically polarized.[5] They arise as a result of the Doppler effect on the incident radiation due to the propagating sonic waves

(isentropic pressure fluctuations) present in the medium. Spectral distribution studies deal with two closely related but somewhat separated phenomena.[4] The first concerns with the broadening of the Rayleigh line upon scattering. This type of measurement reveals the molecular motions, such as rotational and translational diffusion of the particles of the medium. The second aspect deals exclusively with the location and peak width of the Brillouin lines and is generally called the Brillouin scattering. We shall see in a later chapter that such measurements enable the determinations of the velocity and attenuation of the hypersonic waves in the medium.

Purpose of Research

It is apparent that light scattering is indeed a powerful tool for the study of molecular properties of matter. A survey of the published literature shows that research activities in the area of light scattering by macromolecules are, for most part, limited to solutions and highly crystalline polymers, and only very few have been concerned with the amorphous state. It is, thus, believed that a light scattering study in amorphous solid polymers will not only serve as a bridge to the present molecular knowledge of macromolecules but also as a means for understanding this state of matter better. This is exactly the purpose of this dissertation.

CHAPTER II

THEORY OF LIGHT SCATTERING IN INHOMOGENEOUS MEDIA

Introduction

When a beam of light falls on a medium, it may either be transmitted with negligible attenuation in intensity or scattered in all directions. The former is the case if and only if the medium is perfectly uniform. Should it possess some kind of optical inhomogeneity either as a result of the presence of impurities or small scale density fluctuations, the latter will always happen. Thus, the scattered radiation is an information carrier of the optical properties or molecular structure of the medium.

In general, the optical properties of a medium can depend either on the mean value of the molecular parameters of the medium or their local deviations from the mean, namely the degree of inhomogeneity. The phenomenon of light scattering is associated completely with the latter kind of optical properties and hence, a discussion on how they may be characterized is necessary prior to the treatment of the scattering problem itself.

Concept of Inhomogeneity

Following Ross,[6] we represent the inhomogeneous medium as a perturbed continuum over its homogeneous analog and assume that it is non-conductive and has a constant magnetic permeability different from that for vacuum by a negligible amount. Then, the only macroscopic parameter which, by virtue of its inhomogeneity, will affect the propagation of light through the medium is the electric permittivity, ϵ (or dielectric constant). We shall further assume that the medium is constant with time. In this case, the electric permittivity is a continuous function only of position.

Let each point P_i inside the medium be defined by its position vector $\bar{r}_i$ from an arbitrary origin 0 in the sample such that

$$\bar{r}_i = \overline{OP}_i \ . \qquad (2.1)$$

Then, the electric permittivity at any point inside the medium is:

$$\epsilon(P_i) = \epsilon(\bar{r}_i) \ . \qquad (2.2)$$

We can define the mean permittivity of the medium (i.e. the permittivity for its idealized homogeneous analog) by:

$$\langle\epsilon\rangle = \frac{1}{V}\iiint_V \epsilon(\bar{r}_i)dV \ , \qquad (2.3)$$

where V is the volume (or rather the illuminated volume when dealing with light scattering) of the medium; and the

respective local deviation at each point by :

$$\delta\epsilon(P_i) = \delta\epsilon(\bar{r}_i) = \epsilon(\bar{r}_i) - \langle\epsilon\rangle \ . \qquad (2.4)$$

The inhomogeneity can be characterized by its amplitude and extent. The amplitude is given by the magnitude of the mean square deviations, or variance:

$$\langle\delta\epsilon^2\rangle = \frac{1}{V}\iiint_V [\epsilon(\bar{r}_i) - \langle\epsilon\rangle]^2 dV \ . \qquad (2.5)$$

The extent is the distance over which the deviation can be regarded not changing appreciably. Usually, the extent of the inhomogeneity is expressed by the covariance function at two points:

$$F'(\bar{r}_i,\bar{r}_j) = \frac{1}{V}\iiint_V [\epsilon(\bar{r}_i) - \langle\epsilon\rangle][\epsilon(\bar{r}_j) - \langle\epsilon\rangle]dV$$

or (2.6)

$$F'(\bar{r}_i,\bar{\rho}) = \frac{1}{V}\iiint_V [\epsilon(\bar{r}_i) - \langle\epsilon\rangle][\epsilon(\bar{r}_i + \bar{\rho}) - \langle\epsilon\rangle]dV,$$

where $\epsilon(\bar{r}_i)$ and $\epsilon(\bar{r}_j)$ are the permittivities at any two points, P_i and P_j, situated inside the medium at a distance

$$\bar{\rho} = \bar{r}_j - \bar{r}_i \qquad (2.7)$$

apart.

We shall consider only the case when the local deviations $\delta\epsilon$ are homogeneous or the mean permittivity is a constant and not a function of position. This condition, which in essence is the analog of the stationarity condition (i.e. all ensemble averages are independent of the origin of time) for time dependent processes, reduces the

covariance function at two points to be dependent only on the oriented distance between them and not on the distance to the origin. Hence, the covariance function becomes a function of $\overline{\rho}$. Using equation (2.2), we can rewrite equation (2.6) as:

$$F'(\overline{\rho}) = \frac{1}{V}\iiint_V \delta\epsilon(\overline{r}_i)\,\delta\epsilon(\overline{r}_i+\overline{\rho})\,dV. \qquad (2.8)$$

It is clear that $F'(\overline{\rho})$ is a measure of the interdependence between the deviations from the mean permittivity at two points. When the points are very remote from one another, the respective deviations of the permittivity, $\delta\epsilon(\overline{r}_i)$ and $\delta\epsilon(\overline{r}_j)$, are independent of each other and therefore, the covariance function as given in equation (2.8) vanishes, i.e.

$$\lim_{\overline{\rho}\to\infty} F'(\overline{\rho}) = 0. \qquad (2.9)$$

Similarly, it can easily be seen that $F'(\overline{\rho})$ will have its maximum value at $\overline{\rho} = 0$.

In practice, the covariance function is normalized with respect to its value at $\overline{\rho} = 0$:

$$F(\overline{\rho}) = \frac{F'(\overline{\rho})}{F'(0)}$$

or

$$F(\overline{\rho}) = \frac{\frac{1}{V}\iiint_V \delta\epsilon(\overline{r}_i)\,\delta\epsilon(\overline{r}_i+\overline{\rho})\,dV}{\langle\delta\epsilon^2\rangle}. \qquad (2.10)$$

The resulting function, $F(\overline{\rho})$, is called the autocorrelation or correlation function.

We see immediately from the Schwartz inequality that $|F(\overline{\rho})| \leq 1$, where the equal sign applied to $|F(0)|$.

The concept of the correlation function was first introduced by Zernike[7] in 1916. Later, Wiener[8] and Khintchine[9] showed that the correlation function of a real process was always a positive-definite function and vice versa -- this means that in the one-dimensional case the correlation function, $F(\rho)$, can be expressed in the following form:

$$F(\rho) = \frac{1}{2\pi} \int_{-\infty}^{\infty} \exp(i\eta\rho)\, dG(\eta)$$

or

$$F(\rho) = \frac{1}{2\pi} \int_{-\infty}^{\infty} \exp(i\eta\rho) J(\eta)\, d\eta \ ;$$

if $F(\rho)$ is also real, then

$$F(\rho) = \frac{1}{2\pi} \int_{-\infty}^{\infty} \cos(\eta\rho) J(\eta)\, d\eta \ . \qquad (2.11)$$

Here, $J(\eta)$ is a positive function for all η and is known as the spectral density or the power spectrum. Thus, from equation (2.11), the power spectrum must be a Fourier transform of the correlation function.

As an example, let us consider the correlation function of an ideally disordered sample which exhibits the Markov property, i.e. in a given direction, the deviation in permittivity from the mean at a point $r + dr$, where $r > 0$ and $dr > 0$, depends only on the deviation at r but not on those preceeding r. Doob[10] has proven that a sample may have this property if and only if its correlation function at two points, $F(\bar{r}_i, \bar{r}_k)$, satisfies the following relation:

$$F(r_i, r_k) = F(r_i, r_j)F(r_j, r_k) \quad ,$$

where

$$r_i \leq r_j \leq r_k \quad ,$$

or if $\rho_1 = r_j - r_i$ and $\rho_2 = r_k - r_j$,

$$F(\rho_1 + \rho_2) = F(\rho_1)F(\rho_2) \quad . \qquad (2.12)$$

The solution of equation (2.12) is obviously given by:

$$F(\rho) = \exp(-\rho/a) \quad , \qquad (2.13)$$

where $\rho = |\overline{\rho}| \geq 0$.

The parameter a in equation (2.13) has the dimension of distance and is given the name "correlation distance". It is always positive in value and is equal to the distance ρ at which the value of the correlation function, $F(\rho)$, attenuates to 1/e. Thus, in effect, a measures the extent (i.e. range or distance) of the inhomogeneity present in the sample. The larger the value of a, the more inhomogeneous is the sample and vice versa.

Light Scattering Theory

The classical theory of light scattering in isotropic inhomogeneous media was first formulated by Debye and Beuche[11] in 1949. Since then, the theory has been supplemented with more details by Guinier and Fournet.[12] Recently, Ross[6] has redeveloped the theory by using a slightly different approach. His treatment is so explicit and elegant that we choose to review it as follows.

Let us consider a monochromatic, plane electromagnetic wave incident normally on a block of inhomogeneous material of length ℓ which has a constant magnetic permeability different from that for vacuum by a negligible amount, zero conductivity and a mean permittivity $\langle\epsilon\rangle$. If the incident beam has a cross section A_0, then the illuminated volume inside the sample will be $A_0\ell$. For simplicity, let us assume the permittivity, $\epsilon(\bar{r})$, is just a random function of position only and not of time so that we can ignore any possible frequency fluctuations and changes in the resultant scattered field. We also assume that the interaction of the electromagnetic wave with the medium is so weak that the Born (or Rayleigh-Debye) approximation is valid.

The plane incident beam has an electric vector,

$$\bar{E} = \bar{E}_0 \exp(-i\omega t) \tag{2.14a}$$

and a magnetic vector,

$$\bar{H} = \bar{H}_0 \exp(-i\omega t) \tag{2.14b}$$

which must satisfy the Maxwell equations for a classical field, namely:

$$\nabla \times \bar{E} + \frac{1}{c}\dot{\bar{B}} = 0 \tag{2.15a}$$

$$\nabla \times \bar{H} - \frac{1}{c}\dot{\bar{D}} = \frac{4\pi}{c}\bar{j} \tag{2.15b}$$

$$\nabla \cdot \bar{D} = 4\pi d \tag{2.15c}$$

$$\nabla \cdot \bar{B} = 0 \quad , \tag{2.15d}$$

where c is the velocity of light in vacuum, $\dot{\bar{B}}$ and $\dot{\bar{D}}$ are the first time derivatives of the magnetic induction and electric displacement respectively, $\bar{j}$ is the electric current density and d is the electric charge density. Since the medium under consideration is non-conductive and is free from any electric charges,

$$\bar{j} = 0$$

and

$$d = 0 \ . \qquad (2.16)$$

With the help of the constitutive relations:

$$\bar{D} = \epsilon\bar{E}$$

$$\bar{B} = \mu\bar{H} \ , \qquad (2.17)$$

where ϵ is the permittivity and μ is the magnetic permeability, and equations (2.16) and (2.14 a and b) we can write the Maxwell equations (2.15 a, b and c) for the electric and magnetic field at any point $\bar{r}$ inside the illuminated volume of the medium as follows:

$$\nabla \times \bar{E}(\bar{r}) = \frac{i\omega}{c} \mu\bar{H}(\bar{r}) \qquad (2.18a)$$

$$\nabla \times \bar{H}(\bar{r}) = - \frac{i\omega}{c} \epsilon(\bar{r})\bar{E}(\bar{r}) \qquad (2.18b)$$

$$\nabla \cdot \epsilon(\bar{r})\bar{E}(\bar{r}) = 0 \ . \qquad (2.18c)$$

Equation (2.18c) can be simplified by using the well known vector identity of the divergence of the product of a scalar and a vector to:

$$\nabla \cdot \bar{E}(\bar{r}) = -\bar{E}(\bar{r}) \cdot \frac{\nabla\epsilon(\bar{r})}{\epsilon(\bar{r})} \ . \qquad (2.19)$$

Taking the curl on both sides of equation (2.18a) and substituting $\nabla \times \bar{H}(\bar{r})$ from (2.18b), we obtain:

$$\nabla \times \nabla \times \bar{E}(\bar{r}) = \frac{\omega^2 \mu \epsilon(\bar{r})}{c^2} \bar{E}(\bar{r}) \ . \qquad (2.20)$$

But,

$$\nabla \times \nabla \times \bar{E}(\bar{r}) = \nabla(\nabla \cdot \bar{E}(\bar{r})) - \nabla \cdot \nabla \bar{E}(\bar{r}) =$$

$$\nabla(\nabla \cdot \bar{E}(\bar{r})) - \nabla^2 \bar{E}(\bar{r}) \ , \qquad (2.21)$$

therefore, equation (2.20) can also be written as:

$$\nabla(\nabla \cdot \bar{E}(\bar{r})) - \nabla^2 \bar{E}(\bar{r}) = \frac{\omega^2 \mu \epsilon(\bar{r})}{c^2} \bar{E}(\bar{r}) \ ,$$

or with the help of equation (2.19),

$$\nabla^2 \bar{E}(\bar{r}) + \frac{\omega^2 \mu \epsilon(\bar{r})}{c^2} \bar{E}(\bar{r}) = -\nabla[\bar{E}(\bar{r}) \cdot \frac{\nabla \epsilon(\bar{r})}{\epsilon(\bar{r})}] =$$

$$-\nabla[\bar{E}(\bar{r}) \cdot \nabla \ln \epsilon(\bar{r})] \ . \qquad (2.22)$$

Equation (2.22) can be combined with equation (2.4),

$$\epsilon(\bar{r}) = \langle \epsilon \rangle + \delta\epsilon(\bar{r}) \ ,$$

to yield

$$\nabla^2 \bar{E}(\bar{r}) + \langle k \rangle^2 \bar{E}(\bar{r}) = -\langle k \rangle^2 \frac{\delta \epsilon(\bar{r})}{\langle \epsilon \rangle} \bar{E}(\bar{r}) -$$

$$\nabla\{\bar{E}(\bar{r}) \cdot \nabla \ln[\langle \epsilon \rangle + \delta\epsilon(\bar{r})]\}, \qquad (2.23)$$

where

$$\langle k \rangle = \frac{\omega}{c} \sqrt{\mu \langle \epsilon \rangle} = \frac{2\pi}{\langle \lambda \rangle} = \frac{2\pi}{\lambda_0} \langle n \rangle$$

is the mean wavenumber in the medium which has a mean refractive index $\langle n \rangle$; λ_0 is the wavelength of the electromagnetic field in vacuum, and $\langle \lambda \rangle$ is the mean wavelength in the medium.

Equation (2.23) is the wave equation that we must solve to obtain the scattered field, $\bar{E}(\bar{L})$, at the observation point specified by the position vector $\bar{L}$. In passing, we want to point out the fallacy that many authors have made in dealing with equation (2.23). Authors like Stratton[13], Wheelon[14] and Hoffmann[15] suggested that the last term in equation (2.23), namely

$$\nabla\{\bar{E}(\bar{r}) \cdot \nabla \ln[\langle\epsilon\rangle + \delta\epsilon(\bar{r})]\}$$

could be ignored if the changes in $[\frac{\delta\epsilon(\bar{r})}{\langle\epsilon\rangle}]$ are small over a wavelength, or if

$$\lambda\left|\nabla \frac{\delta\epsilon(\bar{r})}{\langle\epsilon\rangle}\right| << 1 \ .$$

This in fact is not correct, for, as we shall see soon, this term will cancel the longitudinal component of the scattered electromagnetic field and so maintain the transversality of the scattered electric and magnetic vectors to the plane of propagation.

We recognize that the wave equation in (2.23) is an inhomogeneous vector Helmholtz equation of the form:

$$\mathcal{L}\bar{E}(\bar{r}) = \gamma(\bar{r}) \ , \qquad (2.24a)$$

where $\mathcal{L}$ is the Helmholtz operator:

$$\mathcal{L} = \nabla^2 + \langle k\rangle^2 \ . \qquad (2.24b)$$

There are two methods by which equation (2.23) can be solved. The first method employs the perturbation approximation technique, while the second involves the application

of the Green dyadic. The latter method is mathematically more refined and is therefore used below.

The inhomogeneous Helmholtz equation (2.24) can be transformed to its integral counterpart (see Morse and Feshbach[16]) by a standard method to give:

$$\bar{E}_s(\bar{L}) = -\frac{1}{4\pi}\iiint_V G(\bar{L}|\bar{r}|\langle k\rangle)\gamma(\bar{r})dV \ , \qquad (2.25)$$

where $\bar{r}$ is any point in the illuminated volume V at which $\gamma(\bar{r})$ is assumed to be known and $G(\bar{L}|\bar{r}|\langle k\rangle)$ which is the Green dyadic or the vector analog of the Green function for scalar equations is given by:

$$G(\bar{L}|\bar{r}|\langle k\rangle) = \left[\frac{\exp(i\langle k\rangle|\bar{L}-\bar{r}|)}{|\bar{L}-\bar{r}|}\right] F \ . \qquad (2.26)$$

Here, F is the unit dyadic or the idemfactor such that

$$F\bar{v} = \bar{v}$$

is true for any vector $\bar{v}$.

Writing equation (2.25) for the wave equation (2.23), we get:

$$\bar{E}_s(\bar{L}) = \frac{\langle k\rangle^2}{4\pi\langle\epsilon\rangle}\iiint_V \frac{\exp(i\langle k\rangle|\bar{L}-\bar{r}|)}{|\bar{L}-\bar{r}|}\,\delta\epsilon(\bar{r})\bar{E}(\bar{r})dV + \qquad (2.27)$$

$$\frac{1}{4\pi}\iiint_V \frac{\exp(i\langle k\rangle|\bar{L}-\bar{r}|)}{|\bar{L}-\bar{r}|}\,\nabla\{\bar{E}(\bar{r})\cdot\nabla\ln[\langle\epsilon\rangle+\delta\epsilon(\bar{r})]\}dV .$$

To obtain the most general solution for equation (2.23), we must also add to equation (2.27) the solution of the homogeneous equation:

$$\nabla^2\bar{E}(\bar{r}) + \langle k\rangle^2\bar{E}(\bar{r}) = 0 \ ,$$

which, as can be easily obtained, is given by:

$$\bar{E}_h(\bar{L}) = \bar{E}_h(\bar{r}) = \bar{E}_0(\bar{r}) \exp(i\bar{k}\cdot\bar{r}) \ . \qquad (2.28)$$

Thus, the total electric field at the point of observation $\bar{L}$ is given by:

$$\bar{E}(\bar{L}) = \bar{E}_h(\bar{L}) + \frac{\langle k\rangle^2}{4\pi\langle\epsilon\rangle} \iiint_v \frac{\exp(i\langle k\rangle|\bar{L}-\bar{r}|)}{|\bar{L}-\bar{r}|} \delta\epsilon(\bar{r})\bar{E}(\bar{r})dV + \qquad (2.29)$$

$$\frac{1}{4\pi} \iiint_v \frac{\exp(i\langle k\rangle|\bar{L}-\bar{r}|)}{|\bar{L}-\bar{r}|} \nabla\{\bar{E}(\bar{r})\cdot\nabla\ln[\langle\epsilon\rangle+\delta\epsilon(\bar{r})]\}dV.$$

However, as can be seen from equation (2.28), $\bar{E}_h(\bar{L})$ is just the incident electric field at the point $\bar{r}$ inside the illuminated volume; it follows then the scattered electric field at $\bar{L}$ is only represented by $\bar{E}_s(\bar{L})$ shown in equation (2.27).

Let us assume the incident electric field which has a magnitude E_0 is travelling along the x direction specified by the unit vector $\bar{e}_x$ and further is polarized vertically along the z direction characterized by the unit vector $\bar{e}_z$. We can rewrite $\bar{E}_h(\bar{L})$ in equation (2.28) as follows:

$$\bar{E}_h(\bar{L}) = \bar{E}_h(\bar{r}) = E_0\bar{e}_z\cdot\exp(i\langle k\rangle\bar{e}_x\cdot\bar{r}) \ . \qquad (2.30)$$

To solve for $\bar{E}_s(\bar{L})$, we identify that equation (2.29) is a Fredholm equation of the second kind and therefore can be treated with the Liouville-Neumann method of successive substitution.[17] This method consists in continually substituting the value of $\bar{E}(\bar{L})$ for $\bar{E}(\bar{r})$ and adding the resulting terms together to obtain a series.

To obtain the first term of the series, let us replace $\bar{E}(\bar{r})$ in equation (2.29) by the value of $\bar{E}_h(\bar{r})$ given in equation (2.30). Thus,

$$\bar{E}(\bar{L}) = \bar{E}_h(\bar{L}) + \frac{E_0\langle k\rangle^2}{4\pi\langle\epsilon\rangle}\bar{e}_z\iiint_v \frac{\exp(i\langle k\rangle|\bar{L}-\bar{r}|)}{|\bar{L}-\bar{r}|}\,\delta\epsilon(\bar{r})\,\exp(i\langle k\rangle\bar{e}_x\cdot\bar{r})dV + \tag{2.31}$$

$$\frac{E_0}{4\pi}\iiint_v \frac{\exp(i\langle k\rangle|\bar{L}-\bar{r}|)}{|\bar{L}-\bar{r}|}\,\nabla\{\bar{e}_z\exp(i\langle k\rangle\bar{e}_x\cdot\bar{r})\cdot\nabla\ln[\langle\epsilon\rangle+\delta\epsilon(\bar{r})]\}dV.$$

We may substitute $\bar{E}(\bar{r})$ in equation (2.29) again with the above value for $\bar{E}(\bar{L})$ to obtain the second term of the series. But before we do that, let us expand the logarithmic term in equation (2.31) in a Taylor series as follows:

$$\ln[\langle\epsilon\rangle+\delta\epsilon(\bar{r})] = \ln\langle\epsilon\rangle + \frac{\delta\epsilon(\bar{r})}{\langle\epsilon\rangle} - \frac{[\delta\epsilon(\bar{r})^2]}{2\langle\epsilon\rangle^2} + \cdots . \tag{2.32}$$

Since we have assumed that the interaction between the incident field and the medium is weak, the deviation $\delta\epsilon(\bar{r})$ must be very much smaller than the mean permittivity $\langle\epsilon\rangle$, i.e.

$$\frac{\delta\epsilon(\bar{r})}{\langle\epsilon\rangle} << 1 . \tag{2.33}$$

In this case, it is obvious that terms higher than the second in equation (2.32) will contribute little and hence can be ignored. This is the well known Born (or Rayleigh-Debye) approximation -- if the scattering is weak, further scattering of the once scattered wave will be negligible.

Physically, the Born (or Rayleigh-Debye) approximation is equivalent to ignoring second and higher order scattering phenomena.

As $\nabla \ln\langle\epsilon\rangle = 0$, we obtain on substituting equation (2.32) into equation (2.31):

$$\bar{E}(\bar{L}) = \bar{E}_h(\bar{L}) + \frac{E_0\langle k\rangle^2}{4\pi\langle\epsilon\rangle}\bar{e}_z \iiint_v \frac{\exp(i\langle k\rangle|\bar{L}-\bar{r}|)}{|\bar{L}-\bar{r}|} d\epsilon(\bar{r}) \cdot \exp(i\langle k\rangle \bar{e}_x \cdot \bar{r}) dV + \tag{2.34}$$

$$\frac{E_0}{4\pi\langle\epsilon\rangle} \iiint_v \frac{\exp(i\langle k\rangle|\bar{L}-\bar{r}|)}{|\bar{L}-\bar{r}|} \nabla[\bar{e}_z \exp(i\langle k\rangle \bar{e}_x \cdot \bar{r}) \cdot \nabla\delta\epsilon(\bar{r})] dV .$$

Now, if we substitute equation (2.34) for $\bar{E}(\bar{r})$ in equation (2.29) to obtain the second term of the Liouville-Neumann series, we notice that it will be proportional to $[\frac{\delta\epsilon(\bar{r})}{\langle\epsilon\rangle}]^2$ and therefore can be disregarded.

In short, providing that the Born (or Rayleigh-Debye) approximation is valid, the scattered electric field at the observation point $\bar{L}$ is given by:

$$\bar{E}_s(\bar{L}) = \frac{E_0\langle k\rangle^2}{4\pi\langle\epsilon\rangle}\bar{e}_z \iiint_v \frac{\exp(i\langle k\rangle|\bar{L}-\bar{r}|)}{|\bar{L}-\bar{r}|} \delta\epsilon(\bar{r}) \exp(i\langle k\rangle \bar{e}_x \cdot \bar{r}) dV + \tag{2.35}$$

$$\frac{E_0}{4\pi\langle\epsilon\rangle} \iiint_v \frac{\exp(i\langle k\rangle|\bar{L}-\bar{r}|)}{|\bar{L}-\bar{r}|} \nabla[\bar{e}_z (i\langle k\rangle \bar{e}_x \cdot \bar{r}) \cdot \nabla\epsilon(\bar{r})] dV .$$

Applying the Gauss gradient theorem, (see e.g. G. Arfken,[18] p. 44), i.e. for any scalar functions u and v,

$$\iiint_v u\nabla v d\tau = \oint\!\!\oint_s uv d\sigma - \iiint_V v\nabla u d\tau ,$$

to the second integral in the above expression for $\bar{E}_s(\bar{L})$, and noting that in our case the surface integral vanishes because the surface of integration can be moved beyond the limits of the illuminated volume V, we can reduce equation (2.35) to:

$$\bar{E}_s(\bar{L}) = \frac{E_0\langle k\rangle^2}{4\pi\langle\epsilon\rangle}\bar{e}_z\iiint_v \frac{\exp(i\langle k\rangle|\bar{L}-\bar{r}|)}{|\bar{L}-\bar{r}|}\delta\epsilon(r)\exp(i\langle k\rangle\bar{e}_x\cdot\bar{r})dV - \tag{2.36}$$

$$\frac{E_0}{4\pi\langle\epsilon\rangle}\iiint_v[\bar{e}_z\exp(i\langle k\rangle\bar{e}_x\cdot\bar{r})\cdot\nabla\delta\epsilon(\bar{r})]\nabla[\frac{\exp(i\langle k\rangle|\bar{L}-\bar{r}|)}{|\bar{L}-\bar{r}|}]dV.$$

Since in most practical cases, the observation point L is situated far beyond the small scattering volume V in the Fraunhofer region, we can also express $|\bar{L}-\bar{r}|$ in terms of r/L. In Figure 2.1, it is obvious that if $|\bar{r}| << |\bar{L}|$,

$$|\bar{L}-\bar{r}| \approx QL = |\bar{L}| - OQ = |\bar{L}| - |\bar{r}|\cos(\hat{\bar{r}}\hat{\bar{L}})$$

or

$$|\bar{L}-\bar{r}| \approx L(1-\frac{|\bar{r}|}{L}\frac{|\bar{L}|}{L}\cos(\hat{\bar{r}}\hat{\bar{L}}) = L(1-\frac{\bar{r}}{L}\cdot\frac{\bar{L}}{L}), \tag{2.37}$$

where $\hat{\bar{r}}\hat{\bar{L}}$ is the angle between $\bar{r}$ and $\bar{L}$ and $L = |\bar{L}| = OL$ is the distance from the medium to the observation point.

With $|\bar{L}-\bar{r}|$ given by equation (2.37), we can rewrite equation (2.36) as follows:

$$\bar{E}_s(\bar{L}) = \frac{E_0\langle k\rangle^2}{4\pi\langle\epsilon\rangle}\frac{\exp(i\langle k\rangle L)}{L}\bar{e}_z\iiint_v \exp[i\langle k\rangle(\bar{e}_x-\bar{e}_L)\cdot\bar{r}]\delta\epsilon(\bar{r})dV - \tag{2.38}$$

$$\frac{i\langle k\rangle E_0}{4\pi\langle\epsilon\rangle}\frac{\exp(i\langle k\rangle L)}{L}\bar{e}_L\iiint_v\{\bar{e}_z\exp[i\langle k\rangle(\bar{e}_x-\bar{e}_L)\cdot\bar{r}]\cdot\nabla\delta\epsilon(\bar{r})\}dV,$$

where $\bar{e}_L$ is the unit vector along $\bar{L}$.

The last integral in equation (2.38) can once more be simplified with the Gauss theorem, namely for a scalar function u and a vector $\bar{Q}$:

$$\iiint_v u\nabla\cdot\bar{Q}dv = \oiint_s u\bar{Q}\cdot d\bar{S} - \iiint_v \bar{Q}\cdot\nabla u dV .$$

The surface integral can again be ignored because the surface of integration can be moved beyond the limits of the irradiated volume V causing the integral to vanish. Hence, equation (2.38) becomes:

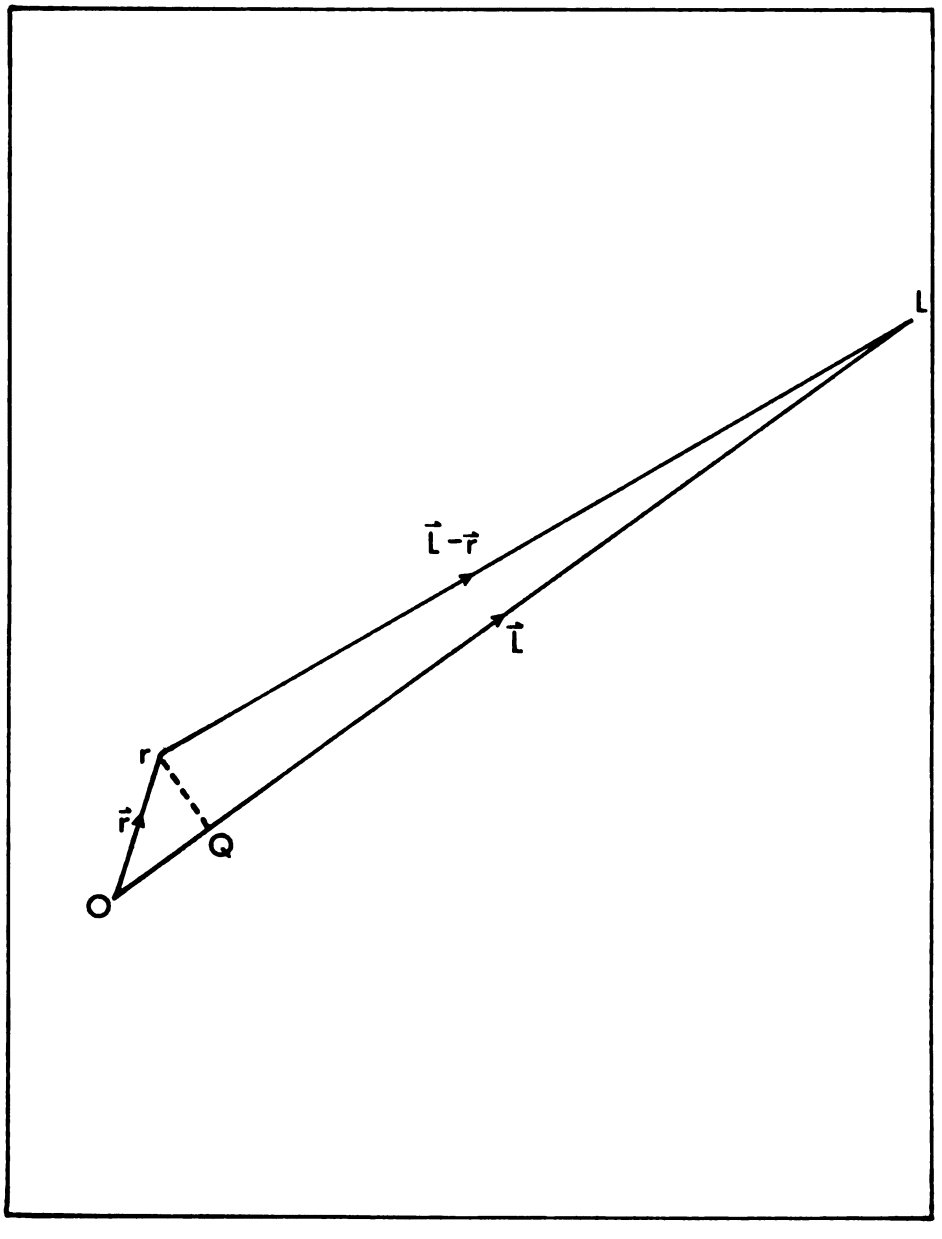

Figure 2.1. The vector diagram.

$$\bar{E}_s(\bar{L}) = E_s(L\bar{e}_L) = \frac{E_0\langle k\rangle^2}{4\pi\langle\epsilon\rangle}\frac{\exp(i\langle k\rangle L)}{L}\bar{e}_z\iiint_v \exp[i\langle k\rangle(\bar{e}_x-\bar{e}_L)\cdot\bar{r}]\,\delta\epsilon(\bar{r})dV$$

$$- \frac{E_0\langle k\rangle^2}{4\pi\langle\epsilon\rangle}\frac{\exp(i\langle k\rangle L)}{L}\bar{e}_L(\bar{e}_z\cdot\bar{e}_L)\iiint_v \exp[i\langle k\rangle(\bar{e}_x-\bar{e}_L)\cdot\bar{r}]\,\delta\epsilon(\bar{r})dV. \qquad (2.39)$$

However,

$$\bar{e}_L \times (\bar{e}_z \times \bar{e}_L) \equiv \bar{e}_z - \bar{e}_L(\bar{e}_L \cdot \bar{e}_z)$$

is a well known vector identity; therefore equation (2.39) reduces to the following final expression for the scattered electric field at the observation point $\bar{L}$:

$$\bar{E}_s(L\bar{e}_L) = \frac{E_0\langle k\rangle^2}{4\pi\langle\epsilon\rangle}\frac{\exp(i\langle k\rangle L)}{L}\bar{e}_L\times(\bar{e}_z\times\bar{e}_L)\iiint_v \exp(i\langle k\rangle\bar{s}\cdot\bar{r})\,\delta\epsilon(\bar{r})dV, \qquad (2.40)$$

where $\bar{s} = \bar{e}_x - \bar{e}_L$.

Equation (2.40) clearly indicates that except for a factor of proportionality, the instantaneous scattered electric field is the Fourier transform of the local deviation in permittivity from the mean. We, therefore, expect that the scattered light carries information about the inhomogeneity present in the medium.

In practice, the instantaneous electric field can never be measured. This is because the optical period of the field is of the magnitude of 10^{-15} second while the fastest photodetector only has a resolving time of about 10^{-10} second. However, most detectors can measure light intensity, i.e. the square of the modulus of the instantaneous field strength very accurately.

To obtain an expression for the scattered light intensity, it will be better to consider the entire scattered wave at the point of observation $\bar{L}$, i.e. also consider the magnetic field of the scattered wave at $\bar{L}$.

The first Maxwell equation shown in (2.18a) can be written in the following manner for the scattered electric and magnetic fields at $\bar{L}$:

$$\nabla \times \bar{E}_s(L\bar{e}_L) = (\bar{e}_L \frac{\partial}{\partial L}) \times \bar{E}_s(L\bar{e}_L) = \frac{i\omega}{c} \mu \bar{H}_s(L\bar{e}_L) \quad . \quad (2.41)$$

Substituting the value for $\bar{E}_s(L\bar{e}_L)$ given in equation (2.40) into the above expression, we obtain:

$$\bar{H}_s(L\bar{e}_L) = \frac{ic}{\mu\omega} \frac{E_0 \langle k \rangle^2}{4\pi \langle \epsilon \rangle} \bar{e}_L \times [\bar{e}_L \times (\bar{e}_z \times \bar{e}_L)] \iiint_v \exp(i\langle k \rangle \bar{s} \cdot \bar{r}) \delta\epsilon(\bar{r}) dV \cdot$$

$$\frac{\partial}{\partial L} \frac{\exp(i\langle k \rangle L)}{L} \quad . \quad (2.42)$$

But, for L very large,

$$\frac{\partial}{\partial L} \frac{\exp(i\langle k \rangle L)}{L} = i\langle k \rangle \frac{\exp(i\langle k \rangle L)}{L} - \frac{\exp(i\langle k \rangle L)}{L^2} \approx i\langle k \rangle \frac{\exp(i\langle k \rangle L)}{L} ;$$

therefore, with the help of the vector identity:

$$\bar{e}_L \times [\bar{e}_L \times (\bar{e}_z \times \bar{e}_L)] \equiv (\bar{e}_L \cdot \bar{e}_z)(\bar{e}_L \times \bar{e}_L) - (\bar{e}_L \cdot \bar{e}_L)(\bar{e}_L \times \bar{e}_z) = -(\bar{e}_L \times \bar{e}_z),$$

equation (2.42) reduces to:

$$\bar{H}_s(L\bar{e}_L) = \frac{H_0 \langle k \rangle^2}{4\pi \langle \epsilon \rangle} \frac{\exp(i\langle k \rangle L)}{L} (\bar{e}_L \times \bar{e}_z) \iiint_v \exp(i\langle k \rangle \bar{s} \cdot \bar{r}) \delta\epsilon(\bar{r}) dV, \quad (2.43)$$

where $H_0 = \frac{E_0 \langle k \rangle c}{\mu\omega}$ is the magnitude of the incident magnetic field.

Now, we can evaluate the Poynting vector $\langle\bar{S}\rangle$ of the scattered wave. By definition, $\langle\bar{S}\rangle$ represents the average amount of scattered light energy which crosses a unit area normal to $\bar{e}_L$ (i.e. its direction of propagation) at $\bar{L}$ and is given by:

$$\langle\bar{S}\rangle = \frac{\delta\Phi}{\delta A}\,\bar{e}_L = I_s(L\bar{e}_L)\bar{e}_L = \frac{c}{8\pi}\,\bar{E}_s(L\bar{e}_L)\times\bar{H}_s^*(L\bar{e}_L), \qquad (2.44)$$

where $I_s(L\bar{e}_L)$ is the scattered light intensity at $\bar{L}$ and $\bar{H}_s^*(L\bar{e}_L)$ is the complex conjugate of $\bar{H}_s(L\bar{e}_L)$.

Making the appropriate substitutions of $\bar{E}_s(L\bar{e}_L)$ and $\bar{H}_s^*(L\bar{e}_L)$ in equation (2.44) with equation (2.40) and the complex conjugate of equation (2.43) respectively:

$$\langle\bar{S}\rangle = I_s(L\bar{e}_L)\bar{e}_L = \frac{\langle k\rangle^4}{16\pi^2\langle\epsilon\rangle^2 L^2}\left(\frac{c}{8\pi}E_0H_0\right)[\bar{e}_L\times(\bar{e}_z\times\bar{e}_L)]\times(\bar{e}_L\times\bar{e}_z)\cdot$$

$$\iiint_{V_i}\iiint_{V_j}\delta\epsilon(\bar{r}_i)\delta\epsilon(\bar{r}_j)\exp(i\langle k\rangle\bar{s}\cdot\bar{r}_j)\exp(-i\langle k\rangle\bar{s}\cdot\bar{r}_i)\,dV_i\,dV_j. \qquad (2.45)$$

It can be seen from equation (2.44) that the first term in parentheses on the right hand side of the above expression is equal to the magnitude of the Poynting vector or the intensity of the incident electromagnetic wave, i.e.

$$\frac{c}{8\pi}\,E_0H_0 = |\langle\bar{S}_0\rangle| = I_0\ . \qquad (2.46)$$

Since,

$$[\bar{e}_L\times(\bar{e}_z\times\bar{e}_L)]\times(\bar{e}_L\times\bar{e}_z) = \bar{e}_L|\bar{e}_z\times\bar{e}_L|^2\ ,$$

it follows, therefore, from equations (2.45) and (2.46):

$$I_s(L\bar{e}_L) = \frac{\langle k\rangle^4 I_0}{16\pi\langle\epsilon\rangle^2 L^2} |\bar{e}_z \times \bar{e}_L|^2 \cdot$$

$$\iiint_{V_i}\iiint_{V_j} \delta\epsilon(\bar{r}_i)\delta\epsilon(\bar{r}_j)\exp(i\langle k\rangle\bar{s}\cdot\bar{r}_j)\exp(-i\langle k\rangle\bar{s}\cdot\bar{r}_i)dV_i dV_j,$$

or letting

$$\bar{\rho} = \bar{r}_j - \bar{r}_i$$

and realizing that

$$|\bar{e}_z \times \bar{e}_L|^2 = \sin^2\beta ,$$

where β is the angle between the direction of the incident electric field and the direction of observation, we obtain for vertically polarized incident light:

$$I_s(\beta) = \frac{\langle k\rangle^4 I_0}{16\pi^2\langle\epsilon\rangle^2 L^2} \sin^2\beta \iiint_{V_i} \exp(i\langle k\rangle\bar{s}\cdot\bar{\rho})dV_i \cdot \iiint_{V_j} \delta\epsilon(\bar{r}_i)\delta\epsilon(\bar{r}_j)dV_j . \qquad (2.47)$$

Substituting equation (2.10) for the last integral in equation (2.47), we obtain:

$$I_s(\beta) = I_0 \frac{V}{L^2} \frac{\langle k\rangle^4}{16\pi^2} \frac{\langle\delta\epsilon^2\rangle}{\langle\epsilon\rangle^2} \sin^2\beta \iiint_V F(\bar{\rho})\exp(i\langle k\rangle\bar{s}\cdot\bar{\rho})dV. \qquad (2.48)$$

Here V is the illuminated volume of the medium and $F(\bar{\rho})$ is the correlation function we discussed in the last section.

The volume integral of the correlation function in equation (2.48) can be reduced further if the deviations in permittivity from the mean, $\delta\epsilon(\bar{r})$, are isotropic. In this case, $F(\bar{\rho})$ is a function only of ρ, i.e.

$$F(\bar{\rho}) = F(\rho) \ ,$$

where $\rho = |\bar{\rho}|$, and spherical polar co-ordinates with the polar axis lying along $\bar{s}$ can be introduced. Letting the angle between $\bar{s}$ and $\bar{\rho}$ be γ, the volume integral becomes:

$$\iiint_V F(\bar{\rho}) \exp(i\langle k\rangle \bar{s}\cdot\bar{\rho}) dV = 2\pi \int_0^{\rho max} F(\rho)\rho^2 d\rho \cdot$$

$$\int_0^{\pi} \exp(i\langle k\rangle s\rho\cos\gamma)\sin\gamma \, d\gamma \ ,$$

or after performing the angular integration,

$$\iiint_V F(\bar{\rho}) \exp(i\langle k\rangle \bar{s}\cdot\bar{\rho}) dV = 4\pi \int_0^{\infty} \rho^2 F(\rho) \frac{\sin(\langle k\rangle \rho s)}{\langle k\rangle \rho s} \, d\rho. \quad (2.49)$$

Here, the upper limit of ρ is set equal to ∞ because $F(\rho)$ becomes negligibly small for ρ exceeding a certain value, and s is given by:

$$s = |\bar{s}| = |\bar{e}_x - \bar{e}_L| = 2\sin\left(\frac{\theta}{2}\right) , \qquad (2.49a)$$

where θ is the scattering angle or the angle between the direction of observation and that of propagation of the incident wave.

Taking equation (2.49) into account, we obtain from equation (2.48) the scattered light intensity from an isotropic inhomogeneous medium at a scattering angle θ:

$$I_s(\beta) = \left[I_0 \frac{V}{L^2} \frac{\langle k\rangle^3}{4\pi} \frac{\langle \delta\epsilon^2\rangle}{\langle \epsilon\rangle^2}\right] \frac{\sin^2\beta}{s} \int_0^{\infty} \rho F(\rho) \sin(\langle k\rangle \rho s) d\rho \ . \quad (2.50a)$$

If the point of observation $\bar{L}$ is restricted to lie on the xy plane, as it is usually the case when a photomultiplier tube is used to scan the scattered light intensity, $\sin^2\beta = |\bar{e}_z \times \bar{e}_L|^2$ is equal to unity. Hence,

$$I_s(s) = [I_0 \frac{V}{L^2} \frac{\langle k\rangle^3 \langle \delta\epsilon^2\rangle}{4\pi \langle \epsilon\rangle^2}] \frac{1}{s}\int_0^\infty \rho F(\rho)\sin(\langle k\rangle \rho s)d\rho \ . \quad (2.50b)$$

At this point, it is already obvious that the angular distribution of the scattered light intensity depends functionally on the correlation function $F(\rho)$ and the mean wavenumber $\langle k\rangle$. The magnitude of the variance in permittivity, $\langle \delta\epsilon^2\rangle$, however, cannot be extracted absolutely from the distribution, for with $I_s(s)$ being only the relative scattered intensity, the term in square bracket in equation (2.50b) represents just the expansion factor of the scale to which the intensity is recorded.

Taking a Fourier transform of $I_s(s)$ in equation (2.50b), we see:

$$F(\rho) = \frac{1}{\rho} \frac{8}{\langle k\rangle^2} \frac{L^2}{I_0 V} \frac{\langle \epsilon\rangle^2}{\langle \delta\epsilon^2\rangle} \int_0^\infty s I_s(s)\sin(\langle k\rangle \rho s)ds \ . \quad (2.51)$$

This implies that at least in principle the form of the correlation function and hence the value of the correlation distance a (see last section) can be determined from the angular distribution of the scattered light intensity measurement. But, from the experimental standpoint, this is not really true for s, which is defined in equation (2.49a), can have values only between 0 and 2 and not 0 and ∞ as indicated in equation (2.51). In fact, what we can determine in this fashion is only the function $T(\rho)$ which is defined as follows:

$$T(\rho) = \frac{1}{\rho} \frac{8}{\langle k\rangle^2} \frac{L^2}{I_0 V} \frac{\langle \epsilon\rangle^2}{\langle \delta\epsilon^2\rangle} \int_0^\infty s I_s(s) U(2-s)\sin(\langle k\rangle \rho s)ds \ , \quad (2.52)$$

where $U(2 - s)$ is the unit function:

$$U(2 - s) = \begin{cases} 1 , & \text{for } 0 \leq (2 - s) < 2 \\ 0 , & \text{for } (2 - s) < 0 . \end{cases}$$

Since the Fourier transform of $\frac{8}{\langle k \rangle^2} \frac{L^2}{I_0 V} \frac{\langle \epsilon \rangle^2}{\langle \delta\epsilon^2 \rangle} s I_s(s)$ is exactly equal to $\frac{2}{\pi}\rho F(\rho)$, we can also define a new function $D(\rho)$ such that $D(\rho)$ is the Fourier cosine transform of $U(2 - s)$, or

$$D(\rho) = \frac{2}{\pi} \frac{\sin(2\langle k \rangle \rho)}{\langle k \rangle \rho} .$$

Now, it follows from the convolution theorem that $T(\rho)$ is also given by:

$$T(\rho) = \frac{2}{\pi^2} \int_0^\infty F(\zeta)[D(|\rho-\zeta|) - D(\rho + \zeta)]d\zeta = \frac{2}{\pi^2} F * D . \tag{2.53}$$

Thus, strictly speaking, the true correlation function $F(\rho)$ of the medium can be determined experimentally only by deconvoluting the function $T(\rho)$ which we establish from the angular distribution of the scattered light intensity measurement.

Although, as we mentioned above, the variance in permittivity, $\langle \delta\epsilon^2 \rangle$, or the amplitude of the inhomogeneity of the medium cannot be obtained from the distribution of the relative scattered intensity, it can be estimated from a knowledge of the turbidity or the scattering coefficient of the sample.

Denoting the turbidity by τ, then by definition

$$\tau = \oint\!\!\oint R(\beta)d\Omega = \int_0^{\pi}\int_0^{2\pi}\frac{I_s(\beta)L^2}{I_0V}\sin\theta d\psi d\theta, \qquad (2.54)$$

where $R(\beta) = \frac{I_s(\beta)L^2}{I_0V}$ is called the Rayleigh ratio or the scattering cross section per unit volume, θ is the scattering angle (in this case, the polar angle) and ψ is the azimuthal angle measured from the y axis. Before we perform the angular integration, we notice that the term $\sin^2\beta$ in equation (2.50a) is related to θ and ψ by the following equation:

$$\sin^2\beta = 1 - \sin^2\theta\,\sin^2\psi\ . \qquad (2.55)$$

Substituting equation (2.50a) into equation (2.54) and taking equation (2.55) into account, we obtain after integrating over ψ and changing variable from θ to s:

$$\tau = \frac{\langle k\rangle^3}{2}\frac{\langle\delta\epsilon^2\rangle}{\langle\epsilon\rangle^2}\{\int_0^2[\int_0^{\infty}\rho F(\rho)\sin(\langle k\rangle\rho s)d\rho]ds -$$

$$\frac{1}{8}\int_0^2(4s^2 - s^4)[\int_0^{\infty}\rho F(\rho)\sin(\langle k\rangle\rho s)d\rho]ds\} \ . \qquad (2.56)$$

But, according to the Lambert law, the turbidity is also given by:

$$I(\ell) = I(0)\exp(-\tau\ell)\ ,$$

or

$$\tau = \frac{1}{\ell}\ln\frac{I(0)}{I(\ell)}\ , \qquad (2.57)$$

where $I(\ell)$ is the direct transmitted intensity (assuming no reflection on the surfaces of incidence and emergence) of the beam which has passed through the sample of thickness

ℓ, and $I(0)$ the intensity of the incident wave. Thus, knowing ℓ, the turbidity of the medium can be determined absolutely by measuring $I(\ell)$ and $I(0)$. Besides, if the correlation function, $F(\rho)$, and therefore, the value of the correlation distance, a, can also be established from the angular distribution of the scattered intensity, from equation (2.56) the determination of the permittivity variance, $\langle \delta\epsilon^2 \rangle$, is straight forward.

Most of the time, the more easily measured quantity: the refractive index, is used instead of the electric permittivity. The relation between the two quantities is given by the Maxwell formula:

$$n(\bar{r}) = \sqrt{\epsilon(\bar{r})\mu} \ ,$$

or for the medium under consideration which has a magnetic permeability different from that for vacuum by a negligible amount,

$$\epsilon(\bar{r}) = [n(\bar{r})]^2 = [\langle n \rangle + \delta n(\bar{r})]^2 \ , \qquad (2.58)$$

where $\delta n(\bar{r})$ is the deviation in refractive index from the mean at any point $\bar{r}$ inside the medium.

Since

$$\frac{\langle \delta\epsilon^2 \rangle}{\langle \epsilon \rangle^2} = \frac{\langle (\epsilon(\bar{r}) - \langle \epsilon \rangle)^2 \rangle}{\langle \epsilon \rangle^2} = \frac{\langle \epsilon^2 \rangle - \langle \epsilon \rangle^2}{\langle \epsilon \rangle^2}$$

and

$$\langle \delta n(\bar{r}) \rangle = \langle n(\bar{r}) - \langle n \rangle \rangle = 0 \ ,$$

taking equation (2.58) into account, we obtain:

$$\frac{\langle \delta\epsilon^2 \rangle}{\langle \epsilon \rangle^2} = \frac{4\langle n \rangle^2 \langle (\delta n)^2 \rangle + 4\langle n \rangle \langle (\delta n)^3 \rangle + \langle (\delta n)^4 \rangle - \langle (\delta n)^2 \rangle^2}{\langle n \rangle^4 + 2\langle n \rangle^2 \langle (\delta n)^2 \rangle + \langle (\delta n)^2 \rangle^2} \quad . \quad (2.59)$$

Within the framework of the Born approximation which we have assumed valid,

$$\frac{\delta n(\bar{r})}{\langle n \rangle} << 1 \quad ,$$

therefore, we can ignore the second and higher terms in the numerator and denominator in equation (2.59). It follows then

$$\frac{\langle \delta\epsilon^2 \rangle}{\langle \epsilon \rangle^2} \approx \frac{4\langle n \rangle^2 \langle (\delta n)^2 \rangle}{\langle n \rangle^4} = \frac{4\langle (\delta n)^2 \rangle}{\langle n \rangle^2} \quad . \quad (2.60)$$

We can also write equation (2.56) in the following way:

$$\frac{\langle \delta\epsilon^2 \rangle}{\langle \epsilon \rangle^2} = \frac{\tau}{\langle k \rangle J} = \frac{\tau \lambda_0}{2\pi \langle n \rangle J} \quad , \quad (2.61)$$

where λ_0 is the wavelength of the incident wave in vacuum and

$$J = \frac{\langle k \rangle^2}{2} \{ \int_0^2 [\int_0^\infty \rho F(\rho) \sin(\langle k \rangle \rho s) d\rho] ds -$$

$$\frac{1}{8} \int_0^2 (4s^2 - s^4) [\int_0^\infty \rho F(\rho) \sin(\langle k \rangle \rho s) d\rho] ds \} \quad . \quad (2.61a)$$

Substituting equation (2.60) into equation (2.61), we see

$$\langle (\delta n)^2 \rangle \approx \frac{\tau \lambda_0 \langle n \rangle}{8\pi J} \quad ,$$

or the standard deviation in refractive index of the medium,

$$\sqrt{\langle(\delta n)^2\rangle} \approx \sqrt{\frac{\tau\lambda_0\langle n\rangle}{8\pi J}} \ . \qquad (2.62)$$

Thus, having established the form of the correlation function, $F(\rho)$, and determined the value of the correlation distance, a, we can calculate the standard deviation in refractive index provided that we also know the turbidity and the mean refractive index of the medium.

Conclusion

From the above two sections, we conclude that the inhomogeneity in electric permittivity, ϵ, (or refractive index, n) of an isotropic medium which is non-conductive and has a constant magnetic permeability different from that for vacuum by a negligible amount can be characterized in amplitude by the variance, $\langle\delta\epsilon^2\rangle$ (or $\sqrt{\langle(\delta n)^2\rangle}$), and in extent by the correlation distance, a, given by the correlation function, $F(\rho)$.

Provided that the scattering of the medium is weak or the Born approximation is valid, the correlation function and hence the correlation distance can be established from the angular distribution of the scattered intensity from the medium. With the knowledge of the correlation distance, the amplitude of the inhomogeneity ($\langle\delta\epsilon^2\rangle$ or $\sqrt{\langle(\delta n)^2\rangle}$) can be determined by measuring the turbidity of the sample.

CHAPTER III

LIGHT SCATTERING FROM AMORPHOUS SOLID POLYBLENDS

Introduction

In recent years, multicomponent polymeric materials, commonly called polyblends, have become giant rivals in industry of their individual constituents, namely homopolymers. The impetus was first launched by the discovery of T. A. Grotenhuis[19] twenty-four years ago when he obtained a superflexible and abrasive resistant product by mixing a hard unmasticated rubber with an elastic rubber. Since then, interest in the area increases rapidly as more and more desirable blends, e.g. polystyrene latex with polybutadiene latex -- the high impact polystyrene, polyvinyl chloride with an elastomer such as chlorinated polyethylene, ABS, MBS or EVA and etc., were made and patented.

The physical and mechanical properties of polyblends depend greatly on the intimacy of the mixture of the parent polymers. The word "compatibility", which has its origin in the mixing of two liquids, is frequently used to describe this phenomenon. It is understood that liquids are compatible if on mixing they yield one homogeneous phase. This implies that compatibility is associated with

nearly complete mixing of the molecules at the molecular level. In view of their huge size and high viscosity in comparison to liquids, such intimate mixing definitely will be extremely difficult for polymers both kinetically and mechanically. Thermodynamically,[20,21] the condition for two chemically unlike high polymers to be mutually compatible, i.e. $\Delta G_m < 0$, where ΔG_m is the free energy of mixing, can be observed only in exceptional cases. This is because of the great reduction in the entropy of mixing, ΔS_m, associated with the smaller number of molecules involved by virtue of their contiguous nature and the endothermic nature of the process of mixing. Thus, when two polymers of different chemical composition are brought together, they will not intermix at the molecular level and will not give a homogeneous single phase structure. The ultimate state of molecular mixing attainable by many liquid mixtures can only be approached as a limit by polyblends. Hence, compatibility in this case is a representation of how close a limiting state of mixing is approached. Crudely and qualitatively, compatibility is signified often by the transparency of the polyblend, since when phase separation occurs it always is accompanied by an opaque appearance if the refractive indices of the components are different. Quantitatively, compatibility has to be a relative property and is related directly to the degree of inhomogeneity of the polyblend;[22] the larger the inhomogeneity, the lower the

compatibility of the components of the polyblend and vice versa.

Although polymethyl methacrylate (PMMA) has a refractive index fairly close to that of polystyrene (PS), the two are not compatible at all compositions. In what follows, the inhomogeneity of a series of their blends are studied and analyzed by the method of light scattering which was discussed in the last chapter.

Inhomogeneity Parameters

The theory presented in Chapter II is a general one and is applicable to any isotropic inhomogeneous medium. However, the two parameters used to characterize the inhomogeneity of the medium, namely the variance in permittivity, $\langle \delta\epsilon^2 \rangle$, and the correlation function, $F(\rho)$, can be extended to the case of polyblends where one component is distributed in a matrix formed by the other.

First let us consider $\langle \delta\epsilon^2 \rangle$. To the first approximation, we can regard the two components as being separately homogeneous so that ϵ_1 and ϵ_2 are their electric permittivities respectively. If Φ_1 and Φ_2 represent the volume fractions occupied by each of them, the mean permittivity, $\langle \epsilon \rangle$, of the medium is given by:

$$\langle \epsilon \rangle = \Phi_1 \epsilon_1 + \Phi_2 \epsilon_2 \ . \qquad (3.1)$$

The local deviations in permittivity pertaining to each component from the mean are then:

$$\delta\epsilon_1 = \epsilon_1 - \langle\epsilon\rangle = (\epsilon_1 - \epsilon_2)\phi_2$$

and (3.2)

$$\delta\epsilon_2 = \epsilon_2 - \langle\epsilon\rangle = (\epsilon_2 - \epsilon_1)\phi_1 \ .$$

From equation (3.2), we obtain the variance in permittivity:

$$\langle\delta\epsilon^2\rangle = \phi_1(\delta\epsilon_1)^2 + \phi_2(\delta\epsilon_2)^2 = (\epsilon_1-\epsilon_2)^2\phi_1\phi_2 \ . \quad (3.3)$$

Thus, for a polyblend of two components having about the same density the amplitude of the inhomogeneity depends on the amount of the second component blended with the first. If $\phi_1 > \phi_2$, the greater the amount of the second component added, the larger the amplitude of the inhomogeneity will be.

With a polyblend, we can also define two additional inhomogeneity parameters based on the limiting properties of the correlation function:

$$\lim_{\rho\to 0} F(\rho) = 1$$

and

$$\lim_{\rho\to\infty} F(\rho) = 0$$

Following Porod,[23] we allow the second component which is distributed in a matrix of the first to have an arbitrary form and a volume fraction ϕ_2. Then, the probability, $z(\rho)$, that a point within the volume of the polyblend at a distance ρ from a given point occupied by the second component is itself also occupied by that component is given by:

$$z(\rho) = \phi_2 + (1 - \phi_2)F(\rho) \ . \quad (3.4)$$

Integrating equation (3.4) for a range of ρ from 0 to L,

$$\int_0^L z(\rho)d\rho = L\phi_2 + (1 - \phi_2) \int_0^L F(\rho)d\rho \ ,$$

or for L large enough,

$$\int_0^L z(\rho)d\rho \approx L\phi_2 + (1 - \phi_2) \int_0^\infty F(\rho)d\rho \ . \qquad (3.5)$$

According to Porod,

$$\int_0^\infty F(\rho)d\rho = 1_c/2 \ , \qquad (3.6)$$

where 1_c is an inhomogeneity parameter called the "distance of heterogeneity".

The geometrical significance of 1_c is as follows.[12] Let us draw an arbitrary line of length L in an arbitrary direction from a point occupied by the second component. This line will then be divided into segments which are alternately occupied by either one of the two components comprising the polyblend. The integral of $z(\rho)$ over ρ is a representation of the probable length of the line which will be occupied by the second component. It is larger than the mean length, $L\phi_2$, similarly occupied because the condition upon which the line is first drawn enhances the chance of finding a segment so occupied. The excess length is represented by $(1 - \phi_2)1_c/2$.

Furthermore, by integrating $4\pi\rho^2 z(\rho)$ over a range of ρ from 0 to R, we obtain the probable volume occupied by the second component as follows:

$$\int_0^R 4\pi\rho^2 z(\rho)d\rho = V\phi_2 + (1 - \phi_2)\int_0^R 4\pi\rho^2 F(\rho)d\rho ,$$

or for R large enough,

$$\int_0^R 4\pi\rho^2 z(\rho)d\rho \approx V\phi_2 + (1 - \phi_2)\int_0^\infty 4\pi\rho^2 F(\rho)d\rho , \qquad (3.7)$$

where V is the total volume of the polyblend.

Here again, by virtue of the conditional nature of the probability function, $z(\rho)$, the probable volume is larger than the mean volume, $V\phi_2$, occupied by the second component by $(1 - \phi_2)\int_0^\infty 4\pi\rho^2 F(\rho)d\rho$. We can define:

$$\int_0^\infty 4\pi\rho^2 F(\rho)d\rho = v_c , \qquad (3.8)$$

where v_c is a parameter which, according to Porod, characterizes the "volume of heterogeneity".

Thus, the inhomogeneity of a polyblend can be characterized in amplitude by the variance in permittivity, $\langle\delta\epsilon^2\rangle$, (or the standard deviation in refractive index, $\sqrt{\langle(\delta n)^2\rangle}$); in extent by the correlation distance, a, given by the correlation function, $F(\rho)$, and the distance of heterogeneity, l_c; and in space by the volume of heterogeneity, v_c.

In an experimental investigation of porous catalytic materials by X-ray scattering, Debye, Anderson and Brumberger[24] noticed that in some cases, the angular dependence of the scattered intensity separated into two parts at small and large angles within the low-angle range of their measurements and could not be characterized by a correlation

function which consisted of only one function. Accordingly, Debye and coworkers and others,[25-27], who also observed in some other systems a similar break in the angular dependence of the scattered intensity, proposed the correlation function $F(\rho)$ to be represented as follows:

$$F(\rho) = fF_1 + (1 - f)F_2 \ , \qquad (3.9)$$

where F_1 weighed statistically by a fractional contribution factor f and F_2 by a factor $(1 - f)$ were two single-functioned correlation functions (see later section under "Data Analysis and Results") which described the scattered intensities measured at large and small angles respectively. With this form for $F(\rho)$, the authors were able to analyze their experimental results and found the associated correlation distances, a_1 and a_2, measuring the short- and long-range inhomogeneities of their samples respectively. Debye and coworkers did not justify the physical meaning of the long-range correlation distance a_2, which they obtained by proposing the correlation function F_2 to be a Gaussian (i.e. $F_2 = \exp[-(\rho/a_2)^2]$), with respect to the structure of their materials. However, they showed that with an exponential form for the correlation function F_1 (i.e. $F_1 = \exp(-\rho/a_1)$), the short-range correlation distance a_1 and also the fractional contribution factor f if $f \neq 1$ were theoretically related to the specific surface of the voids randomly distributed in their samples. Their calculated values of the specific surface from a_1

and f were in good agreement with those determined by gas adsorption. Recently, by using Debye's functions for F_2 and F_1, Moritani and coworkers[26] characterized by light scattering the inhomogeneities of a series of copolymer blend specimens (see later section under "Discussion") which were composed of spherical domains of uniform size dispersed in a continuous matrix. With their experimentally determined a_1 and f and noting the relationship between specific surface and radius, the authors also found a 1:1 correspondence between the calculated values of the radius of the spherical domains of their samples and those observed from electron micrographs. These two instances of agreement certainly provide direct proofs on the soundness of the isotropic theory of scattering discussed in Chapter II. Furthermore, in cases like these when $F(\rho)$ is represented by equation (3.9), the fractional contribution factor f of the short-range correlation function F_1 constitutes another parameter which characterizes the inhomogeneity of the sample.

Experimental

Material

The materials used to prepare the samples consisted of methyl methacrylate monomer, narrow-molecular-weight-distribution polystyrene and α,α'-azobisisobutyronitrile (AIBN) initiator. The monomer, stabilized with hydroquinone, was

obtained from Eastman Kodak Company which also supplied the AIBN initiator. The polystyrene was of the anionically polymerized type having a molecular weight of 82,500 and was kindly supplied by Dow Chemical Company.

Monomer Purification

Before the monomer was employed in preparing the samples, it was purified carefully as follows:

The hydroquinone stabilizer of the monomer was first removed by shaking the monomer with 5% by weight of sodium hydroxide solution in a separation funnel. The brownish colored aqueous phase containing the stabilizer was then drained from the funnel. The procedure was repeated until the brownish color did not appear in the aqueous phase.

The organic phase was washed three times with one liter of distilled water each to remove any trace of sodium hydroxide that might have remained. The monomer was then transferred to a flask where it was dried over drierite for more than three hours. The drying process was completed when a fresh addition of blue drierite did not become pink in color. The dried monomer was filtered through another inch of drierite into a distillation flask. Dry purified nitrogen gas was bubbled through the monomer for one hour before distillation was started thereby minimizing polymerization during distillation. With the stream of nitrogen maintained, the monomer was distilled through a Vigreaux column under 10 cm pressure where it boiled at 48^{0}C. After

a final flush with purified nitrogen for 15 minutes, only the middle portion of the distillate was collected and stored in refrigerator.

Before use, the distillation apparatus and the storage vessels were thoroughly cleaned with liquid detergent and distilled water; baked overnight in an annealing oven at 580^{0}C; flushed with fresh aqua regia for half a day; rinsed successively with distilled, demineralized and triple-distilled water and finally dried at 110^{0}c.

The distilled monomer was further checked for impurities with gas chromatography using a carbowax column. The chromatogram (Fig. 3.1) showed only one sharp peak indicating the high purity of the collected monomer.

AIBN Purification

The AIBN initiator is thermally unstable and will decompose at moderate temperatures. To ensure decomposition did not occur, the initiator was dissolved in Spectro-Grade benzene and recrystallized. The crystals were dried under vacuum and stored in the refrigerator until needed.

Sample Preparation

Altogether seven samples ranging from a pure polymethyl methacrylate (PMMA) and six blends of 0.0001%, 0.001%, 0.005%, 0.01%, 0.03% and 0.05% polystyrene (by weight) in polymethyl methacrylate were prepared.

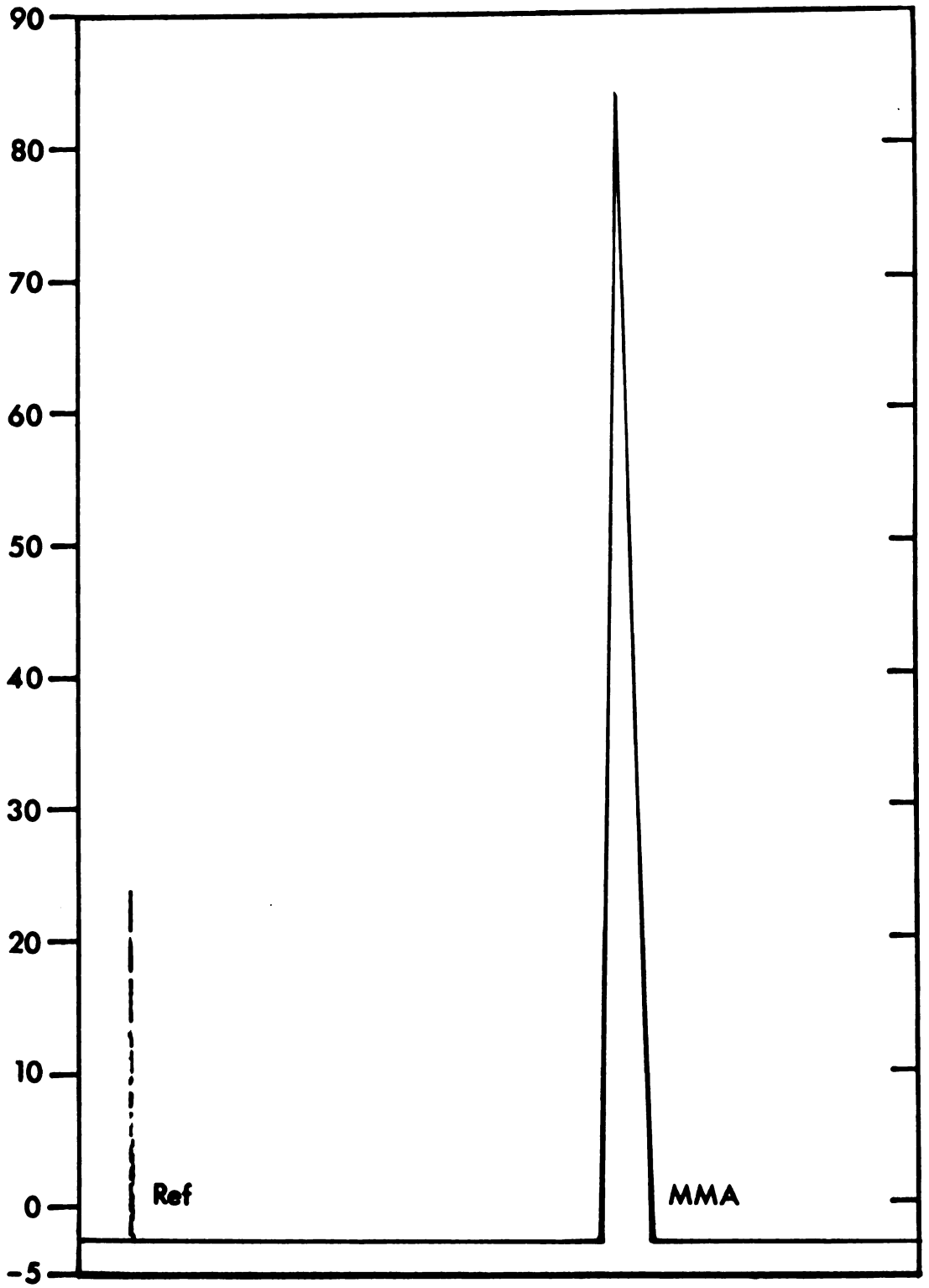

Figure 3.1. Gas chromatogram of MMA monomer.

PMMA:-- The pure polymethyl methacrylate sample was prepared by dissolving about 0.1% by weight of the AIBN initiator in the distilled methyl methacrylate monomer. The liquid was then introduced into a filtration apparatus (Fig. 3.2) where it was filtered first through a very fine sintered glass filter and then a 0.25μ Solvinert Millipore filter into the sample tube.

The filtration apparatus and the sample tube were thoroughly cleaned before use in the same way as the distillation apparatus used for the monomer purification. The filtration apparatus and the sample tube were designed to form a completely closed system to avoid any unnecessary contamination that might have resulted from the shortest exposure of the filtrate to air before it was covered. The sample tube, 2 cm in ID and 19 cm in length, was made of Pyrex and had a constriction for easy seal-off 7 cm below the joint to the filtration apparatus.

When enough liquid was collected in the sample tube, valve B in Figure 3.2 was closed. The liquid was degassed via valve C (Fig. 3.2) by a standard freeze-thaw procedure until it evolved no gas bubbles when thawed. After degassing, the sample tube was sealed off at the constriction while it was still frozen in a dewar of liquid nitrogen.

The liquid in the sealed tube was melted in cool methanol. Then, the tube was introduced into a paraffin oil temperature bath where the monomer was polymerized thermally to a solid polymer at 50°C followed by a final

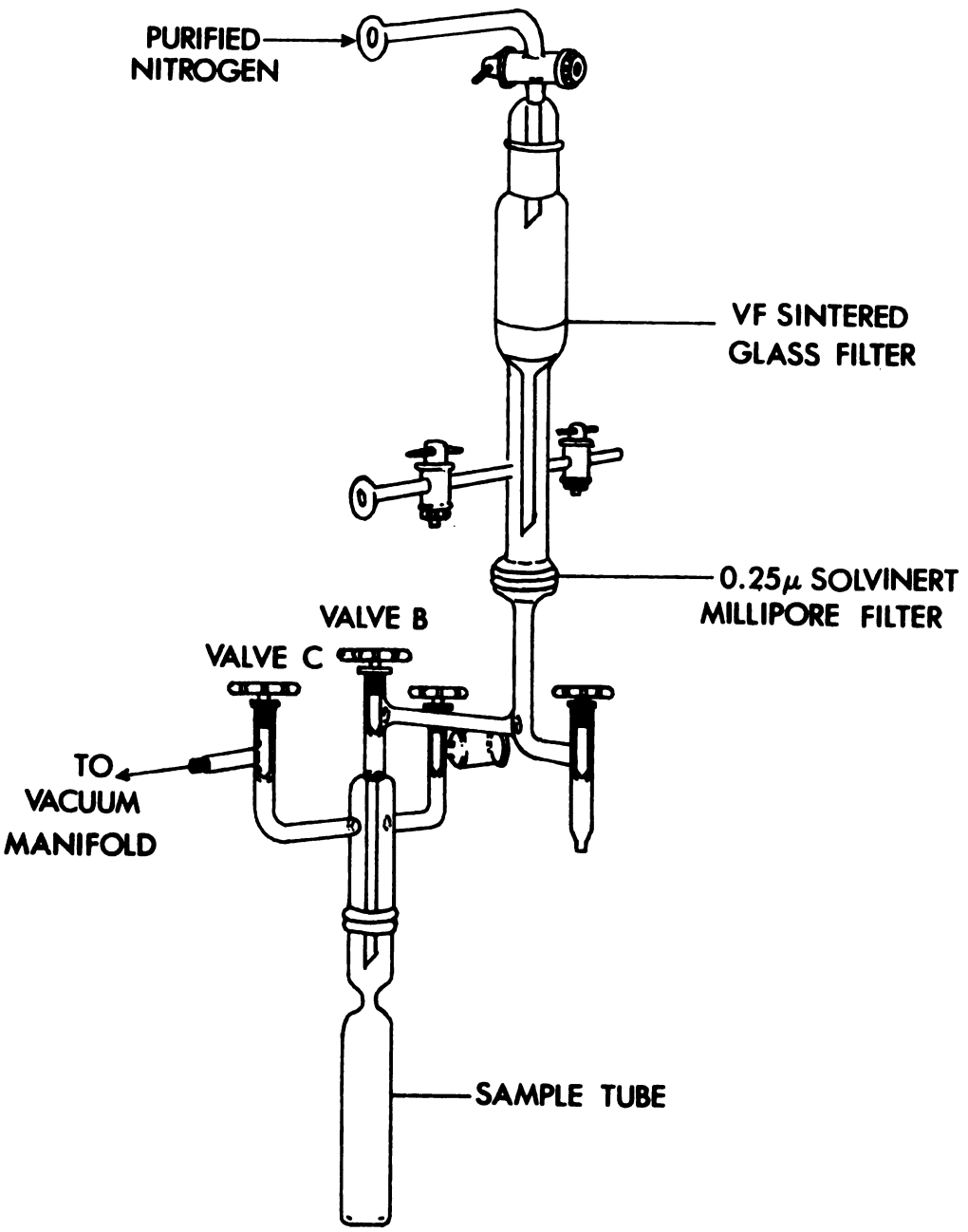

Figure 3.2. Filtration apparatus.

annealing at 101°C to complete the polymerization. Table 3.1 shows the thermal history which the sample has undergone.

Table 3.1. Thermal history of pure PMMA.

Sample	T_1 (°C)	t_1 (hr)	T_2 (°C)	t_2 (hr)	T_3 (°C)	t_3 (hr)	T_4 (°C)	t_4 (hr)
PMMA	40	4	51	14	71	5	101	5

PS/PMMA Blends:-- The blends were prepared in exactly the same way as PMMA except:

1) in addition to the AIBN initiator, an appropriate amount of polystyrene was also added to the distilled methyl methacrylate monomer;

2) the liquid mixture was filtered through an ultra fine sintered glass filter instead of a combination of a very fine glass filter and a Millipore filter.

The amount of polystyrene used for the 0.001% and 0.0001% blends were obtained by successive dilution of the 0.005% polymer-monomer solution with monomer. Since it is a well known fact that the degree of inhomogeneity of a sample depends on the heat treatment it has undergone, the blends were all subjected to the identical thermal history of polymerization shown in Table 3.2.

Table 3.2. Thermal history of PS/PMMA blends.

PS/PMMA Blend (%)	T_1 (^{0}C)	t_1 (hr)	T_2 (^{0}C)	t_2 (hr)	T_3 (^{0}C)	t_3 (hr)	T_4 (^{0}C)	t_4 (hr)	T_5 (^{0}C)	t_5 (hr)
0.0001	45	5	50	14	65	4	80	4	100	21
0.001	45	5	50	14	65	4	80	4	100	21
0.005	45	5	50	14	65	4	80	4	100	21
0.01	45	5	50	14	65	4	80	4	100	21
0.03	45	5	50	14	65	4	80	4	100	21
0.05	45	5	50	14	65	4	80	4	100	21

Table 3.3. Dimensions of pure PMMA and PS/PMMA blends.

Sample	Diameter (cm)	Length (cm)
PMMA	1.585	1.915
0.0001% PS/PMMA	1.595	1.910
0.001 % PS/PMMA	1.585	1.946
0.005 % PS/PMMA	1.593	1.923
0.01 % PS/PMMA	1.590	1.895
0.03 % PS/PMMA	1.582	1.930
0.05 % PS/PMMA	1.590	1.913

Sample Polishing

After polymerization and removal from the glass tubes, the samples were fairly rough and were not suitable for light scattering experiments. Thus, they were polished as follows:

Each sample was cut into two portions. One portion was machined in a lathe into a perfect cylinder, about 1.6 cm in diameter and 1.9 cm in length, with two flat ends, while the other portion was milled into a rectangular tile, about 2 cm in length, 1.5 cm in width and 0.5 cm in depth. To preserve the thermal history of the sample, liquid nitrogen was blown at the cutting tool to minimize heating while the sample was machined. The curved surface of the cylindrical portion was polished carefully in the lathe first with super fine emery paper and then with "Semichrone" plexiglass polish (a product of Competition Chemicals, Iowa) on a clean cloth. Liquid nitrogen cooling was also used in the polishing process to minimize heat. The flat surfaces of the two portions of the sample were polished in exactly the same way but on a flat table.

The polished samples were extremely smooth and were almost completely free from scratches or surface blemishes. The interiors were completely free of bubbles and visible defects. The cylindrical portion was used for light scattering. The rectangular tile was used for refractive index measurements. Table 3.3 is a representation of the dimensions of the polished cylindrical samples.

Isotropy of Sample

The scattering theory discussed in Chapter II is based on the assumption that the sample is isotropic. Therefore, to justify the use of the theory, the isotropy of our samples must be confirmed. This was done in a Brice-Phenix photometer. The green line from the mercury arc source was incident normally on the flat end of the sample and the scattered intensities at different angles were measured as the sample was rotated about its cylindrical axis. The constancy of the galvanometer readings at each angle (within experimental errors) shows the high degree of optical isotropy of our samples.

Low-Angle Photometer

The photometer used to measure the scattered radiation at low angles (Fig. 3.3) was a modified Brillouin spectrometer with no Fabry Perot interferometer. It was originally designed by S. Gaumer[28] and consisted of three basic subsystems as described below.

(1) Light source

The optical source was a 2 w. Spectra-Physics model 165 Argon ion laser which was energized by a model 265 fully regulated power supply and stabilized for single frequency operation with a model 589 air-spaced etalon. By tuning a thumbwheel, the laser could deliver eight vertically polarized emission lines of the following

L1 = Argon Ion Laser
ND = Neutral Density Filters
OR1 = Optical Rail 1
M1 = Mirror 1
OR2 = Optical Rail 2
M2 = Mirror 2
L2 = He-Ne Alignment Laser
OA = Optical Axis
P1 = Alignment Pinhole 1
S = Sample Holder
P2 = Alignment Pinhole 2
B = Bridgeport Table

LE1 = Small Light Pipe Lens 1
LP = Light Pipe
LE2 = Small Light Pipe Lens 2
I1 = Large Iris Diaphragm 1
F = Gelatin Green Filter
INT = Empty Fabry Perot Interferometer Housing
LE3 = Focussing Lens (f = 500 mm)
I2 = Large Iris Diaphragm 2
SH = Photographic Shutter

Figure 3.3. Schematic drawing of the low-angle photometer.

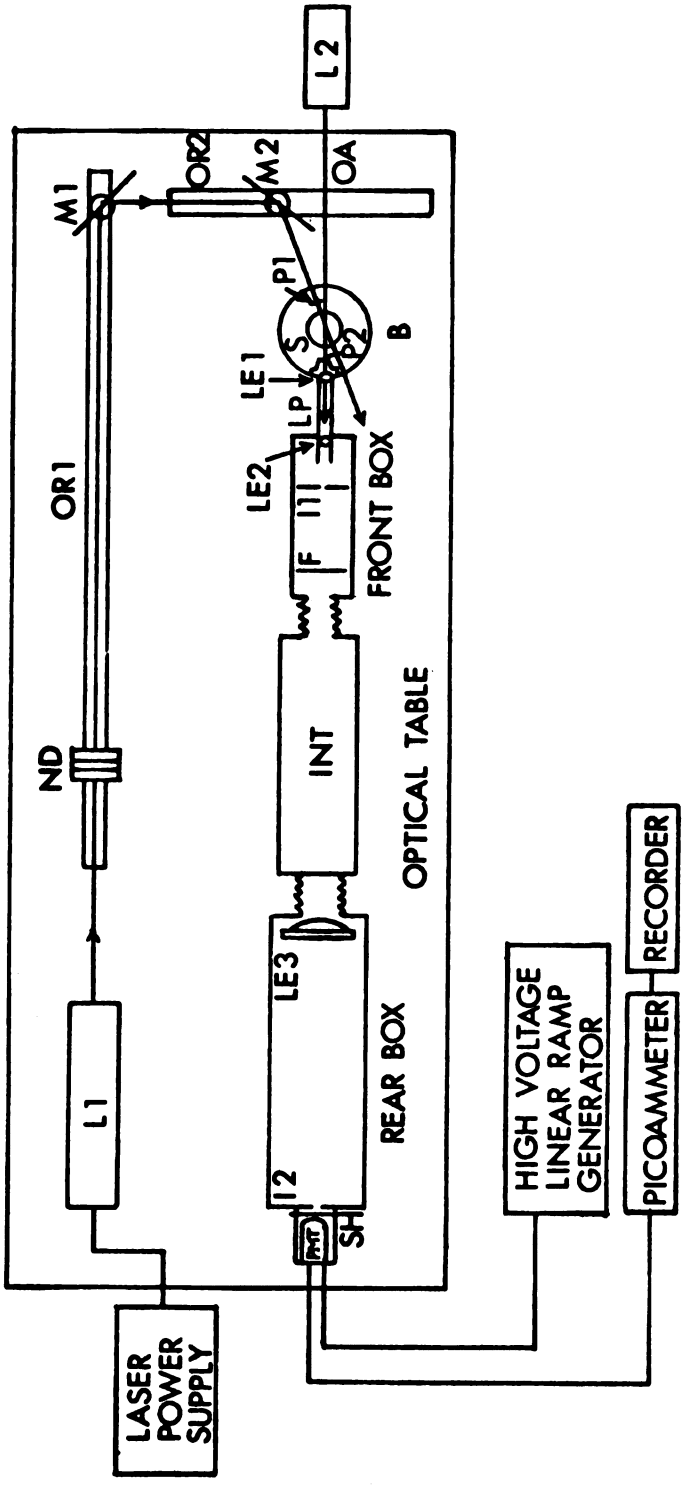
L2
OR2
M2
OA
M1
P1
S
P2
B
LE1
LP
LE2
F
FRONT BOX
OR1
ND
INT
OPTICAL TABLE
LE3
L1
I2
REAR BOX
SH
PMT
HIGH VOLTAGE
LINEAR RAMP
GENERATOR
RECORDER
PICOAMMETER
LASER
POWER
SUPPLY

Figure 3.3

wavelengths (nm.): 514.5, 501.7, 496.5, 488.0, 476.5, 472.7, 465.8, and 457.9. The green line (514.5 nm.) was chosen for the experiment because of its spectral purity in comparison to the others and its total available power of about 700 mw. With this line, the light mode output was stable at a power higher than 125 mw with a beam diameter of 1.5 mm.

The green light (about 200 mw.) from the laser was first incident normally on a series of neutral density filters to attenuate its intensity to within the scale of the detection system and then reflected by two mirrors carried on two separated and perpendicular optical rails into the sample compartment.

The neutral density filters were housed in parallel slots in a metal box which had been adjusted to center the filters to the beam. The filters were supplied by Special Optics Company and had the following suggested transmittances: 0.9%, 1.0%, 4.5%, 10.0%, 24.8%, and 47.2%. In combination, the filters provided an attenuation factor of $\prod_i F_i$ where F_i was the transmittance of the i^{th} filter.

The two mirrors which reflected the incident light into the sample compartment were each fitted to a Gimbal mount which was driven by two perpendicular micrometers. The first mirror, which was placed on the same optical rail as the neutral density filters, was further mounted on a small rotary table fitted to a precision

translation stage. Since the optical detection system was fixed, the mirrors constituted the main feature for changing the light course and hence, the scattering angle. The mirrors did not affect the polarization state of the incident light.

(2) Sample compartment

The sample compartment consisted of a pair of interlocked pinholes of 1 mm in diameter situated on either side of a 2" x 2" sample holder bracket which was placed at dead center on a Bridgeport rotary table. The angle of observation could be read to an accuracy of five seconds of a degree from the table scales. The compartment was not confined by any boundary.

The two pinholes which had been lined up initially with the optical axis of the photometer (see section under "Alignment") served as standard references for the incident radiation at a particular setting of the Bridgeport table. By moving the two mirrors described in the last paragraph along their respective optical rails, the incident beam could be centered on both pinholes with the aid of the micrometers on each Gimbal mount. Since the detection system of the photometer was fixed in position, the instrument did not have a provision for continuous angular scan. However, scattering angles from 3^0 to 135^0 could be obtained and ascertained, one at a time, in the manner just described.

The sample holder (Fig. 3.4) consisted of a rectangular teflon housing piece (1.6" x 1" x 0.76") sitting perpendicularly on a cylindrical aluminum jacket (1.75" x 2.28") which had a square base of the same dimension as the bracket on the Bridgeport table. The sample which had a teflon O ring of 0.95" x 0.2" surrounding it in front was housed and locked in position in a bore and a recess of matching dimensions in the housing piece. Oval shaped openings were milled out around the jacket and from the two sides of the housing piece so that light could go through the sample freely without reflection. To further minimize reflection, the whole sample holder was sprayed flat black.

(3) Detection system

The detection system (Fig. 3.3) was confined by a front box; an empty Fabry Perot interferometer housing; and a long rear box carrying a photomultiplier tube. The inside of the boxes were painted flat black to absorb extraneous light.

The scattered radiation from the sample was first collected by a light pipe (Fig. 3.5) which was extended from the front box to about 3.5" from the center of the Bridgeport table. The entrance of the light pipe was guarded by a rectangular slit (0.004" in width and 0.04" in length) followed by another (0.0045" in width and 0.096" in length) 0.05" away. The slits were constructed by screwing a circular insert, which had a hollow center and a sliced conical

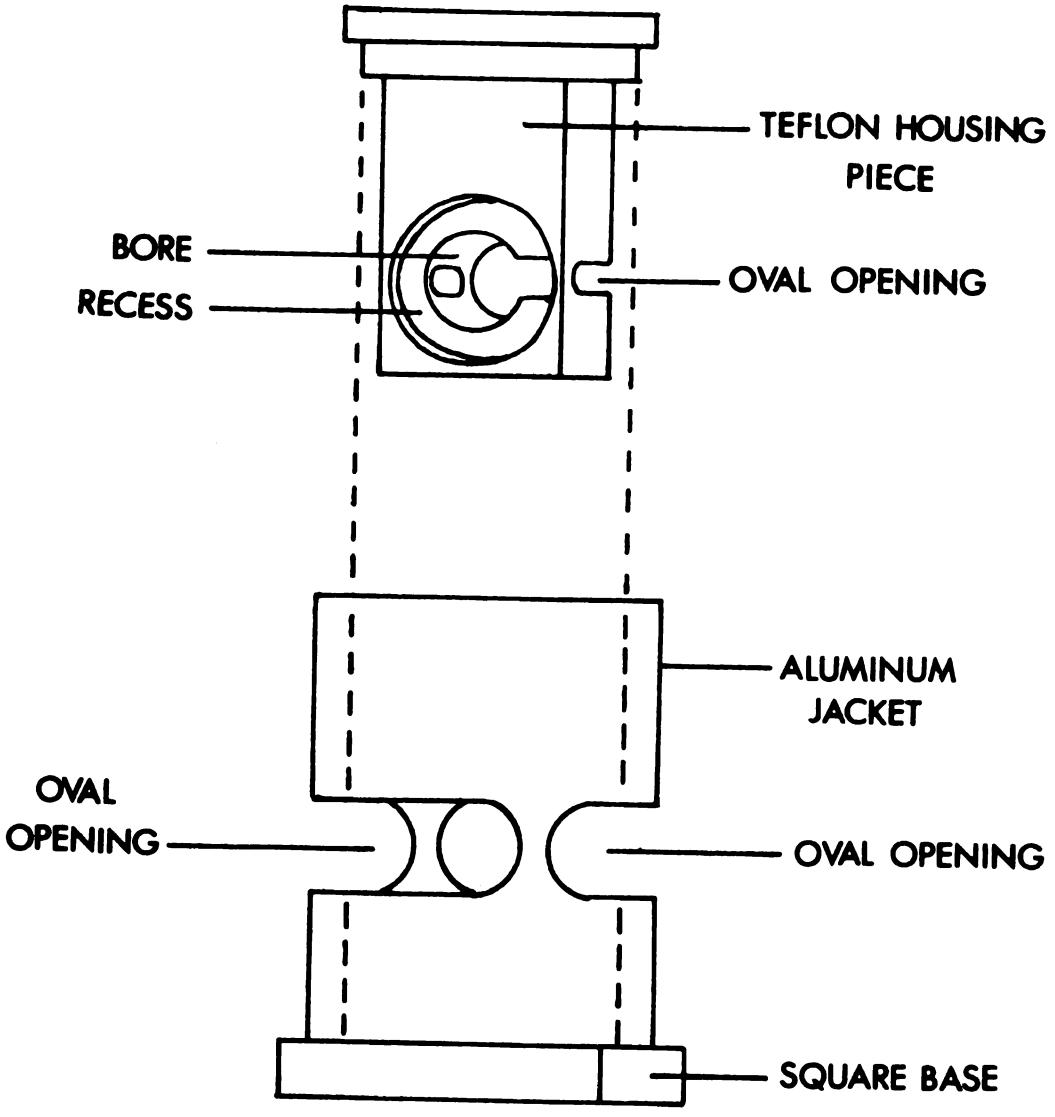

Figure 3.4. Sample holder.

SL = Slit, 0.004" in Width, 0.04" in Length

CN = Conical Nose Piece

CI = Circular Insert

CO = Circular Opening

AM = Adjustable Mount

LE1 = Small Biconvex Lens, f = 50 mm

AP = Aluminum Pipe

LE2 = Small Plano Convex Lens, f = 136 mm

Figure 3.5. Light pipe.

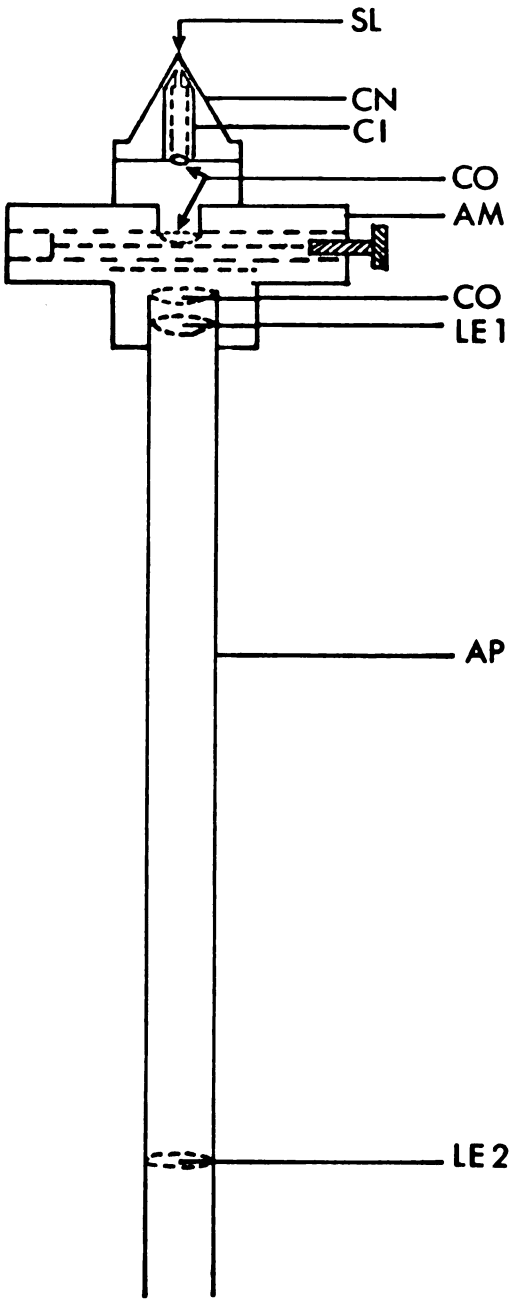

Figure 3.5

end, into a 60^0 conical nose-piece, which had a circular aperture of 0.04" in diameter at the apex. The dimensions of the slits depended on how far the insert was screwed into the nose-piece and were adjusted to the above values on an optical comparator. The conical piece was set into a mount which in turn was screwed and locked into a hollow aluminum pipe of 15" long. The mount was made adjustable only in the horizontal and vertical directions. To ensure the slits oriented vertically, two matching sets of perpendicular lines were scratched separately on the mount and on the front box. The first set was made with the aid of the optical comparator while the second set with a height gauge. Inside the aluminum pipe were two small lenses. The first one was placed behind the adjustable mount and was biconvex with a focal length of 50 mm. The second one which was 35.8 cm away from the first was plano convex and had a focal length of 136 mm. The conical nose-piece, the mount and the inside of the aluminum pipe were all sprayed flat black to minimize reflection. So constructed, the light pipe assembly provided a resolution angle not bigger then 0.6^0 on the horizontal plane.

After passing through the slits, the scattered radiation was focussed by the two lenses of the aluminum pipe to a large iris diaphragm inside the front box. The iris was adjusted to pass only the image of the slit and hence baffled out any extraneous light that might result from diffraction. The radiation was then probed by a Kodak

wratten gelatin green filter placed just behind the iris, whereby the component due to fluorescence (slightly red in color) was removed. Thereafter, the scattered light propagated through the empty Fabry Perot interferometer housing and was finally focussed by a large lens of f = 500 mm inside the rear box into the photomultiplier tube, which was protected in front by another baffled iris diaphragm followed by a photographic shutter.

The photomultiplier tube (EMI 9558 B), which detected the scattered light intensity, was housed in a refrigerated chamber and was powered by a Lansing model 80-010 high voltage linear ramp generator. The signal from the photomultiplier tube was then amplified by a Keithley model 417 picoammeter and was finally recorded by a Sargent model SRG recorder.

The characteristics of the photomultiplier tube and its refrigerated chamber, the high voltage linear ramp generator and the picoammeter have been discussed thoroughly by S. Gaumer[28] and can be found in his thesis.

Experimental Procedures

Alignment:- Prior to any measurement, the crucial alignment of the photometer was accomplished by sending a beam from a small Spectra-Physics model 132 He-Ne laser (Fig. 3.3) through two equal height, 1 mm pinholes which were placed respectively on the optical rail inside the front and the rear box confining the detection system of

the photometer. The laser was tapped laterally and raised or lowered carefully by adjusting the two laboratory jacks upon which it was anchored until the beam was adjusted to the center of the pinholes. With the laser untouched, the Bridgeport table was aligned with an alignment pin placed at its center. After removing the pin, the Bridgeport table was set at 180^0 so that the two pinholes on it could be centered with respect to the beam and then locked in position separately with a set screw. With the pinholes out of the way by turning the Bridgeport table to a new position, the light pipe assembly was placed into the front box. The two sets of perpendicular lines on the adjustable mount of the light pipe assembly and on the front box respectively were lined up to one another. The slit at the entrance of the light pipe was then centered with the beam by adjusting the mount until the intensity of its image as seen from the other end of the light pipe was maximum. The two baffled iris diaphragms, the Kodak wratten gelatin green filter and the large lens were then put into their proper places and adjusted optimally as described before.

Angular Distribution of Scattered Intensity:-- With the photometer aligned, the sample in its holder was placed into the square bracket at the center of the Bridgeport table. Normal incidence of the beam (λ_0 = 514.5 nm) on the flat end of the cylindrical sample was achieved by rotating the sample housing piece horizontally on its jacket until

the beam coincided with its back reflection. The intensity of the scattered radiation emerging from the other flat end of the sample was detected and recorded as a function of the scattering angle. The measurements were performed at room temperature.

As discussed in the Appendix, the scattering angle read off from the Bridgeport table scales before the sample was placed into the system was only an apparent one. To obtain the real scattering angle, this apparent value was corrected for the effect due to refraction inside the sample. The relative intensity of the scattered light was measured in chart units by taking the difference between the recorded signal line and the zero base line obtained with the photographic shutter in front of the photomultiplier tube in a closed position.

At the onset of the measurement, the voltage of the photomultiplier tube and the input scale of the picoammeter were adjusted so that the scattered light signal at the lowest scattering angle was displayed full scale on the recorder. At higher scattering angles, when the scattered intensity attenuated to a much smaller value, the signal was amplified either by substituting a higher transmittance neutral density filter in the incident beam or by changing the input scale of the picoammeter. Each time this was done, a corresponding expansion factor given by the ratio of the intensity recorded after and before amplification was noted. The subsequent intensities were then given by

$I_r^{\theta} \prod_i R_i$, where I_r^{θ} was the recorded intensity at a scattering angle θ and R_i was the reciprocal of the i^{th} expansion factor. The scattered intensities so measured were then corrected for the effects due to refraction, reflection and scattering volume (also attenuation for the 0.03% and 0.05% polystyrene samples) as discussed in the Appendix.

Turbidity:-- For convenience and better reproducibility, the turbidity of the sample was determined with the neutral density filters placed between the large f = 500 mm lens and the exit iris diaphragm in the rear box of the photometer (Fig. 3.3). Two intensity measurements were made at 0^0 setting of the Bridgeport table for the incident beam: (1) with no sample in its path, and (2) after it transversed through a sample of length ℓ. Since exactly the same combination of neutral density filters were used for both measurements, the transmittance factor of each of the filters was not important to the turbidity determination and therefore calibration was not necessary. However, the latter intensity measurement had to be corrected for reflection as shown in the Appendix. The results were (1) $I(0)$ and (2) $I(\ell)$ respectively. The turbidity of the sample was then calculated from equation (2.57) with ℓ shown in Table 3.3.

Refractive Index:-- Refractive index measurements were performed on a Bausch & Lomb - 3L refractometer. The refractometer was maintained at the same temperature as that at which the angular distribution of scattered intensity was measured by circulating water through the refractometer prisms from a Haake model FK constant temperature circulator. The sample milled to the form of a rectangular tile as described previously was placed in contact with the illuminated prism with a drop of 1-bromonaphthalene. Time was allowed for thermal equilibrium between the prism and the sample before the refractive index and the position of the compensator were finally read off from the refractometer. The index so determined was for the sodium D line (n_D), and could be corrected for $\lambda_0 = 514.5$ nm as follows:

With the aid of the standard dispersion table supplied with the refractometer and the compensator reading, the value of $(n_F - n_C)$, where n_F and n_C were the indices for the blue (486 nm) and red (656 nm) hydrogen lines respectively, was first determined. Two constants B and A given by:

$$B = 0.52364 \times 10^6 \ (n_F - n_C)$$

and

$$A = n_D - 2.8796 \times 10^{-6} \ B,$$

were computed. The index of refraction at $\lambda_x = 514.5$ nm was then calculated from the following equation:

$$n_x = A + \frac{B}{\lambda_x^2} \quad .$$

The above procedure was repeated with the other surface of the sample in contact with the illuminated prism. The mean refractive index of the sample was then evaluated by taking the average of the two corrected indices. Table 3.4 summarizes the results.

Data Analysis and Results

From equation (2.50b), it is seen that there are two methods by which the correlation function can be determined from the angular distribution of the scattered intensity. The first one which involves deconvolution of the Fourier transform of the measured intensity was discussed in Chapter II. The second one is the method of trial and error: trial expressions are assigned to the correlation function until its corresponding power spectrum (equation (2.50b)) matches with the experimental intensity distribution function. This method is comparably simpler and therefore was adopted.

The trial expressions for the correlation function must be positive-definite as required by the Wiener-Khintchine theorem (equation (2.11)). They must also satisfy:

$$\lim_{\rho \to \infty} F(\rho) = 1$$

$$\lim_{\rho \to \infty} F(\rho) = 0 \quad .$$

Table 3.4. Mean refractive indices of pure PMMA and PS/PMMA blends at λ_0 = 514.5 nm.

Sample	$\langle n \rangle_{514.5}$
PMMA	1.4942
0.0001% PS/PMMA	1.4943
0.001 % PS/PMMA	1.4943
0.005 % PS/PMMA	1.4944
0.01 % PS/PMMA	1.4946
0.03 % PS/PMMA	1.4947
0.05 % PS/PMMA	1.4948

The following is a representation of those which have been proposed for isotropic samples and selected from the literature by Ross[6,25]:

$$F_1 = \exp(-\rho/a)$$

$$F2 = \exp[-(\rho/a)^2]$$

$$F3 = 1/[1 + (\rho/a)^2]^2$$

$$F4 = (1 + \rho/a)\exp(-\rho/a)$$

$$F5 = \exp[-(\rho/a)^2/2]$$

$$F6 = (\rho/a)K_1(\rho/a) \quad ,$$

where $K_1(\rho/a)$ in F6 is the modified spherical Bessel function of order 1 and a is the correlation distance discussed previously. Since F1, F4, and F6 can be generated with $\nu = 1/2$, 3/2, and 1 respectively from:

$$F7 = (\rho/a)^{\nu}K_{\nu}(\rho/a)/[2^{\nu-1}\Gamma(\nu)] \quad ,$$

where $\Gamma(\nu)$ is the well known Gamma function and $K_{\nu}(\rho/a)$ is the modified spherical Bessel function of order ν, F7 has also been suggested[29] as a general expression for the correlation function. Figure 3.6 shows the behavior of F1 to F6 as a function of (ρ/a).

Among the first six types of correlation functions, F1 and F2 are by far the most common.[11,24,30] For experiments whose angular distribution of scattered intensity requires two expressions for the correlation function (see equation (3.9)), F2, which was originally introduced by Debye, Anderson and Brumberger[24] for porous materials, has

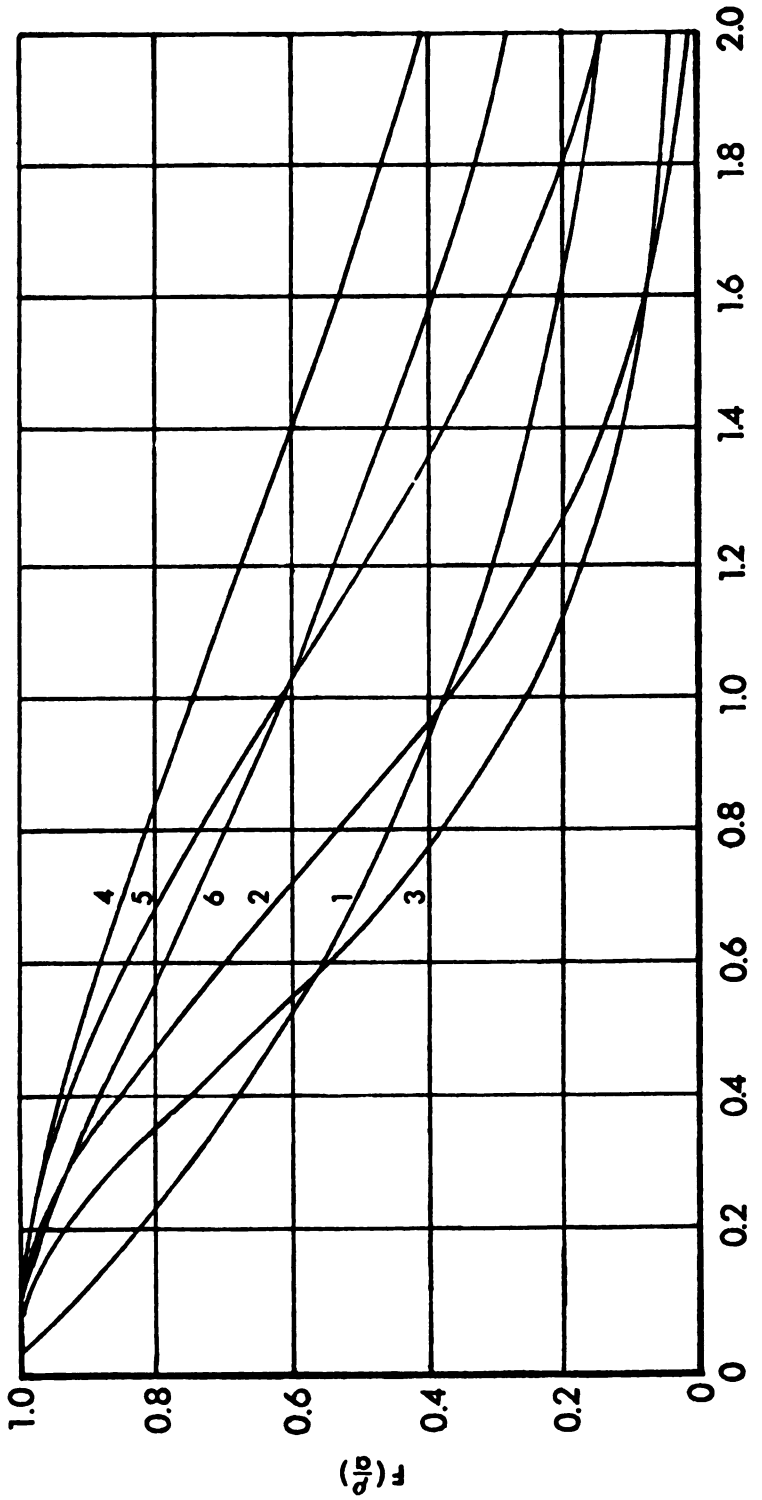

Figure 3.6. Behavior of six types of correlation functions (F1 to F6) proposed for isotropic samples.

always been suggested and found in agreement with the small-angle portion of the distribution.[25-27,31-33] There is some controversy over the type of correlation function for the large-angle portion, however. Although F1, which was first proposed by Debye and Bueche,[11] is still the most popular, great controversy exists about its physical validity because: (1) it is related to a completely disordered structure or a Markov process (see equation (2.13)) and (2) its derivative is discontinuous at the origin. For this reason, in the present study, all seven cited types of correlation functions were employed and whenever necessary F2 was added to account for the small-angle part of the distribution of the scattered intensity.

Table 3.5 lists the expressions for the corresponding power spectrum, I(s), and turbidity, τ, of each of the seven types of correlation functions. These expressions were calculated in terms of a dimensionless quantity

$$q = 2\langle k\rangle a \qquad (3.10)$$

instead of the correlation distance, a, from equations (2.50b) and (2.56) respectively. In the expressions, the parameter A is represented by:

$$A = \frac{I_0 V}{L^2} \langle k\rangle \frac{\langle \delta\epsilon^2\rangle}{\langle \epsilon\rangle^2} \quad ,$$

and s, as defined in equation (2.49a), is given by:

$$s = 2 \sin(\frac{\theta}{2}) \quad ,$$

Table 3.5. Power spectrum and turbidity expressions.

$F(\rho)$	$I(a)$	τ
$F1 = \exp(-\rho/a)$	$A\,\frac{1}{\pi}\,\frac{q^3}{(4+q^2a^2)^2}$	$\langle k\rangle\frac{\langle\delta\epsilon^2\rangle}{\langle\epsilon\rangle^2}\left[\frac{1}{4}q\left[\frac{(q^2+2)^2}{q^2(1+q^2)}-2\,\frac{q^2+2}{q^4}\ln(1+q^2)\right]\right]$
$F2 = \exp[-(\rho/a)^2]$	$A\,\frac{1}{128\sqrt{\pi}}\,q^3\exp(-\frac{q^2a^2}{16})$	$\langle k\rangle\frac{\langle\delta\epsilon^2\rangle}{\langle\epsilon\rangle^2}\left[\frac{\sqrt{\pi}}{8}q\left[(1+\frac{64}{q^4})[1-\exp(-q^2/4)]-\frac{8}{q^2}[1+\exp(-q^2/4)]\right]\right]$
$F3 = 1/(1+(\rho/a)^2)^2$	$A\,\frac{1}{128}\,q^3\exp(-\frac{qa}{2})$	$\langle k\rangle\frac{\langle\delta\epsilon^2\rangle}{\langle\epsilon\rangle^2}\left[\frac{\pi}{16}q\left[1-\frac{12}{q^2}+\frac{240}{q^4}-(q+5+\frac{28}{q}+\frac{108}{q^2}+\frac{240}{q^3}+\frac{240}{q^4})\exp(-q)\right]\right]$
$F4 = (1+\rho/a)\exp(-\rho/a)$	$A\,\frac{16}{\pi}\,\frac{q^3}{(4+q^2a^2)^3}$	$\langle k\rangle\frac{\langle\delta\epsilon^2\rangle}{\langle\epsilon\rangle^2}\left[\frac{1}{2}q\left[\frac{(q^4-2q^2-2)(2+q^2)}{q^2(1+q^2)^2}+\frac{4}{q^4}\ln(1+q^2)\right]\right]$
$F5 = \exp[-(\rho/a)^2/2]$	$A\,\frac{1}{32\sqrt{2\pi}}\,q^3\exp(-\frac{q^2a^2}{8})$	$\langle k\rangle\frac{\langle\delta\epsilon^2\rangle}{\langle\epsilon\rangle^2}\left[\frac{\sqrt{\pi}}{4\sqrt{2}}q\left[(1+\frac{16}{q^4})[1-\exp(-q^2/2)]-\frac{4}{q^2}[1+\exp(-q^2/2)]\right]\right]$
$F6 = (\rho/a)K_1(\rho/a)$	$A\,\frac{3}{2}\,\frac{q^3}{(4+q^2a^2)^{5/2}}$	$\langle k\rangle\frac{\langle\delta\epsilon^2\rangle}{\langle\epsilon\rangle^2}\left[\frac{3\pi}{8}q\left[\frac{\sqrt{[1+q^2]^3}-1}{3\sqrt{[1+q^2]^3}}\,\frac{q^4+2q^2+2}{q^4}-2\,\frac{\sqrt{[1+q^2]^3}-1}{\sqrt{[1+q^2]}}\,\frac{q^2+2}{q^4}-2\,\frac{1-\sqrt{[1+q^2]}}{q^4}\right]\right]$
$F7 = \frac{1}{2^{\nu-1}\Gamma(\nu)}(\rho/a)^\nu K_\nu(\rho/a)$	$A\,\frac{2^{3\nu}}{2\sqrt{\pi}}\,\frac{\Gamma(\nu+3/2)}{\Gamma(\nu)}\,\frac{q^3}{(4+q^2a^2)^{\nu+3/2}}$	$\langle k\rangle\frac{\langle\delta\epsilon^2\rangle}{\langle\epsilon\rangle^2}\left[\frac{\sqrt{\pi}}{4}\frac{\Gamma(\nu+3/2)}{\Gamma(\nu)}q\left[\frac{(1+q^2)^{\nu+1/2}-1}{(\nu+1/2)(1+q^2)^{\nu+1/2}}\,\frac{q^4+2q^2+2}{q^4}-\right.\right.$ $\left.\left.2\,\frac{(1+q^2)^{\nu-1/2}-1}{(\nu-1/2)(1+q^2)^{\nu-1/2}}\,\frac{q^2+2}{q^4}+2\,\frac{(1+q^2)^{\nu-3/2}-1}{(\nu-3/2)(1+q^2)^{\nu-3/2}}\,\frac{1}{q^4}\right]\right]$

$A = \frac{I_0 V}{L^2}\langle k\rangle\frac{\langle\delta\epsilon^2\rangle}{\langle\epsilon\rangle^2}$ $\qquad q = 2\langle k\rangle a$ $\qquad s = 2a\sin(\theta/2)$

where θ is the scattering angle. From the power spectrum expressions, it is obvious that if the experimentally determined intensity, I(s), is plotted according to the scheme shown in the third column of Table 3.6 for each type of correlation function, a straight line will result for the correct type.

The analysis was performed on a CDC 6500 computer with a Kinfit program written by Nicely and Dye.[34] The program was based on the Taylor series expansion and the least square principle. Before fitting with the computer and in order to determine whether the angular distribution of the scattered intensity could be characterized by a single correlation function, the scattering data of each sample were plotted with I(s) vs s according to the scheme shown in the third column of Table 3.6 for each type of correlation function. It was found that except for the pure PMMA sample, the data of all PS/PMMA blends needed to be characterized by a sum of two correlation functions (see discussion preceding equation (3.9)).

The large-angle intensity data (with PMMA, all intensity data) were supplied to the Kinfit program and were first fitted nonlinearly with each of the power spectrum expressions shown in Table 3.5. By comparing the sum of the square of the residual (residual = $I(s)_{calc.} - I(s)_{exp.}$) of the outputs, the correct type of correlation function was immediately established. Knowing the correlation function, the data were fed once more into the computer with the

Table 3.6. Linear-fit equations and plotting schemes.

F(ρ)	Linear-fit Equation	Plotting Scheme	q	A
$F1 = \exp(-\rho/a)$	$I^{-1/2}(s) = U(1) + U(2)s^2$	$I^{-1/2}(s)$ vs s^2	$2\left[\frac{U(2)}{U(1)}\right]^{1/2}$	$\frac{16\pi}{[U(1)]^2 q^3}$
$F2 = \exp[-(\rho/a)^2]$	$\ln I(s) = U(1) - U(2)s^2$	$\ln I(s)$ vs s^2	$4[U(2)]^{1/2}$	$\frac{128\sqrt{\pi}}{q^3}\exp[U(1)]$
$F3 = 1/[1+(\rho/a)^2]^2$	$\ln I(s) = U(1) - U(2)s$	$\ln I(s)$ vs s	$2U(2)$	$\frac{128}{q^3}\exp[U(1)]$
$F4 = (1+\rho/a)\exp(-\rho/a)$	$I^{-1/3}(s) = U(1) + U(2)s^2$	$I^{-1/3}(s)$ vs s^2	$2\left[\frac{U(2)}{U(1)}\right]^{1/2}$	$\frac{4\pi}{[U(1)]^3 q^3}$
$F5 = \exp[-(\rho/a)^2/2]$	$\ln I(s) = U(1) - U(2)s^2$	$\ln I(s)$ vs s^2	$2[2U(2)]^{1/2}$	$\frac{32\sqrt{2}\sqrt{\pi}}{q^3}\exp[U(1)]$
$F6 = (\rho/a)K_1(\rho/a)$	$I^{-2/5}(s) = U(1) + U(2)s^2$	$I^{-2/5}(s)$ vs s^2	$2\left[\frac{U(2)}{U(1)}\right]^{1/2}$	$\frac{64}{3[U(1)]^{5/2} q^3}$
$F7 = \frac{1}{2^{\nu-1}\Gamma(\nu)}(\rho/a)^\nu K_\nu(\rho/a)$	$I^{-1/(\nu+3/2)}(s) = U(1) + U(2)s^2$	$I^{-1/(\nu+3/2)}(s)$ vs s^2	$2\left[\frac{U(2)}{U(1)}\right]^{1/2}$	$\frac{4^{\nu+3/2}[2\sqrt{\pi}\Gamma(\nu)]}{2^{2\nu}\Gamma(\nu+\frac{3}{2})[U(1)]^{\nu+3/2} q^3}$

same program. This time, the fit was performed linearly according to the equations outlined in the second column of Table 3.6. This is shown in Figures 3.7-3.13 for each of the seven samples under study. From the plots, and with reference to the fourth and fifth columns of Table 3.6, the parameters, q_1 and A_1 (the subscript 1 is used in accord with a_1 discussed in equation (3.9) and signifies the association with the large angles) could be calculated. Moreover, from equation (3.10), the short-range correlation distance, a_1 (see equation (3.9)), was also determined.

To treat the small-angle data, the difference between the observed intensity and that calculated from the power spectrum expression just established for the large angles was first computed. The resultant data were then fitted linearly with the equation shown for F2 in the second column of Table 3.6. Figures 3.14-3.17 show the plots so obtained for the blends ranging from 0.0001% to 0.01% in polystyrene. With the aid of the expressions for F2 in the fourth and fifth columns of Table 3.6 and equation (3.10), the parameters q_2 and A_2 (the subscript 2 is used in accord with a_2 discussed in equation (3.9) and signifies the association with the small angles) and the long-range correlation distance, a_2 (see equation (3.9)), were computed.

Substituting equation (3.9) into equation (2.50b), it can be seen that the two parameters, A_1 and A_2, which have just been determined for the PS/PMMA blends are actually given by:

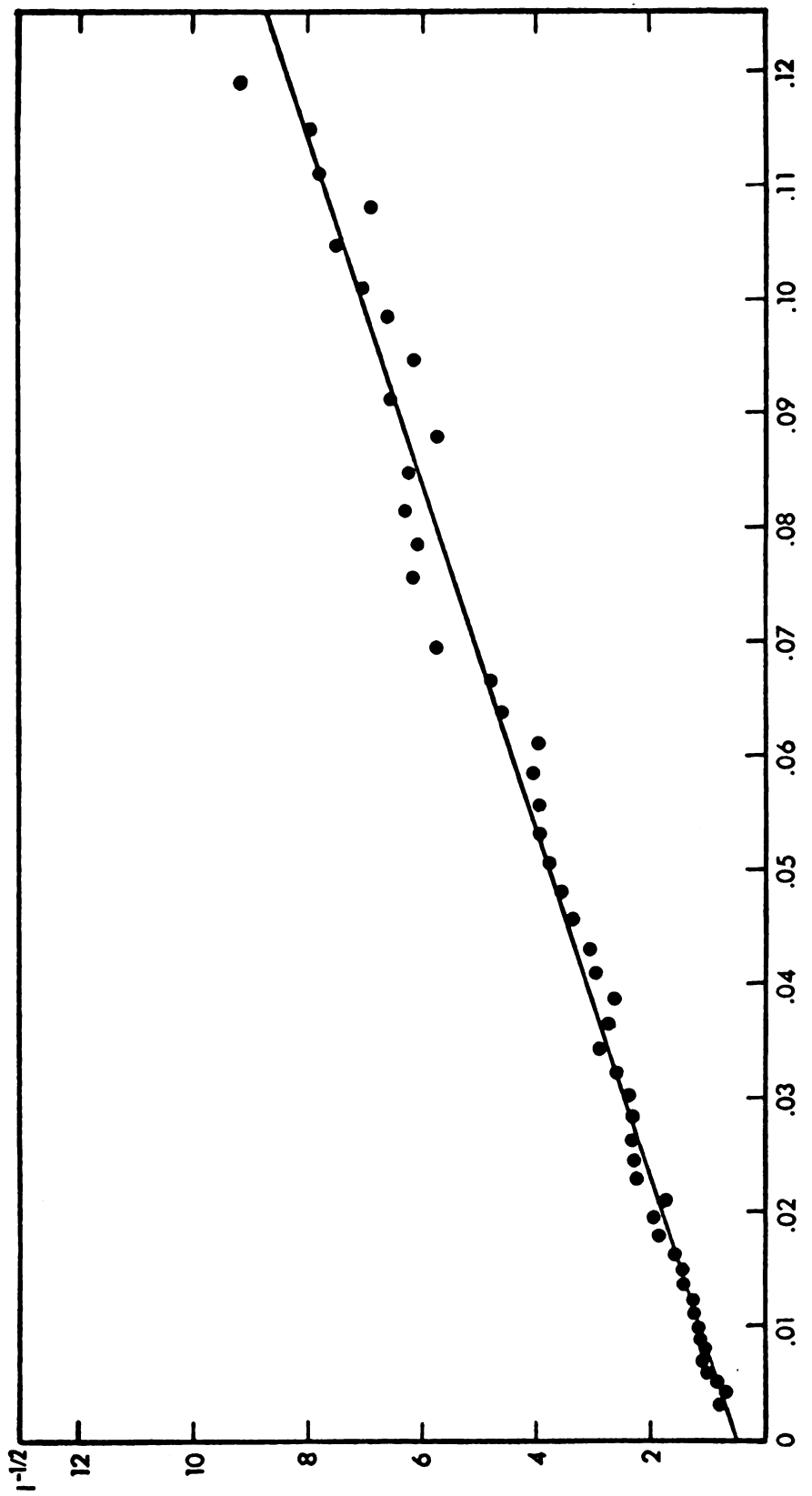

Figure 3.7. Angular dependence of scattered intensity: plot of $I^{-1/2}$ vs s^2 for pure PMMA.

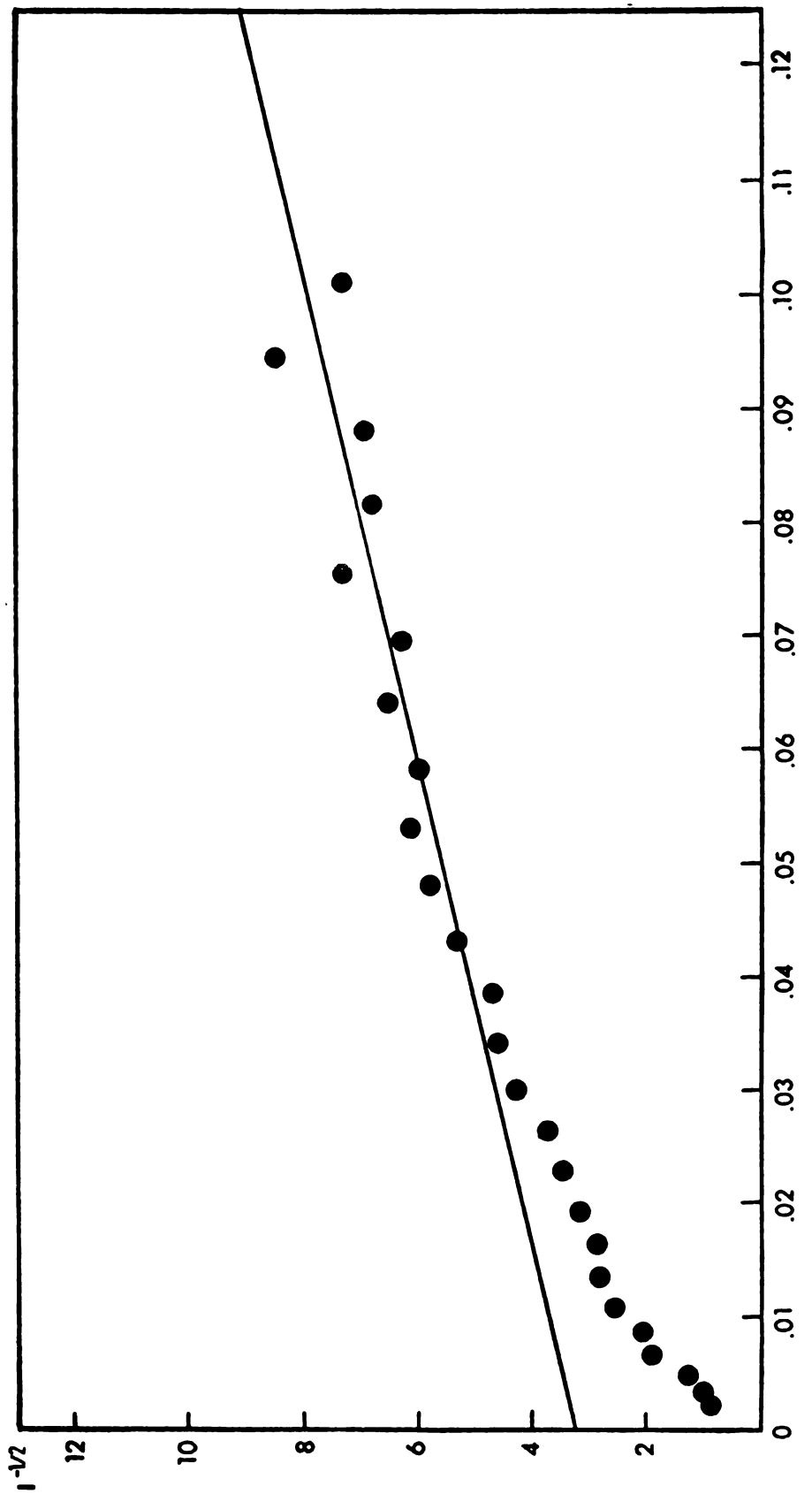

Figure 3.8. Angular dependence of scattered intensity at large angles: plot of $I^{-1/2}$ vs s^2 for 0.0001% PS/PMMA blend.

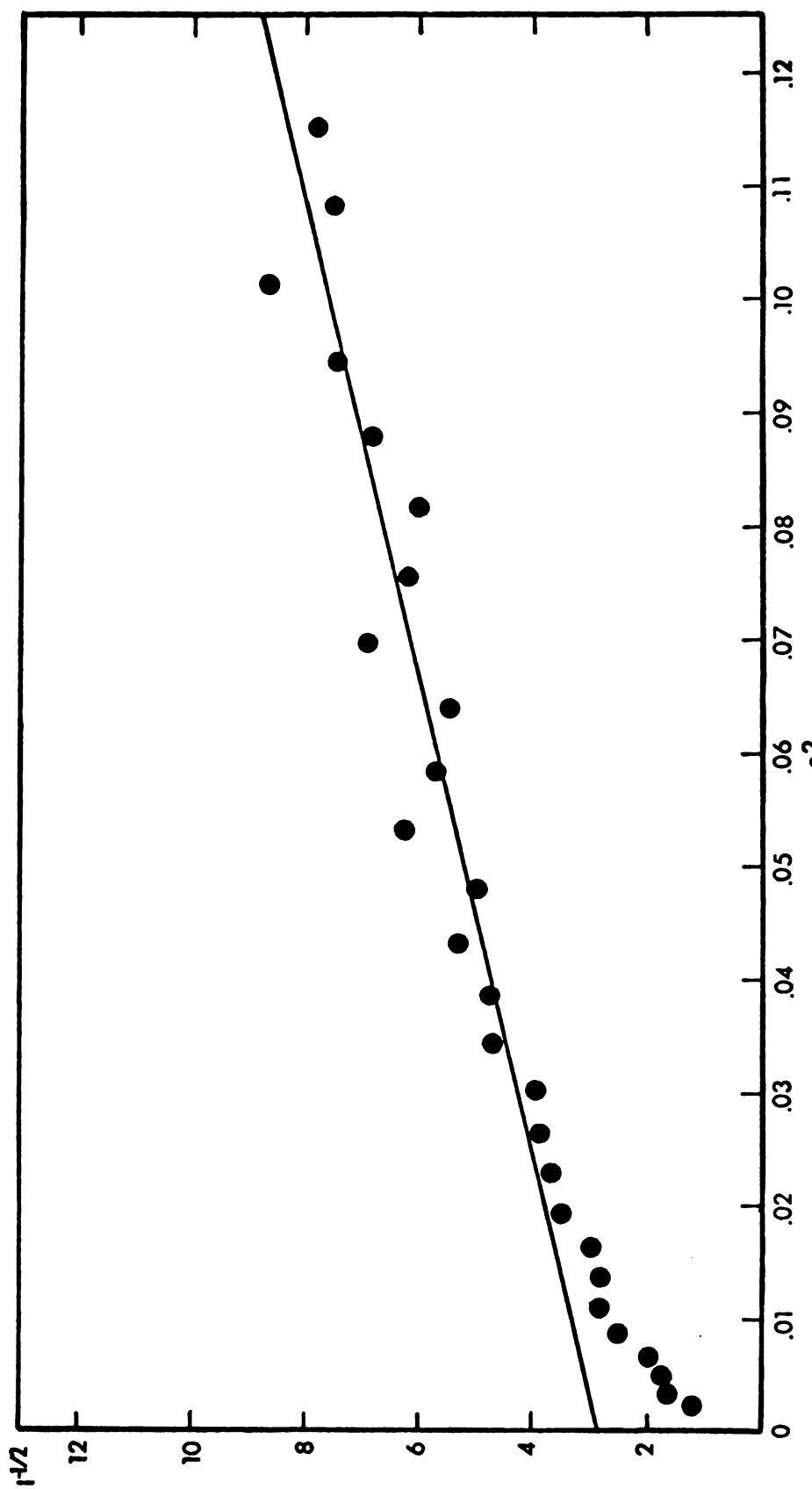

Figure 3.9. Angular dependence of scattered intensity at large angles: plot of $I^{-1/2}$ vs s^2 for 0.001% PS/PMMA blend.

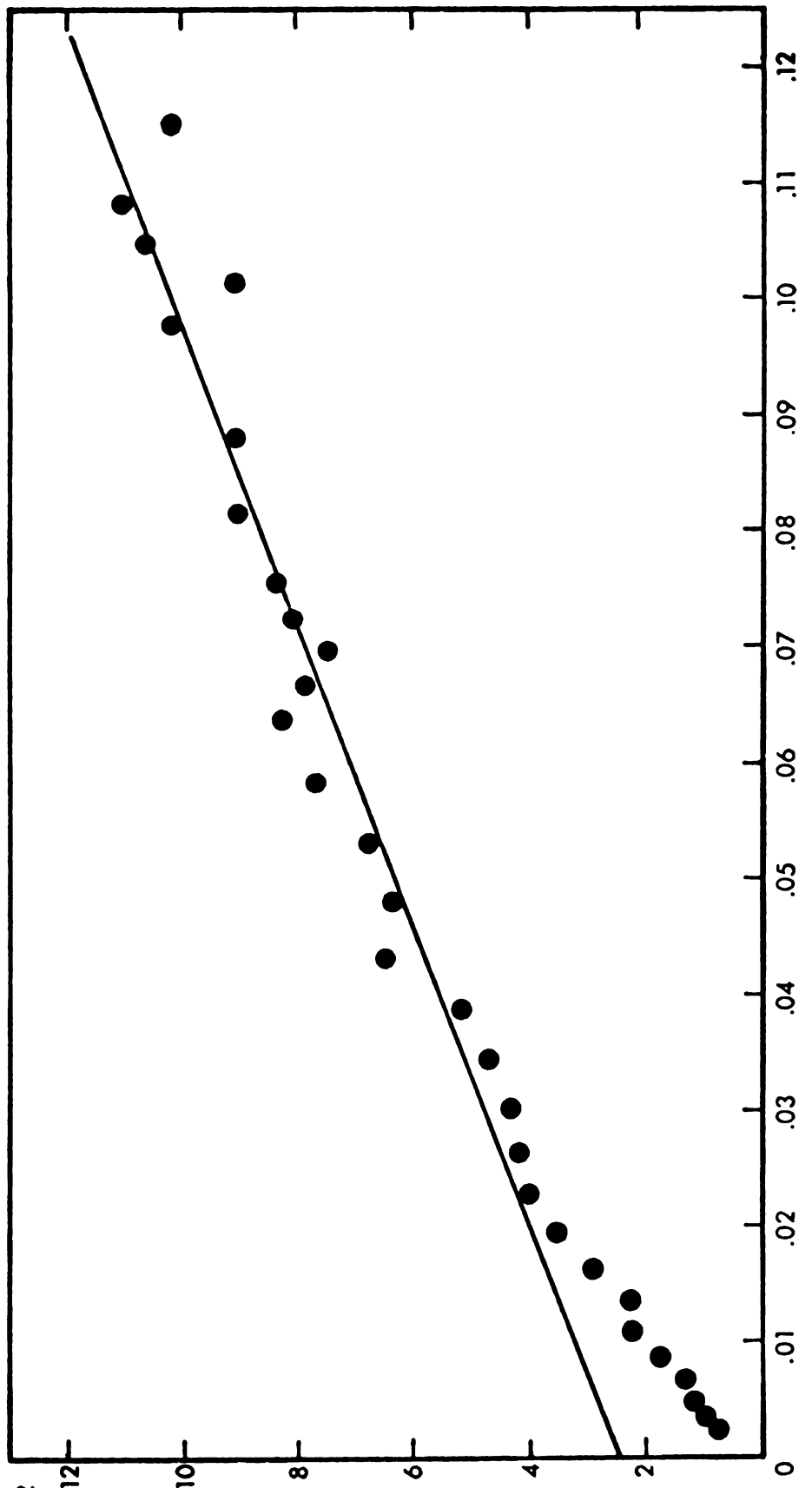

Figure 3.10. Angular dependence of scattered intensity at large angles: plot of $I^{-1/2}$ vs s^2 for 0.005% PS/PMMA blend.

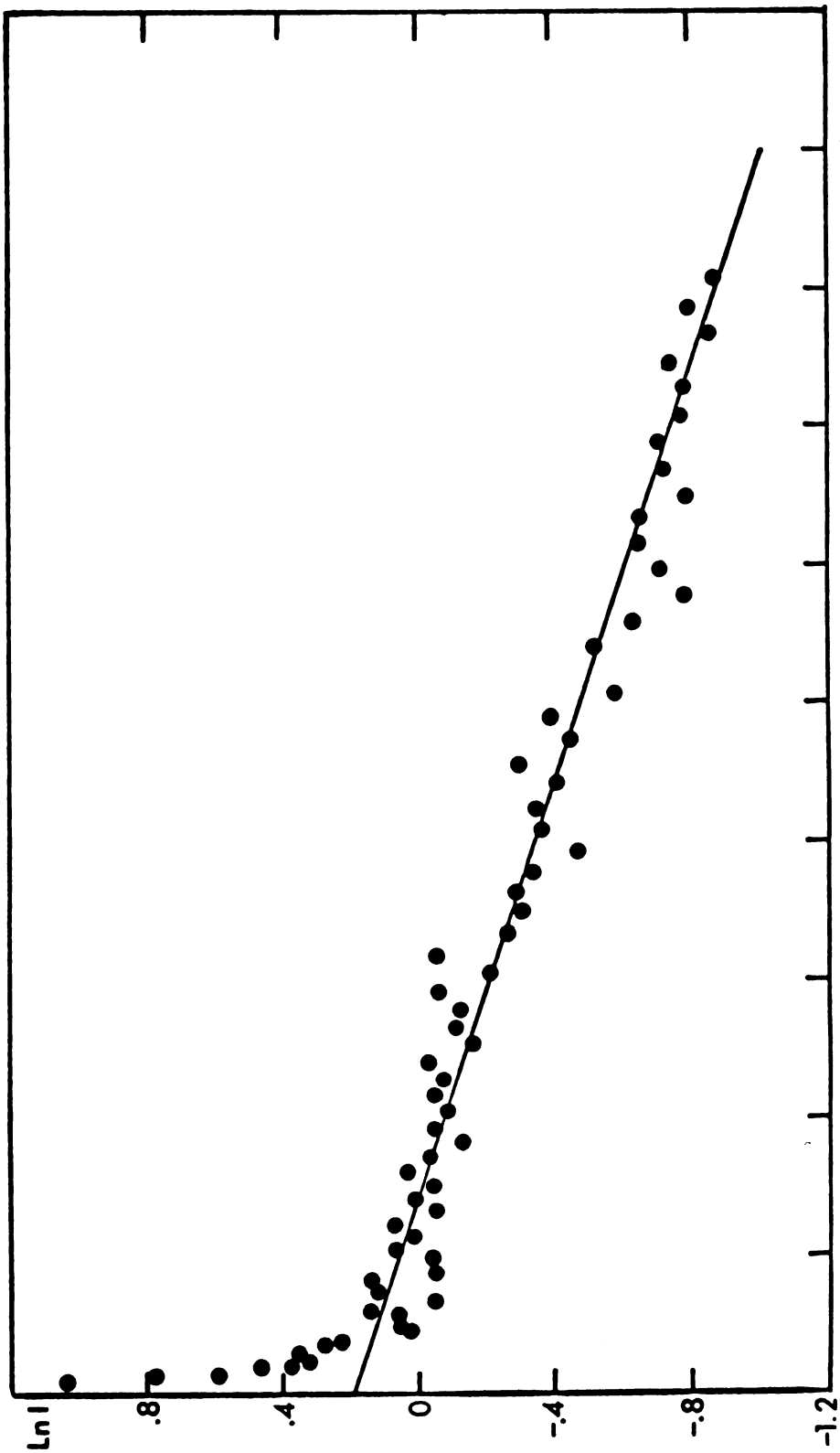

Figure 3.11. Angular dependence of scattered intensity at large angles: Plot of ln I vs s^2 for 0.01% PS/PMMA blend.

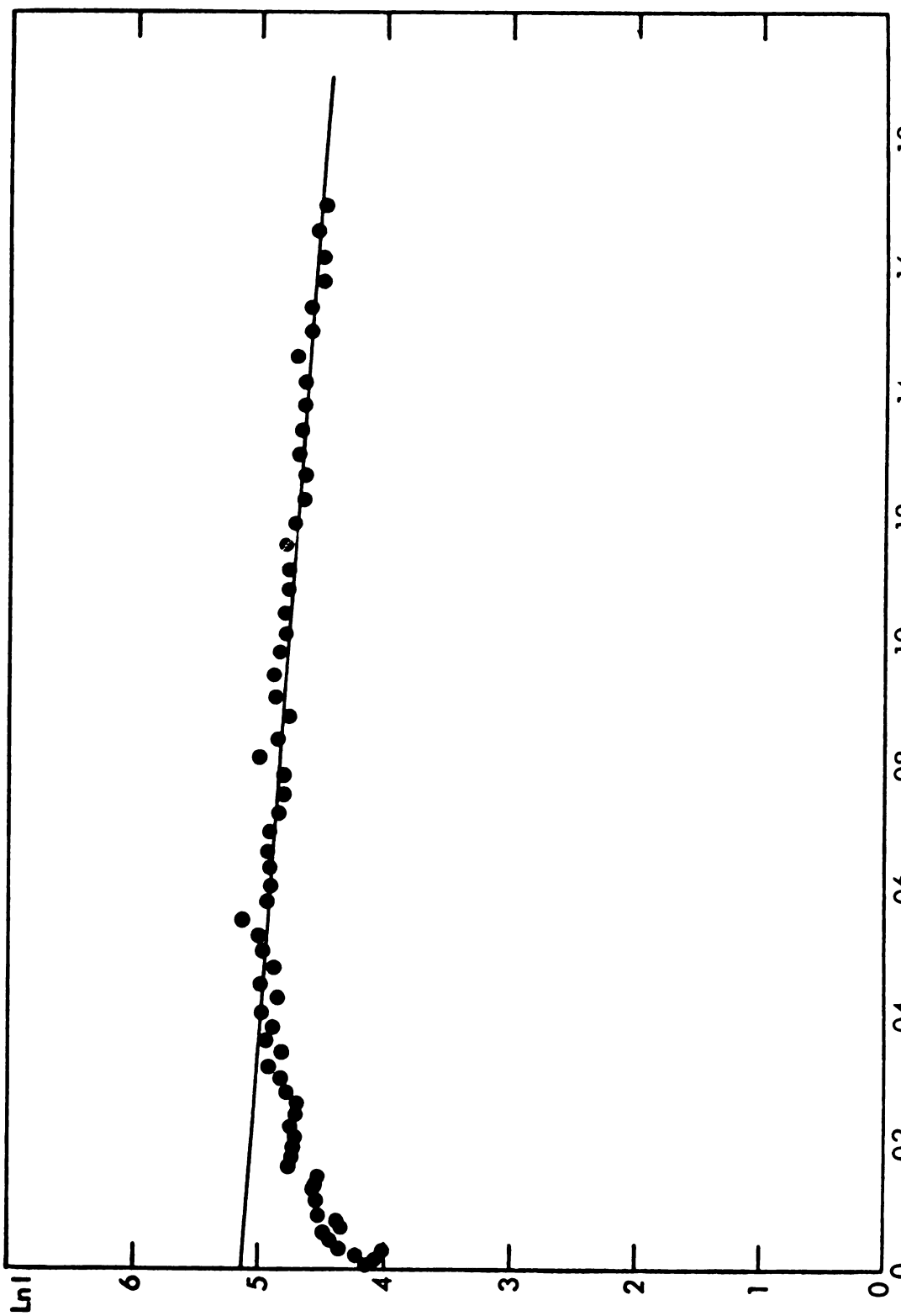

Figure 3.12. Angular dependence of scattered intensity at large angles: Plot of ln I vs s^2 for 0.03% PS/PMMA blend.

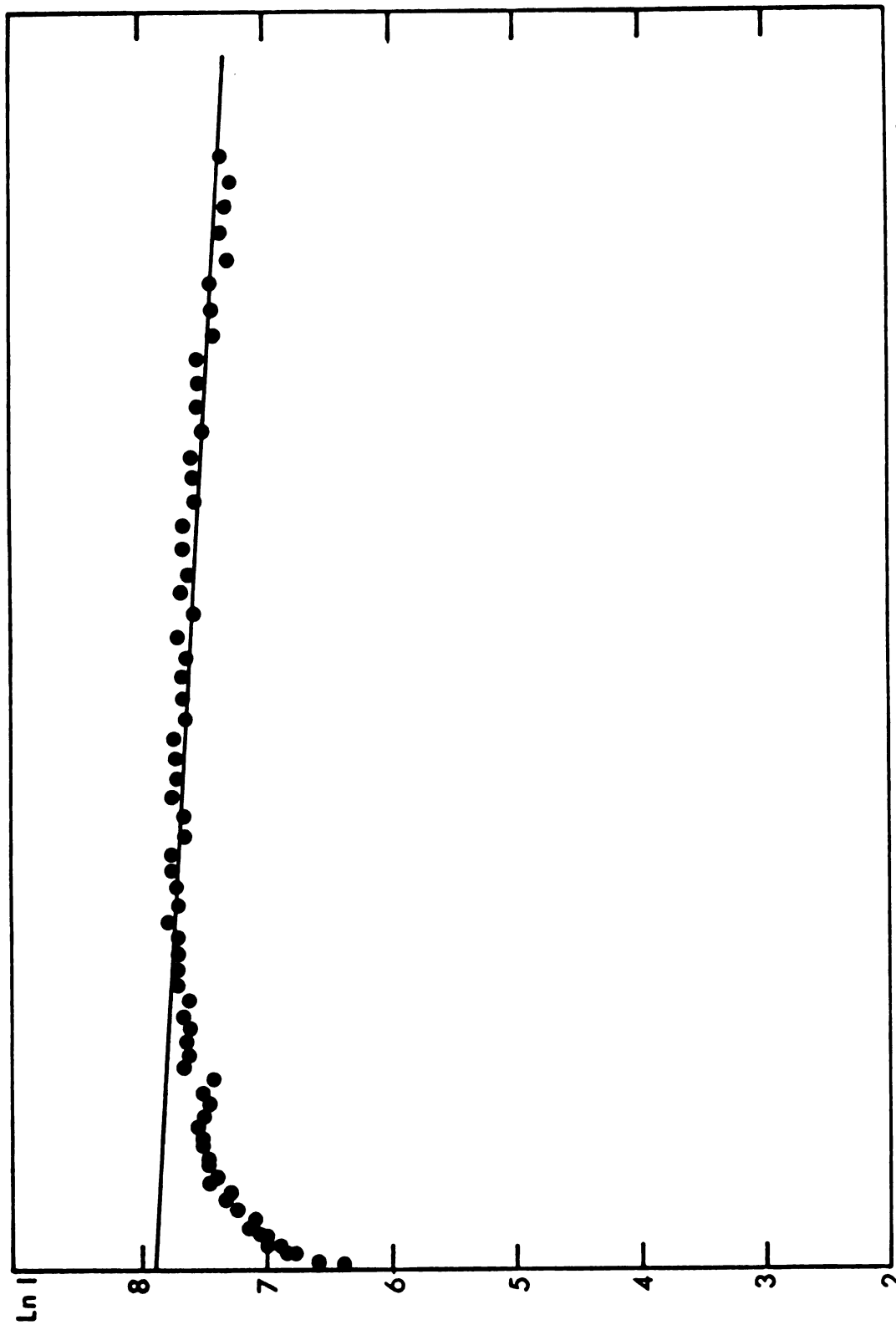

Figure 3.13. Angular dependence of scattered intensity at large angles: plot of ln I vs s^2 for 0.05% PS/PMMA blend.

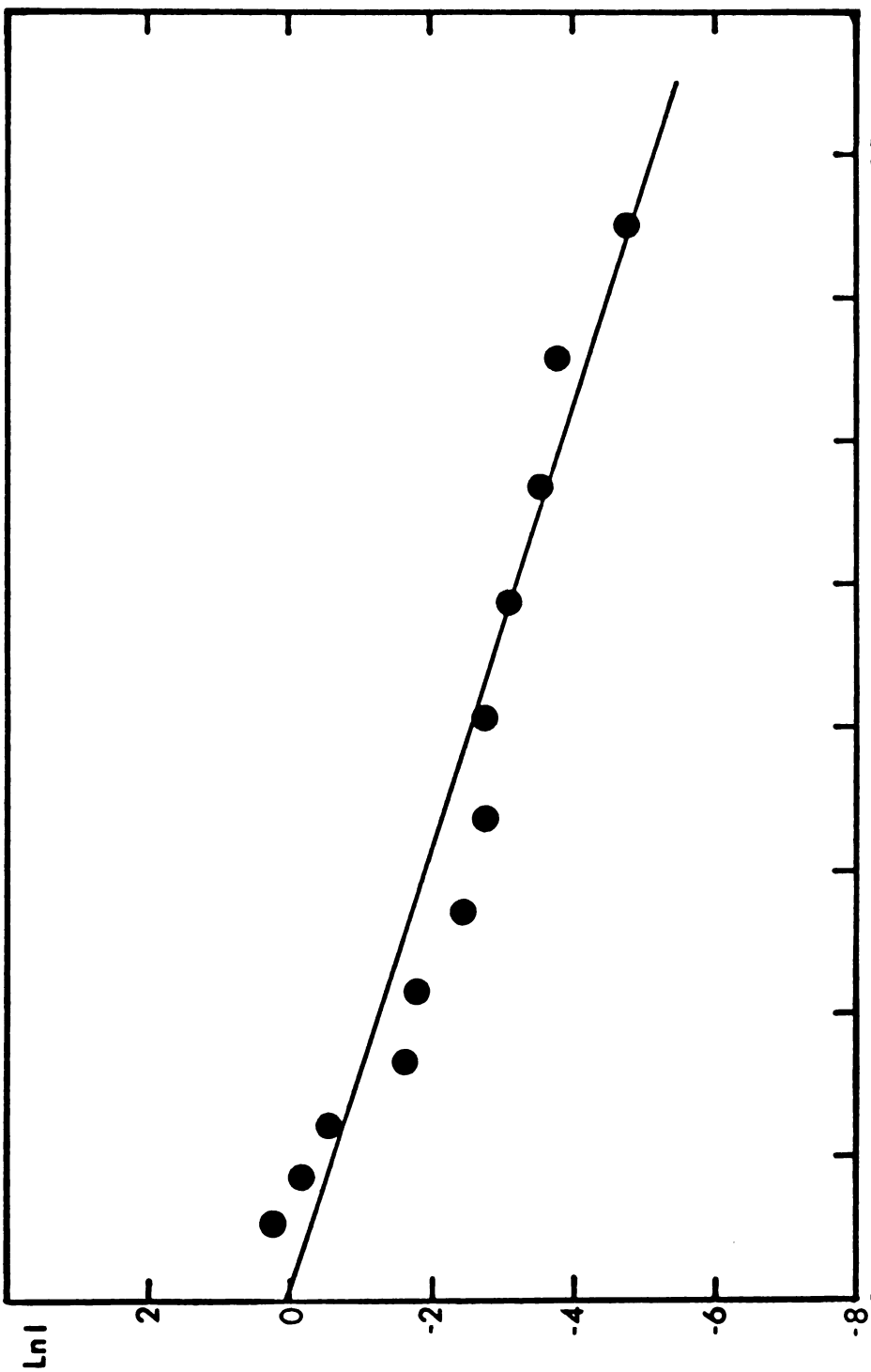

Figure 3.14. Angular dependence of scattered intensity at small angles: plot of ln I vs s^2 x 10^3 for 0.0001% PS/PMMA blend.

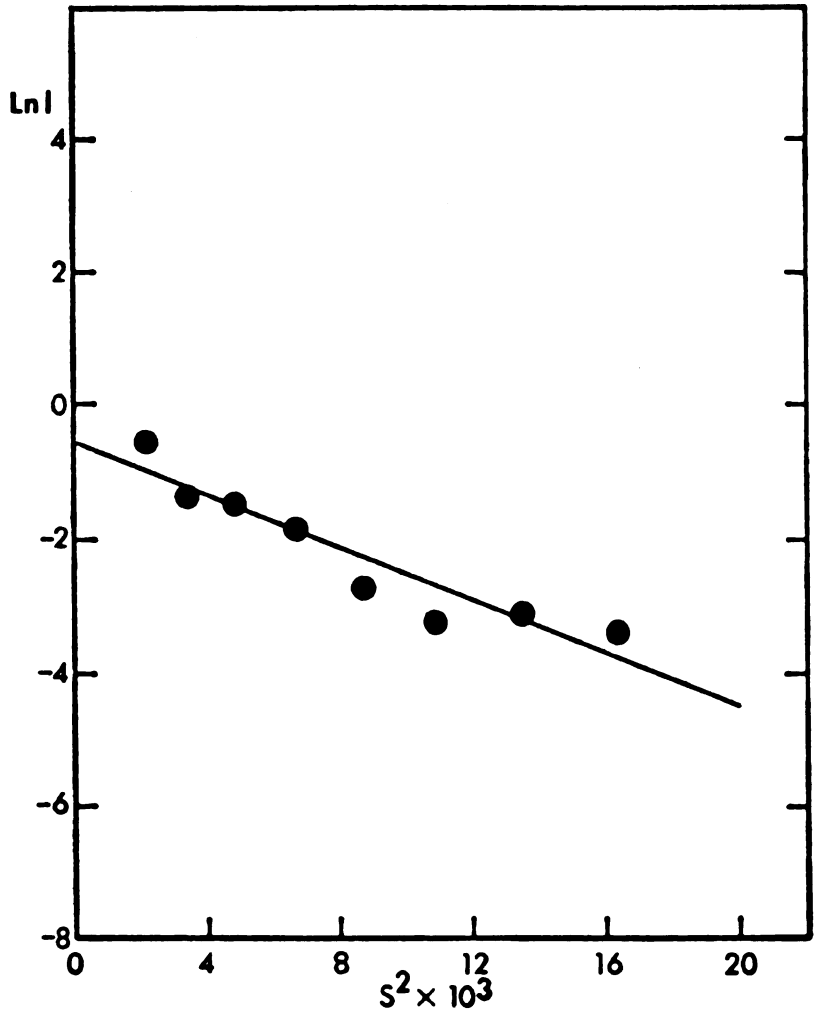

Figure 3.15. Angular dependence of scattered intensity at small angles: plot of ln I vs $s^2 \times 10^3$ for 0.001% PS/PMMA blend.

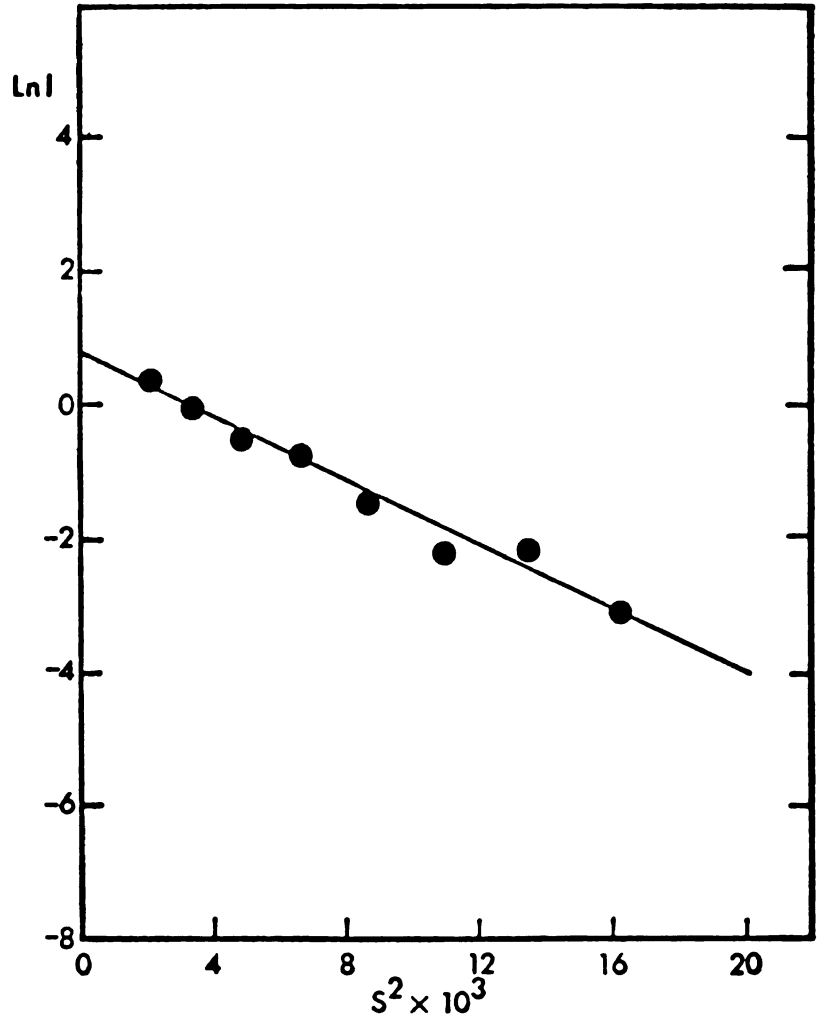

Figure 3.16. Angular dependence of scattered intensity at small angles: plot of ln I vs $s^2 \times 10^3$ for 0.005% PS/PMMA blend.

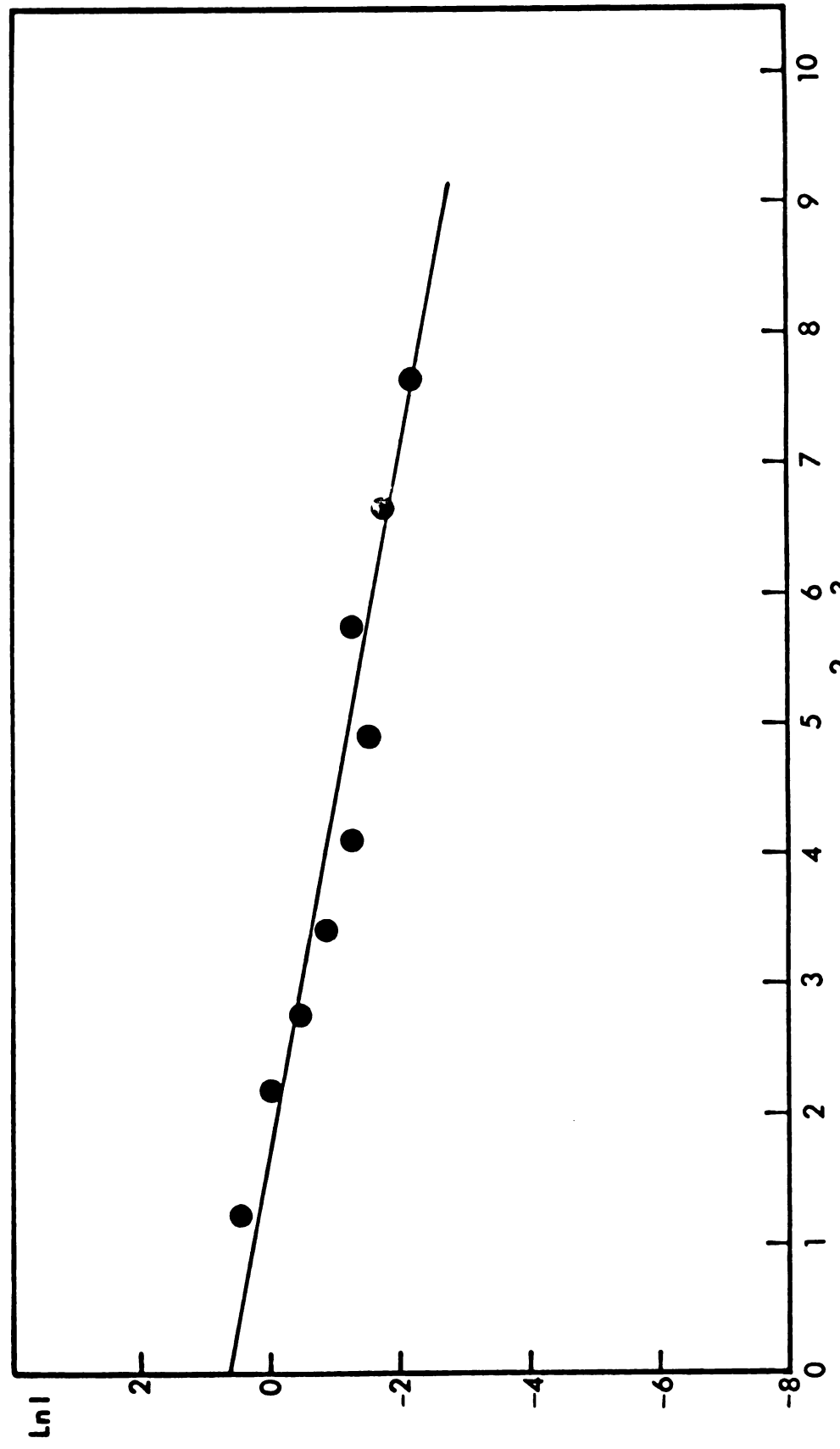

Figure 3.17. Angular dependence of scattered intensity at small angles: Plot of ln I vs $s^2 \times 10^3$ for 0.01% PS/PMMA blend.

$$A_1 = fA$$

and (3.11)

$$A_2 = (1 - f)A \ ,$$

where f is the fractional contribution factor (see equation (3.9)) and A, as defined in Table 3.5, is:

$$A = \frac{I_0 V}{L^2} \langle k \rangle \frac{\langle \delta\epsilon^2 \rangle}{\langle \epsilon \rangle^2} \ .$$

Thus, f was evaluated from A_1 and A_2 by the following equation:

$$f = A_1/(A_1 + A_2) \ . \qquad (3.12)$$

With the knowledge of a_1, a_2, f and the complete correlation function, $F(\rho)$ (see equation (3.9)), the distance of heterogeneity, l_c, and the volume of heterogeneity, v_c, were calculated immediately from equations (3.6) and (3.8) respectively. Integrals involving F7 for different order of ν were solved with the aid of the following equation:

$$\int_0^\infty t^\mu K_\nu(t)dt = 2^{\mu-1}\Gamma\left(\frac{\mu+\nu+1}{2}\right)\Gamma\left(\frac{\mu-\nu+1}{2}\right) \ , \qquad (3.13)$$

if $R(\mu \pm \nu) > -1$.

The knowledge of q_1, q_2, f and the complete correlation function $F(\rho)$ also enables the quantity J, as defined in equation (2.61a), to be determinable from the turbidity expressions shown in Table 3.5. With J, the standard deviation of the refractive index of the sample, $\sqrt{\langle \delta n^2 \rangle}$, was obtained from equation (2.62) with the experimentally

determined turbidity, τ, and the mean refractive index, $\langle n \rangle$, as shown in Table 3.4.

Table 3.7 summarizes the results obtained for the various inhomogeneity parameters pertinent to each of the seven samples under study.

Discussion

It has been mentioned in the last section that if the experimentally determined intensity is plotted according to the scheme shown in the third column of Table 3.6, a straight line should be expected for the correct correlation function. This condition is seen to have been satisfied both by the correlation function determined for the large-angle portion of the intensity distribution (Figs. 3.7-3.13) and F2 ($F2 = \exp[-(\rho/a_2)^2]$) presumed to be describable for the small-angle portion (Figs. 3.14-3.17).

It is unfortunate that the small-angle data of the 0.03% and 0.05% PS/PMMA blends could not be used to yield a physically significant correlation function and hence a long-range correlation distance, a_2. As is apparent from Figs. 3.12-3.13, the data distribute in an opposite fashion from those in the other samples (Figs. 3.8-3.11) even after correction has been made for the effect due to simple attenuation (see Appendix). In view of the extended nature and the opacity of the samples, this phenomenon must be due to multiple scattering and interparticle destructive interference[35] between the scattered intensities.

Table 3.7. Inhomogeneity parameters for pure PMMA and PS/PMMA blends.

Sample	$F(\rho)^*$	q_1	q_2	a_1 (Å)	a_2 (μ)	f	1_c(Å)#	$v_c(\mu^3)$#	$\tau(cm^{-1})$	$\sqrt{\langle \delta n^2 \rangle}$ x10⁴#
PMMA	F1	23.1		6330			12700	6.37	0.00551	0.545
0.0001% PS/PMMA	fF1+(1-f)F2	7.62	50.0	2090	1.37	0.867	6850	2.10	0.0192	1.41
0.001% PS/PMMA	fF1+(1-f)F2	8.13	56.0	2230	1.53	0.939	5840	1.48	0.0326	2.00
0.005% PS/PMMA	fF1+(1-f)F2	11.2	61.6	3070	1.69	0.742	12300	7.47	0.0750	2.05
0.01 % PS/PMMA	fF2'+(1-f)F2	10.3	78.4	2820	2.15	0.996	5130	0.346	0.111	3.94
0.03 % PS/PMMA	F2'	7.56		2070			(3670)	(0.0494)	1.08	(15.0)
0.05 % PS/PMMA	F2'	6.83		1870			(3310)	(0.0364)	2.32	(23.4)

*$F1 = \exp(-\rho/a_1)$; $F2' = \exp[-(\rho/a_1)^2]$;

$F2 = \exp[-(\rho/a_2)^2]$.

#Numbers in parentheses are calculated by assuming f = 1.

In spite of the great controversy about F1 (F1 = $\exp(-\rho/a_1)$), as mentioned previously, it is found to be the best correlation function for the pure PMMA and, at large angles, for the PS/PMMA blends up to a concentration of 0.005% in polystyrene (see second column of Table 3.7). Since F1 is associated with a Markov condition, the former must possess a completely random structure. This simple exponential type of correlation function (F1) was also established for commercial PMMA (Lucite) by Debye and Bueche.[11] However, their measured correlation distance (2800Å) was smaller by a factor 2.3 than that obtained in this study. The discrepancy, as can be seen by comparing against the a_1 value for the 0.0001% PS/PMMA blend, must be due to the impurities associated with the commercial stock. Also, since the Debye sample may not have the same thermal history as ours, the discrepancy is not unexpected. The change in the correlation function (at large angles) from F1 for the blends of 0.01% polystyrene and above definitely implies a more regular structure of these samples than those containing a lower concentration.[36] This is not too surprising, for, as will be discussed below, phase separation has occurred among these samples and so, a change in texture is expected.

The dependence of the inhomogeneity parameters on morphology has been elucidated by Moritani and his coworkers.[26] The authors characterized the inhomogeneities in a series of carefully controlled film specimens of block copolymers

(styrene and isoprene) and graft copolymers (butadiene and styrene-acrylonitrile) from the angular distribution of the scattered intensity by using a correlation function, $F(\rho)$, identical to the one obtained in this study for blends of 0.005% polystyrene and less, namely

$$F(\rho) = f \exp(-\rho/a_1) + (1 - f) \exp[-(\rho/a_2)^2] \ .$$

They then discussed the inhomogeneity parameters in relation to the structures of their specimens observed from electron micrographs. Although the Moritani et al. specimens all have a definite two-phase structure, it is felt that their results can be applied in general to any blend systems of two components characterizable by a common correlation function. The reasoning comes from the fact that a mixture of two polymers of different chemical composition will never truly attain one single homogeneous phase (see "Introduction" of this Chapter). Some of the Moritani conclusions which will be used in the succeeding discussion are as follows:

(1) The larger the size of the domain of the dispersing component, the larger the correlation distances, a_1 and a_2;

(2) the more uniform the dispersion of the domains, the larger the fractional contribution factor "f" and the long-range correlation distance "a_2".

Comparing the values of a_1 and a_2 for the first three blends in our series, as shown in the fifth and sixth

columns of Table 3.7 respectively, it is seen that the extent (i.e. range or distance) of inhomogeneity increases steadily with concentration. This signifies a decrease in compatibility[22] (see "Introduction" of this Chapter) as more polystyrene is present in the polymethyl methacrylate matrix. Moreover, in accord with the Moritani results, this increase in the two parameters may be attributed to a size enlargement of the polystyrene domain which results from the larger concentration and the poorer affinity with the polymethyl methacrylate matrix. The diminution in the fractional contribution factor, f, with the 0.005% blend (see column 7 of Table 3.7) reflects a more pronounced long-range fluctuation in the sample. This suggests that the concentration of polystyrene in this blend is approaching the critical value. The same trend is also suggested by the values of a_1, a_2, and f for the 0.01% polystyrene sample. Following Moritani again, the sudden decrease in the a_1 value** can be explained in terms of precipitation of the polystyrene particles, which is always accompanied by a reduction in size. Furthermore, the value of f being so close to unity shows the extremely uniform dispersion of the praticles in the sample and also accounts for the

---

** Should the short-range correlation function be taken as represented by $F1 = \exp(-\rho/a_1)$, although the data fitted much better with the power spectrum of $F2' = \exp[-(\rho/a_1)^2]$, the value of a_1 would even be smaller being 1200 Å.

increase in the long-range correlation distance, a_2 (see Moritani's second result; last paragraph). The values of the short-range correlation distance, a_1, for the 0.03% and 0.05% blends are smaller than that for the 0.01% sample. However, interpretation and comparison of these values are rendered difficult by the insufficient information obtained for the former two samples. The possibility that the difference in the correlation distance, a_1, is related to the size or the distribution of the molecular weight of the precipitated polystyrene particles is ruled out by the conclusions reached by Bueche.[37] The author studied the effects of concentration and molecular weight on the size distribution of polystyrene "droplets" in polymethyl methacrylate-polystyrene copolymer and that of docosane in polyethyl methacrylate. He found that the size distribution of the droplets was insensitive to these two variables.

Blends containing 0.005% polystyrene or less are transparent, while those containing more than 0.01% are opaque. This fact in conjunction with the changes in the short- and long-range correlation distances (a_1 and a_2) at the 0.01% polystyrene level, as just discussed, suggests that blends of the former kind are compatible while those containing 0.01% or more of polystyrene have undergone phase separation and are therefore incompatible.

The geometrical significance of the distance of heterogeneity, 1_c, and the volume of heterogeneity, v_c, have

been discussed (see section under "Inhomogeneity Parameters"). Substituting equation (3.9) into equations (3.6) and (3.8), it can be seen that these two parameters are strongly dependent on the value of the fractional contribution factor, f. That is the smaller the value of f, the larger are the parameters. This is illustrated in the eighth and ninth columns of Table 3.7.

The turbidity, τ, and the standard deviation of the refractive index, $\sqrt{\langle(\delta n)^2\rangle}$, of each of the samples under study are shown in the tenth and eleventh columns of Table 3.7 respectively. The amplitude of the inhomogeneity (i.e. $\sqrt{\langle(\delta n)^2\rangle}$) in our PMMA sample is smaller than that reported by Debye and Bueche[11] for commercial Lucite (1.7×10^{-4}). This is a direct consequence of the larger extent of the inhomogeneity (measured by the correlation distance, a_1) present in our sample. This can easily be seen from the first turbidity expression shown in Table 3.5. Among the blends, the amplitude of the inhomogeneity is seen to increase with the concentration of polystyrene. This general increase in the amplitude with respect to concentration is predicted by equation (3.3).

Conclusion

The inhomogeneities of pure amorphous PMMA and its blends with various concentrations of amorphous polystyrene, subject to an identical thermal history, have been characterized by studying the angular distribution of the

scattered light intensity. The following conclusions are made.

(1) The simple exponential correlation function of Debye and Bueche is associated only with pure PMMA and at large angles, with the blends containing respectively 0.0001%, 0.001%, and 0.005% of polystyrene. At a concentration of 0.01% polystyrene and above, the blends require a more complex correlation function.

(2) Both the short- and long-range correlation distances (a_1 and a_2) are long with the latter much larger than the former.

(3) The compatibility of the blends decreases with higher concentration of polystyrene.

(4) A trend of behavior opposite to that of the compatibility is observed for the standard deviation in refractive index.

(5) While pure PMMA is completely disordered, blends containing 0.01% or more of polystyrene exhibit a more regular structure than those containing less. Moreover, blends containing 0.005% or less polystyrene are compatible, while those containing 0.01% or more have undergone phase separation and are therefore incompatible.

(6) A size enlargement of the polystyrene domain with concentration is observed among those blends which are compatible. A shrinkage in the domain size is, however, seen after phase separation occurs.

CHAPTER IV

BRILLOUIN SCATTERING IN POLYMETHYL METHACRYLATE AND POLYSTYRENE/POLYMETHYL METHACRYLATE BLENDS

Introduction

Longitudinal acoustical waves are present in every form of matter. They are produced by the adiabatic density fluctuations which are driven thermally by the heat content.[38] When a beam of monochromatic light falls on them, it is scattered when the Bragg condition is satisfied:

$$\lambda_\ell/\langle n\rangle = 2\lambda_s \sin(\theta/2) \quad , \qquad (4.1)$$

where λ_ℓ is the wavelength of light, λ_s the wavelength of the sonic wave, $\langle n\rangle$ the mean refractive index of the medium and θ the angle of scattering. Since the sonic disturbances are propagating in all directions, they can be regarded as sets of "moving mirrors". Based on this principle, L. Brillouin,[39] in 1922, suggested that the scattering of light from these sonic disturbances would be Doppler shifted in frequency according to:

$$\Delta\nu = \pm\, 2\nu_0\langle n\rangle(V_s/c)\sin(\theta/2) \quad , \qquad (4.2)$$

where $\Delta\nu$ is the frequency shift of the scattered light, ν_0 the frequency of the incident light, V_s the velocity

of sound in the medium and c the velocity of light. The factor 2 is included in the equation because the sonic wavetrains form both a moving receiver and a moving source. Substituting equation (4.1) into equation (4.2), it can easily be seen that

$$\Delta\nu = v_s/\lambda_s = \Omega \quad , \qquad (4.3)$$

where Ω is the frequency of the sound wave. From equation (4.1), we also see that the sound wave that can be detected with visible light will have frequency within the gigahertz region.

In addition to the adiabatic disturbances, there are also random entropy fluctuations in a medium. These variations are, however, stationary and hence scatter light quasielastically with no change in frequency. Thus, a typical Brillouin spectrum is a triplet consisting of a central component with the same frequency as the incident light and a pair of Stokes and Antistokes (or just Brillouin) satellites of shifted frequency as given by equation (4.2).

What has been said applies to simple nonrelaxing fluids (i.e. $\omega_B\tau_R<<1$, where ω_B is the angular frequency of the sound wave and τ_R is the relaxation time of the fluid). For a structurally relaxing liquid, such as a polymer, the relaxation time of the molecules at high sonic frequency may be so large (i.e. $\omega_B\tau_R>>1$) that many of the adiabatic modes of motion will be damped and become non-ocillatory. Thus, there are relatively fewer phonon states

in solid polymers[40] than in simple fluids accounting for a much weaker pair of Brillouin components therein. The nonocillatory adiabatic modes of motion will supplement the entropy fluctuations in giving rise to the central peak of the Brillouin spectrum. For polyblends which consist of two components, the central peak should also owe a contribution due to the stationary concentration fluctuations. But this contribution is bound to be small at room temperature (i.e. below the glass transition temperature) because of the extremely low value of the diffusion coefficient under this condition.[41]

Although satisfactory theories of Brillouin scattering in solid amorphous substance are still not available, those in liquids are abundant. The theory of Mountain[42] for relaxing liquids is especially valuable and provides a reasonable description for polymers. According to Mountain, the spectral distribution of the Brillouin components is approximately represented by a sum of two Lorentzian curves:

$$\sigma_B'(k,\omega) = \left\{\frac{[1-c_0^2/V_s^2(1-1/\gamma)]\,[V_s^2k^2+c_0^2/V_s^2\tau_R^2]-(c_\infty^2-c_0^2)k^2}{c_0^4/V_s^4\tau_R + V_s^2k^2}\right\} \times$$

$$\left[\frac{\Gamma_B}{\Gamma_B^2 + (\omega - V_sk)^2} + \frac{\Gamma_B}{\Gamma_B^2 + (\omega + V_sk)^2}\right] . \quad (4.4)$$

where $\sigma_B'(k,\omega)$ is the approximate frequency distribution function of the Brillouin component, c_0 is the low frequency adiabatic sound speed, V_s the phonon speed under

observation, γ the ratio of the specific heat at constant pressure to that at constant volume, c_∞ the infinite frequency sound speed, τ_R the relaxation time of the medium and Γ_B the half width at half height of the Brillouin peak. From equation (4.4), it follows that the intensity of the Brillouin component is:

$$I_B \propto \omega_0^2 \Gamma_B / [(\omega^2 - \omega_0^2)^2 + (2\Gamma_B)^2 \omega^2] \ , \qquad (4.5)$$

where

$$\omega_0^2 - (kV_s)^2 + \Gamma_B^2 = \omega_B^2 + \Gamma_B^2$$

has been substituted.

The half width at half height of the Brillouin component, Γ_B, is the temporal attenuation coefficient, whose reciprocal represents the life time of the sound wave giving rise to the Brillouin effect. The relationship between the spatial attenuation coefficient, α, and the velocity of sound, V_s, is hence given by:[43]

$$\alpha = \Gamma_B / V_s \ . \qquad (4.6)$$

It is obvious that Brillouin scattering is a powerful technique in the study of the acoustical properties of a medium in the gigahertz frequency region which exceeds the limit of 10^8 Hz available to the conventional ultrasonics. By just measuring the shift of the Brillouin component with respect to the central component and the half width at half height of the Brillouin peak, information on the phase velocity of the sound waves in the medium and the sonic attenuation can be obtained from equations (4.2) and (4.6)

respectively. In addition to this well established application, recently Stoicheff,[44] Peticolas,[40] and Romberger[45] reported that the so-called "Landau-Placzek" ratio, that is the ratio of the intensity of the central component to that of the two Brillouin components, was a sensitive probe for structural changes in polymers. Stoicheff, Peticolas and coworkers studied the Landau-Placzek ratio of polyethyl methacrylate and polycyclohexyl methacrylate as a function of temperature and observed a sharp discontinuity in the ratio at the glass transition temperature of the polymer. Romberger extended the study to polymethyl methacrylate and observed a similar break in the ratio at T_g. The values of the ratio they obtained at room temperature are, however, too large to be accounted for by thermodynamical considerations which predict the Landau-Placzek ratio to be given by:[46]

$$\frac{I_c}{2I_B} = \frac{[(\rho \frac{\partial \epsilon}{\partial \rho})_T^2 \cdot (\beta_T - \beta_s)]_{static}}{[(\rho \frac{\partial \epsilon}{\partial \rho})_T^2 \beta_s]_{hs}} \quad , \quad (4.7)$$

where ρ is the density of the medium, ϵ the electric permittivity, T the temperature, β_T the isothermal compressibility, β_s the adiabatic compressibility and the subscripts, static and hs, refer to the low and hypersonic frequency conditions respectively. Accordingly, based on an observation of the Krishnan effect, Romberger suggested that the large value of the ratio at room temperature was due to a nonthermodynamical contribution of the frozen-in

spatial strain which resulted from the volume changes during the polymerization process.

Since spatial strain is in affect the inhomogeneity of a medium, it suggests that samples whose inhomogeneities have been fully characterized (e.g. by the method discussed in Chapters II and III) would be excellent candidates to verify Romberger's point of view. This is one of the purposes of the experiment to be described below. In addition to determining the acoustical properties of the sample, the experiment also attempts to check on the claim that the Landau-Placzek ratio is a sensitive probe to structural changes.

Experimental

Sample Preparation

The samples used in this investigation were pure polymethyl methacrylate and a series of its blends with polystyrene of different concentrations. Details on their preparation and the concentration of the blends have been discussed in Chapter III.

Instrument

The Brillouin spectrometer used in this experiment was the same instrument as described for the low-angle scattering work in Chapter III (Fig. 3.3). Several changes in the collecting optics of the detection system were made, however:

(1) Light pipe

A shorter aluminum pipe of 12 inches was used to collect the scattered light in this case. The pipe was hollow inside but was attached to an adjustable mount on either end. Anchored to each mount was a small variable iris diaphragm which could be adjusted to give a smallest aperture of about 1 mm in diameter. The inner surface of the pipe was painted flat black to minimize reflection.

(2) Fabry Perot interferometer

This unit was the prime resolving device of the spectrometer and was put to function for this investigation. It was a piezoelectric-scan type of interferometer and was manufactured by Lansing Research Corporation. The same company also made the High voltage and linear ramp generator which powered the piezoelectric trnslator. The Fabry Perot mirrors were supplied by Coherent Optics, Inc. They consisted of a pair of matched "Dynasil" plane parallel plates with a flatness of $\lambda/200$, a wedge smaller than 1.0 arc second, 1 inch diameter and thickness of 0.375 inch. The front surface of the plates was coated with "Broad Band Krypton" coating of 1.5-3.0% transmission and 0.1% absorption, while the back surface was with "Antireflection MgF^2" coating of $\lambda/4$ flatness and 98.5% transmission. The front mirror was housed in a Gimbal mount and could be adjusted in orientation by two micrometers. The back mirror was positioned in front of the piezoelectric translator so that it could be translated during scanning.

The scattered light collected by the light pipe was collimated on entering the Fabry Perot interferometer by a 500 mm focal length lens. The entrance of the interferometer was guarded by a large iris diaphragm which stopped the extraneous light. The resolved light rings were focussed by a 1000 mm focal length lens, which was placed right behind the interferometer, to the photomultiplier tube (EMI 9558 B) after passing through an exit pinhole of 2mm in diameter. The pinhole permitted only the center ring of the scattered light pattern to enter the photomultiplier tube and therefore enhanced the resolution of the instrument. Between the lens and the exit pinhole was another large iris diaphragm adjusted to further baffle out the stray light.

Experimental Procedures

Alignment

Before any spectra were obtained, the instrument was first checked for its alignment using the method discussed in Chapter III. After placing the back Fabry Perot mirror in position, the interferometer was adjusted by turning two coarse adjustment knobs until the back reflection of the He-Ne alignment laser beam (Fig. 3.3) coincided with itself. The 500 mm focal length lens was then placed so that the center of the Bridgeport table was on its focal plane. The lens was again centered with respect to the alignment beam

by the back reflection technique. The apertures of the front and the rear iris diaphragms on the light pipe were then adjusted to 1 mm and about 1.5 mm in diameter respectively. With the two Fabry Perot mirrors set at the desired separation and the 1000 mm focal length lens in place, the interferometer was fine tuned with the two micrometers driving the Gimbal mount of the front mirror until a series of concentric rings of high symmetry was obtained. The lens was adjusted to center the ring pattern onto the exit pinhole.

Brillouin Spectra

After the spectrometer had been carefully aligned, the sample in its holder was placed at the center of the Bridgeport table and was illuminated by the green line (λ_0 = 514.5 nm) of the Argon ion laser. The scattering was performed at room temperature (22.5^0C) and at a scattering angle of 90^0. The beam with an output power of 400 mw was incident normally along the cylindrical axis of the sample and the scattered light was observed through its curved surface. Throughout the investigation, the Fabry Perot mirrors were set at a separation of 5.09 mm. The voltage to the photomultiplier was adjusted so that the central peak of the spectrum was within the scale of the recorder chart paper.

Figures 4.1 and 4.2 are representatives of the spectra obtained at a ramp slope of 2.5 v/sec and at full speed of

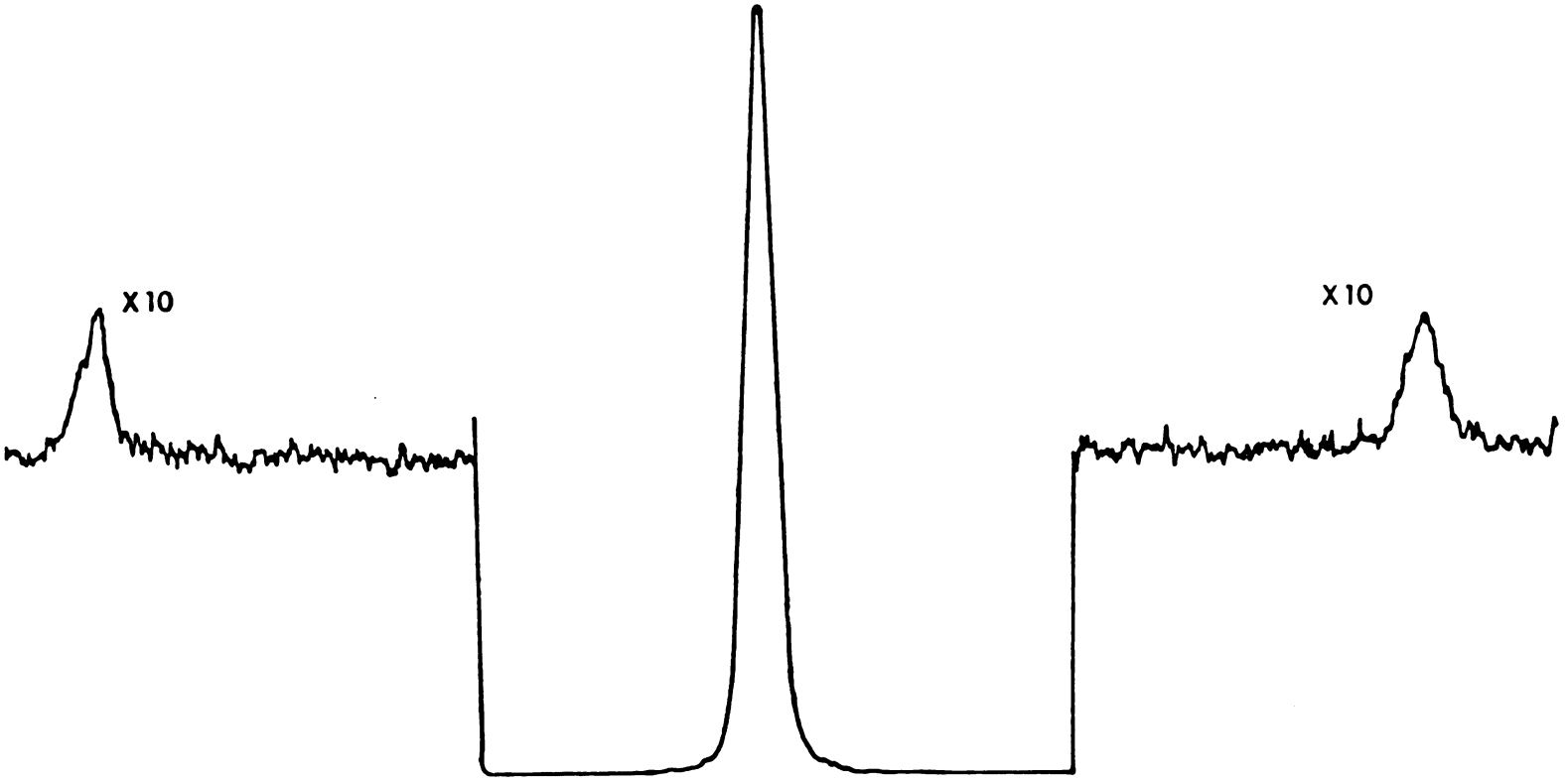

Figure 4.1. Brillouin spectrum of pure PMMA.

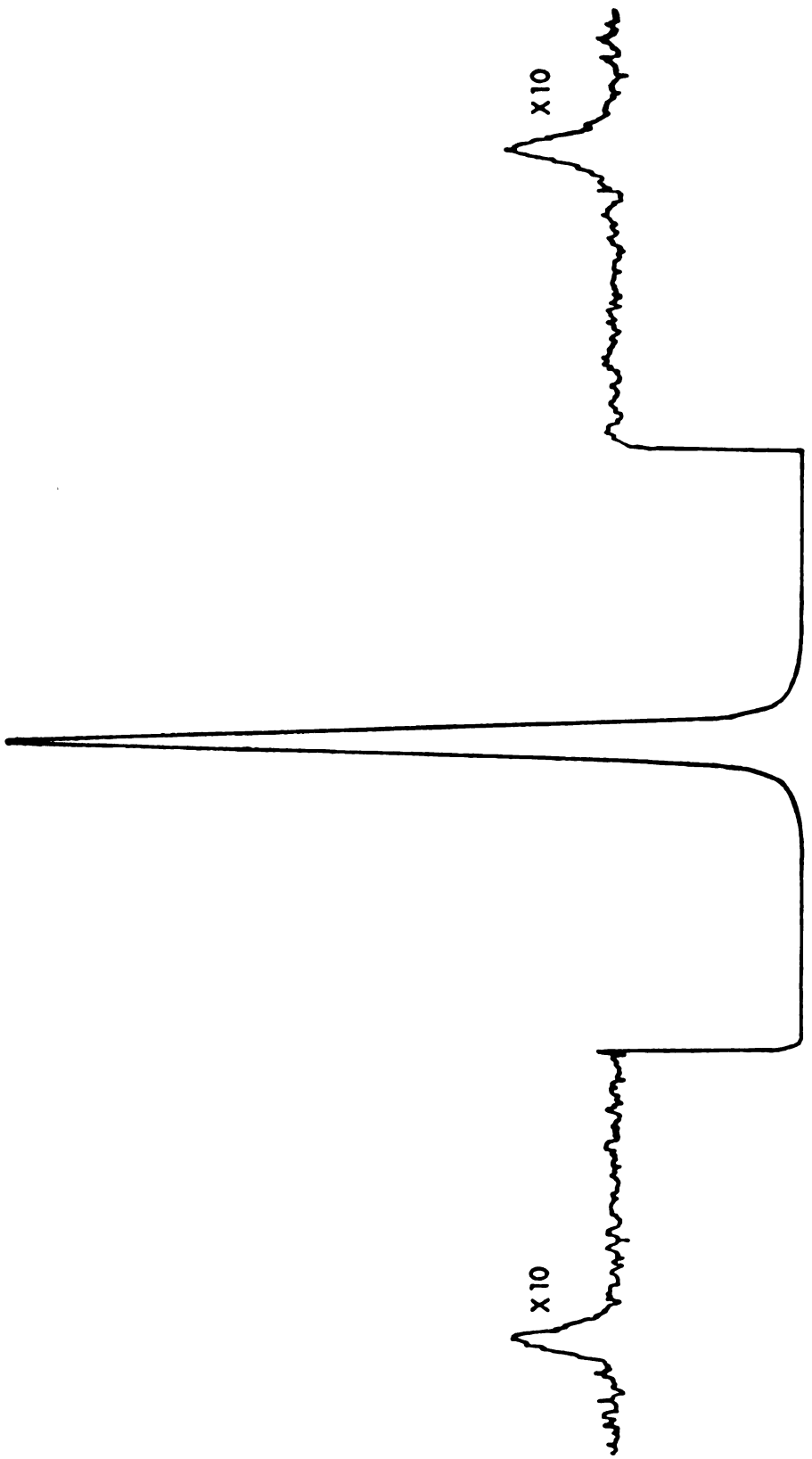

Figure 4.2. Brillouin spectrum of 0.005% PS/PMMA blend.

the recorder. They are for pure PMMA and the 0.005% PS/PMMA blend respectively. As can be seen, the central peak is quite symmetrical indicating a nearly perfect alignment of the interferometer. The two side peaks are the Brillouin components which arise from the propagating sonic disturbances. They have been amplified by ten fold because of their small size in comparison to the central peak. The amplification was achieved by changing the input head setting of the picoammeter from an initial value of 10^{-9} amp to 10^{-10} amp.

With the chosen separation between the Fabry Perot mirrors, the Brillouin peaks were well resolved from the central one and the zero level of the spectrum was very flat (Figs. 4.1-4.2). Using the definition of "fineness" by Born and Wolf[47] as the ratio of the separation between the central peaks of two successive orders (i.e. the free spectral range) to the full width at half height of the same peak, our spectra all yielded a resolution of about 45.

The Brillouin frequency shift, the full widths at half height of the Brillouin and the central components and the free spectral range were obtained by successive geometrical biseections of the peak height (i.e. the distance between the peak apex and the zero level line of the peak) and the full peak width at half height, and were then measured carefully with a pair of calipers. The true width of the Brillouin component was taken to be the difference between its observed spectral width and that of the central peak.[48]

This is based on the fact that the recorded spectrum is a convolution product of the true spectrum with the instrumental response function; since the true central peak, which is very narrowly spread in frequency, cannot be resolved with the interferometric technique, the observed central component represents essentially the response function. The approximation is further rendered possible by the almost Lorentzian line shape of the Brillouin component. The shift and width measurements were converted to frequency units by the following equation for the free spectral range of the spectrum:

$$\Delta f = c/(2l_0) \text{ Hz} \quad , \qquad (4.8)$$

where Δf was the free spectral range in Hz, c the velocity of light and l_0 the Fabry Perot mirror separation in cm. The average values of the Brillouin frequency shifts and the linewidths from three orders of the spectrum were used to calculate the velocity and the attenuation coefficient of sound in each sample from equations (4.2) and (4.6) respectively using the refractive index listed in Table 3.4.

To obtain the intensity of the central peak and the Brillouin doublet, a base line was drawn by extending the zero level line on one side of the peak to that on the other side. The area so marked off under each peak was carefully measured with a planimeter until reproducible readings were obtained. The Landau-Placzek ratio was then calculated by

taking the average of the intensity ratios of the central peak to the sum of the two Brillouin components over four orders of the spectrum (three were obtained with a ramp slope of 2.5 v/sec while the other one was with 0.75 v/sec).

Polarized and Depolarized Brillouin Spectra

With the operation condition of the instrument remaining unchanged, these spectra were obtained by placing a calibrated analyzer behind the exit pinhole of the spectrometer. The analyzer consisted of a piece of green Polaroid framed on a graduated and rotatable mount. When the analyzer was rotated to 0^0 position, only the vertically polarized component of the scattered light would be admitted to the photomultiplier tube and the polarized spectrum was traced by the recorder. The depolarized (i.e. horizontally polarized) spectrum was obtained with the analyzer set at 90^0 position.

Figures 4.3A and B illustrate respectively the polarized and the depolarized spectra obtained for pure PMMA, while Figures 4.4A and B for the 0.005% PS/PMMA blend. As can be seen the triplet characteristic is still obvious with the polarized spectrum but disappears in the depolarized spectrum. This shows the completely polarized nature of the Brillouin satellites.[5] Throughout the experiment, for the reason and by the method discussed in the previous section, the polarized Brillouin peaks and the depolarized central peak were recorded with a ten fold amplification.

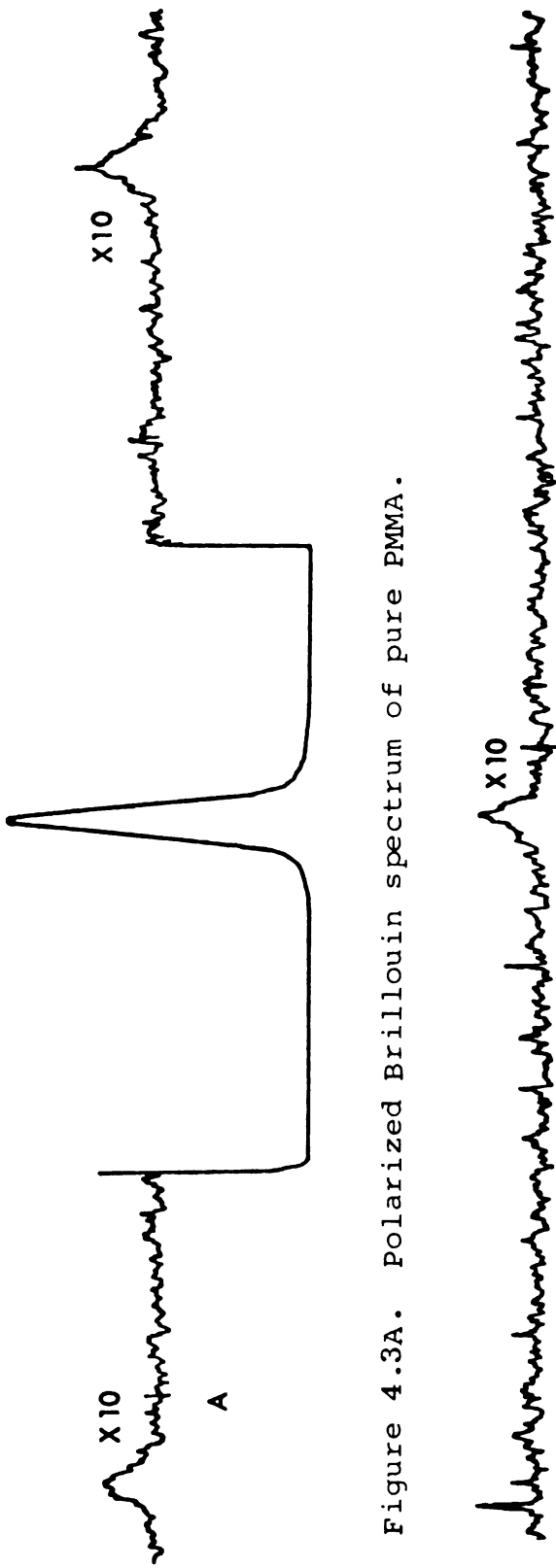

Figure 4.3A. Polarized Brillouin spectrum of pure PMMA.

Figure 4.3B. Depolarized Brillouin spectrum of pure PMMA.

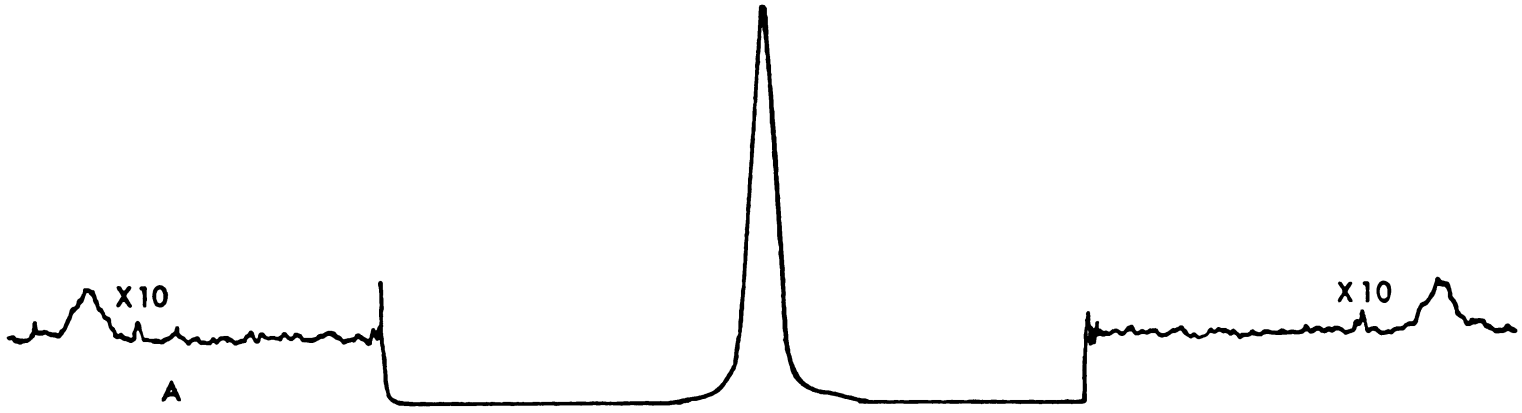

Figure 4.4A. Polarized Brillouin spectrum of 0.005% PS/PMMA blend.

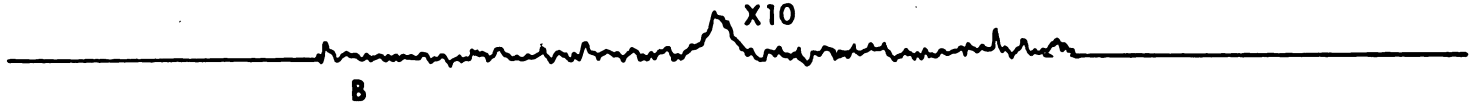

Figure 4.4B. Depolarized Brillouin spectrum of 0.005% PS/PMMA blend.

By measuring the total area under the three peaks in the polarized spectrum in the same manner as described for obtaining the Landau-Placzek ratio in the last section, the total intensity of the scattered light whose polarization vector, like that of the incident beam, was oriented perpendicular to the scattering plane (i.e. V_V) was obtained. Similarly, the area under the only central component in the depolarized spectrum was determined and represented the total intensity of the horizontally polarized (i.e. polarization vector in the scattering plane) component of the scattered light, H_V. The depolarization ratio, ρ_V, of the sample was then calculated by taking the average of the ratios of H_V to V_V over three orders of the spectra.

Results and Discussion

With reference to Figures 4.1 and 4.2, it is obvious that our spectra are characterized by a triplet structure. There are no peaks whatsoever in the immediate neighborhoods between the central component and the two Brillouin satellites indicating that the scattering which arises from the transverse sound waves in the medium, as seen by Flubacher et al.[49] in fused quartz, has not been observed in our case.

The hypersound phase velocities of the longitudinal sound waves in pure PMMA and in the various PS/PMMA blends under study, as determined from the Brillouin frequency shifts, are listed in the second column of Table 4.1.

Table 4.1. Observed velocities, temporal attenuation coefficients, life times and spatial attenuation coefficients of the longitudinal sound waves in pure PMMA and PS/PMMA blends.

Sample	V_s (m/sec)	$\Gamma/2\pi$ (Mc/sec)	$\tau \times 10^{10}$ (sec)	$\alpha \times 10^{-2}$ (cm^{-1})
PMMA	2913 ± 47	65 ± 20	24 ± 7	14 ± 4
0.0001% PS/PMMA	2926 ± 34	57 ± 15	28 ± 7	12 ± 3
0.001% PS/PMMA	2920 ± 23	56 ± 17	29 ± 9	12 ± 4
0.005% PS/PMMA	2937 ± 23	41 ± 20	39 ± 19	8 ± 4

Within experimental errors, they do not depend on the concentration of polystyrene in the PMMA matrix. Rather, they vary by less than 0.5% about an average value of 2924 m/sec. Friedman et al.[50] reported a value of 2870 m/sec at 20°C (or 2862 m/sec at 22.5°C) for PMMA when studied with a He-Ne laser source of 632.8 nm in wavelength which corresponded to a sound wave frequency of 9.58×10^9 Hz. Since our experiment was done with a 514.5 nm wavelength Argon light source probing an average sound wave frequency of 1.21×10^{10} Hz, the 2% difference between our value and that of Friedman et al. must be associated with the dispersion of the sound velocity between the two frequencies.

In the same Table as the velocities, but in the third, fourth and fifth columns respectively, are the temporal attenuation coefficients, the life times and the spatial attenuation coefficients of the longitudinal sound waves in the samples investigated. As can be seen, the smallness of the Brillouin doublet of our spectra, even after a ten fold amplification, barely enables us to measure their half widths at half height, $\Gamma/2\pi$, prescisely. Although this temporal attenuation coefficient appears to range from 65 Mc/sec for pure PMMA to 41 Mc/sec for the 0.005% PS/PMMA blend, the trend is just not obvious because of the huge uncertainties involved. The same argument also applies to the life time, τ, and the spatial attenuation coefficient, α. In fact, the constancy of the sound velocity among the samples implies little effect on their

viscosity due to the inclusion of the various amounts of polystyrene in the PMMA matrix. Since the behavior of the longitudinal sound velocity and its spatial attenuation coefficient with respect to viscosity are similar[41] (i.e. they increase as the viscosity increases), it is more reasonable and safer to say that no trend of any change exists among the temporal attenuation coefficients, the life times and the spatial attenuation coefficients of the longitudinal sound waves in the samples. As a result, it would be better to report their average values as 55 Mc/sec, 30×10^{-10} sec and 1162 cm^{-1} respectively.

The ± values associated with the parameters shown in Table 4.1 represent their respective root mean square deviation from the average obtained over three orders of the spectrum. For a reason which will become obvious below, it was extremely difficult to obtain any Brillouin spectra for PS/PMMA blends higher than 0.005%. Hence, no results on their acoustical properties are reported in Table 4.1.

In spite of the large uncertainties in the Brillouin half width measurements, fairly good precision was obtained with the Landau-Placzek ratios which are summarized in the second column of Table 4.2. As can be seen, they are large in value as Stoicheff,[44] Peticolas[40] and Romberger[45] have found with methacrylate polymers. Our ratio of 21.8 for pure PMMA is comparable with Romberger's 30 for commercial PMMA for the following two reasons. Firstly, our experiment was performed at a temperature of 2.5°C higher which,

Table 4.2. Observed Landau-Placzek ratios and depolarization ratios for pure PMMA and PS/PMMA blends.

Sample	Landau-Placzek Ratio	ρ_v
PMMA	21.8 ± 0.8	0.016 ± 0.001
0.0001% PS/PMMA	42.2 ± 0.7	0.014 ± 0.001
0.001% PS/PMMA	30.8 ± 0.7	0.022 ± 0.001
0.005% PS/PMMA	33.6 ± 0.6	0.013 ± 0.001

Table 4.3. Comparison between the observed Landau-Placzek ratios and $1/2(q_2 + q_1)$ for pure PMMA and PS/PMMA blends.

Sample	q_1	q_2	$\frac{1}{2}(q_2+q_1)$	Landau-Placzek Ratio
PMMA	23.1		23.1*	21.8
0.0001% PS/PMMA	7.62	50.0	28.8	42.2
0.001 % PS/PMMA	8.13	56.0	32.1	30.8
0.005 % PS/PMMA	11.2	61.6	36.4	33.6

*Since the complete correlation function for PMMA is represented by one simple exponential function, the q obtained may be regarded as equivalent to $1/2(q_2 + q_1)$.

according to Romberger's results, should have a slightly lowering effect on the ratio. Secondly, commercial PMMA may contain impurities. The effect of foreign inclusions on the value of the ratio is obvious from our results for the PS/PMMA blends. For instance, it only takes 10 ppm of impurities to alter the ratio to the value obtained by Romberger.

Recalling the result we obtained in the last experiment (Chapter III), namely the inhomogeneity of the sample increases with the polystyrene concentration in the PMMA matrix, it is apparent already, except for the 0.0001% PS/PMMA blend, that the Landau-Placzek ratio is dependent on the inhomogeneity. This fact is even more obvious when the ratio is compared with $\frac{1}{2}(q_2 + q_1)$, where q_2 and q_1, like the ratio itself, are dimensionless and are related respectively to the long- and short-range correlation distances, a_2 and a_1, of the sample discussed in Chapter III by the following equations:

$$q_2 = 2\langle k\rangle a_2$$

$$q_1 = 2\langle k\rangle a_1 \quad ; \quad \text{with} \quad \langle k\rangle = 2\pi\langle n\rangle/\lambda_0 \ ,$$

where $\langle n\rangle$ is the mean refractive index of the sample and λ_0 is the wavelength of the incident light in vacuum. Table 4.3 restates the values of q_2 and q_1 obtained for each of the samples (see Table 3.7) and shows the comparison between the Landau-Placzek ratio and $\frac{1}{2}(q_2 + q_1)$. A least square fit between the two quantities, assuming a

direct proportional relationship, yielded an astonishing slope of unity (i.e. L.P.R. = $A\frac{1}{2}(q_2 + q_1)$, with $A = 1.0 \pm 0.1$)! As yet, there is no theory that can account for this correspondence. It seems that the failure of the Brillouin scattering theory and the theory of light scattering in amorphous solids in providing a prediction of this kind is associated with the fact that the former is developed without regard to the spatial correlation while the latter neglects the time correlation entirely. In other words, the imperfection is inherent with their concern only with the autocorrelation of the fluctuations in the electric permittivity in space and time domain respectively, and not with the cross correlation at two space-time points, which, as Van Hove[51] has pointed out, is exactly what the scattered intensity should depend on.

On the attempt to record the Brillouin spectrum of the 0.01% PS/PMMA blend, it was found that the central peak increased so much in intensity that the voltage to the photomultiplier tube had to be reduced considerably in order to include it within the scale of the recorder chart paper. As a result, the Brillouin doublet could be seen only with a 100-fold amplification and the Landau-Placzek ratio took a huge value of about 4800. Taking equation (4.7) into account and recalling that near the critical point β_T increases strongly while β_s changes only slightly, the abrupt increase in the ratio must imply, as our first experiment (see Chapter III) predicts, that phase separation has

occurred with such a concentration level of polystyrene in the blend. This interpretation is, to some degree, also supported by a Landau-Placzek ratio of about 4000 obtained by Mohr et al.[52] for SF_6 in the vicinity of the critical point.

Listed in the third column of Table 4.2 are the depolarization ratios, ρ_v, obtained from the depolarized and polarized spectra of the samples. As can be seen, they are very small and are practically unaffected by the polystyrene. The $\pm$ values indicated in the the Table are again the root mean square deviations about the average ratios. Since the depolarization ratio is a measure of the molecular anisotropy, it is concluded that the molecules of our samples are highly isotropic.

Conclusion

The investigation of the Brillouin spectra of pure PMMA and a series of PS/PMMA blends with a maximum polystyrene concentration of 50 ppm indicates that the longitudinal sound waves in the samples are propagating and decaying with about the same phase velocity and attenuation coefficient. The depolarization ratio measurements from the depolarized and polarized Brillouin spectra also suggest a high scale of molecular isotropy in the samples. In conjunction with the results obtained from the regular light scattering experiment, the Landau-Placzek ratio is seen to be a sensitive probe to structural changes in

amorphous polymers, as Stoicheff, Peticolas and coworkers have suggested, and is related, at least qualitatively, with the inhomogeneity (or the frozen-in spatial strain concluded by Romberger) present in the sample. A quantitative correspondence between the intensity ratio and the extent of the inhomogeneity is speculated to exist, although the present status of the light scattering theories is not adequate enough for its prediction or subsequent analysis.

CHAPTER V

PROPOSALS FOR FURTHER STUDY

The experiment discussed in Chapter III has demonstrated the possibility of characterizing the inhomogeneity in a medium. The difficulty involved in obtaining the long-range correlation function for the 0.03% and the 0.05% PS/PMMA blends suggests that thin films of these cloudy samples should be investigated. In principle, multiple scattering and destructive interference are less severe in films than in extended cylinders and therefore, more precise measurements on the scattered intensity at small angles would be feasible. However, with films, some correction factors to be described in the Appendix for the scattered intensity will no longer hold and reference should be made to the article by Stein and Keane.[53]

The supermolecular nature of the short- and long-range correlation distances is obscure in physical reality in comparison to the end-to-end distances of the polymethyl methacrylate and polystyrene molecules. Enlightenment in this respect is therefore very desirable. Electron microscopy which can measure down to 0.01 μ scale is the most powerful technique for this purpose provided that successful microtone sections of sample can be prepared and stained.

The electron micrographs not only will provide a direct visual evidence on the inhomogeneity, but also show the fine structures of the sample. The knowledge on the latter will help to develop a model whereby the correlation function can be formulated with a more precise basis and hence, eliminate many difficulties in the interpretation of the results.

One other aspect of the experiment that deserves a further investigation is the thermal history dependence of the inhomogeneity. In Chapter III, the samples have been prepared with an identical thermal history and the effect of composition on inhomogeneity has been studied. But it is a well known fact that the degree of inhomogeneity in polymers or polyblends is also greatly affected by different heat treatment. Thus, a study in this respect will provide another realm of useful information on the morphology of amorphous solids and its evolution so involved.

The speculation on the correspondence between the Landau-Placzek ratio and the simple average of the long and short extent of inhomogeneity (i.e. $\frac{1}{2}(q_2 + q_1)$), as discussed in Chapter IV, definitely needs more experimental and theoretical verification. A new rigorous Brillouin scattering theory taking into consideration the cross correlation function of the permittivity fluctuations at two space-time points should be developed for the prediction of the mutual relationship of this kind.

BIBLIOGRAPHY

BIBLIOGRAPHY

(1) J. Tyndall, Phil. Mag. 37, 384 (1869).

(2) Lord Rayleigh, Phil. Mag. 41, 447 (1871).

(3) Lord Rayleigh, ibid. 12, 81 (1881).

(4) C. C. Gravatt, Appl. Spectry. 25, 509 (1971).

(5) H. Z. Cummins and R. W. Gammon, Appl. Phys. Letters 6, 171 (1965).

(6) G. Ross, Optica Acta 15, 451 (1968).

(7) F. Zernike, (Thesis), Proc. Acad. Sci. Amsterdam 17, 793 (1916).

(8) N. Wiener, Acta Math., Stockh. 55, 117 (1930).

(9) A. Khintchine, Math. Annln. 109, 604 (1934).

(10) J. L. Doob, "Stochastic Process," John Wiley and Sons, Inc., New York, New York, 1953.

(11) P. Debye and A. M. Bueche, J. Appl. Phys. 20, 518 (1949).

(12) A. Guinier and G. Fournet, "Small-Angle Scattering of X-Rays," John Wiley and Sons, Inc., New York, New York, 1955.

(13) J. A. Stratton, "Electromagnetic Theory," Mcgraw Hill Book Company, Inc., New York, New York, 1941.

(14) A. D. Wheelon, Proc. Inst. Radio Engrs. 43, 1459 (1955).

(15) W. C. Hoffmann, I. R. E. Trans. Antannas Propag. 7, s301 (1959).

(16) P. H. Morse and H. Feshbach, "Methods of Theoretical Physics," Mcgraw Hill Book Company, Inc., New York, New York, 1953.

(17) E. T. Whittaker and G. N. Watson, "A Course in Modern Analysis," Cambridge University Press, London, 1946.

(18) G. Arfken, "Mathematical Methods for Physicists," Academic Press, New York, New York, 1968.

(19) T. A. Grotenhuis, U. S. Patent 2,457,097 (1948).

(20) P. J. Flory, "Principles of Polymer Chemistry," Cornell University Press, Ithaca, 1953.

(21) A. R. Shultz, Am. Chem. Soc. Div. Polymer Chem., Preprints 1455 (Sept. 1967).

(22) A. J. Yu, "Multicomponent Polymer Systems," Advance in Chem. series 99, American Chemical Society, Washington D.C., 1971.

(23) G. Porod, Kolloid - Z. 124, 83 (1951).

(24) P. Debye, H. R. Anderson, Jr. and H. Brumberger, J. Appl. Phys. 28, 679 (1957).

(25) G. Ross, Optica Acta 16, 95 (1969).

(26) M. Moritani, T. Inoue, M. Motegi and H. Kawai, Macromolecules 3, 433 (1970).

(27) T. C. Warrens and W. Prins, ibid. 5, 506 (1972).

(28) S. Gaumer, Ph.D. Thesis, Michigan State University (1972).

(29) V. I. Tatarski, "Wave propagation in a Turbulent Medium," Mcgraw Hill Book Company, Inc., New York, New York, 1961.

(30) E. Beebe and R. H. Marchessault, J. Appl. Phys. 35, 3182 (1964).

(31) A. E. M. Keijzer, J. J. van Aartsen and W. Prins, ibid. 36, 2874 (1965).

(32) E. V. Beebe, R. L. Coalson and R. H. Marchessault, J. Polym. Sci., Part C 13, 103 (1966).

(33) L. G. Shaltyko, A. A. Shepelevskii and S. Ya. Frenkel, Vysokomol. soyed. A12, 1581 (1970).

(34) V. A. Nicely and J. L. Dye, J. Chem. Ed. 48, 443 (1971).

(35) R. Duplessix, C. Picot and H. Benoit, J. Polym. Sci., Part B 9, 321 (1971).

(36) A. Peterlin, Makromol. Chemie 87, 152 (1965).

(37) F. Bueche, J. Colloid Interface Sci. 34, 316 (1970).

(38) G. Benedek and T. Greytak, Proc. IEEE 53, 1623 (1965).

(39) L. Brillouin, Ann. Phys. 17, 88 (1922).

(40) J. N. Gayles and W. L. Peticolas, "Light Scattering Spectra of Solids," G. B. Wright, Ed. (p. 715), Springer - Verlag, New York, New York, 1969.

(41) I. L. Fabelinskii, "Molecular Scattering of Light," Plenum Press, New York, New York, 1968.

(42) R. D. Mountain, J. Res. Nat. Bur. Stand. 70A, 207 (1966).

(43) G. I. A. Stegeman, W. S. Gornall, V. Volterra and B. P. Stoicheff, J. Acoust. Soc. Am. 49, 979 (1971).

(44) W. L. Peticolas, G. I. A. Stegeman and B. P. Stoicheff, Phys. Rev. Letters 18, 1130 (1967).

(45) A. B. Romberger, D. P. Eastman and J. L. Hunt, J. Chem. Phys. 51, 3723 (1969).

(46) H. Z. Cummins and R. W. Gammon, J. Chem. Phys. 44, 2785 (1966).

(47) M. Born and E. Wolf, "Principles of Optics," Pergamon Press, New York, New York, 1964.

(48) R. Y. Chiao and B. P. Stoicheff, J. Opt. Soc. Am. 54, 1286 (1964).

(49) P. Flubacher, A. J. Leadbetter, J. A. Morrison and B. P. Stoicheff, Int. J. Phys. Chem., Solids 12, 53 (1960).

(50) E. A. Friedman, A. J. Ritger and R. D. Andrews, J. Appl. Phys. 40, 4243 (1969).

(51) L. Van Hove, Phys. Rev. 95, 249 (1954).

(52) R. Mohr, K. H. Langley and N. C. Ford, Jr., J. Acoust. Soc. Am. 49, 1030 (1971).

(53) R. S. Stein and J. J. Keane, J. Polym. Sci. 17, 21 (1955).

APPENDIX

APPENDIX

CORRECTION FACTORS FOR ANGULAR SCATTERED INTENSITY

In Chapter III, the relative scattered intensity was studied as a function of the scattering angle. To obtain the actual intensity, $I(s)$, from the apparent measured value, $I_{meas}(s)$, corrections must be made for the effects due to (1) the refraction of the scattered light at the exit surface of the sample, (2) the angular dependence of the scattering volume and (3) the reflection of the incident and the scattered light at the interfaces of the sample. Denoting the correction factors by C_n, C_V, and C_R respectively the actual intensity is given by:

$$I(s) = I_{meas}(s) \times C_n \times C_V \times C_R \quad . \qquad (A.1)$$

Refraction Correction

There are two sources of error due to refraction that may affect the angular intensity mesurements. The refraction at the exit surface of the sample (see Fig. A.1) renders the scattering angle, α, read from the Bridgeport table only apparent. If $\langle n \rangle$ is the mean refractive index of the sample at the wavelength of the incident light,

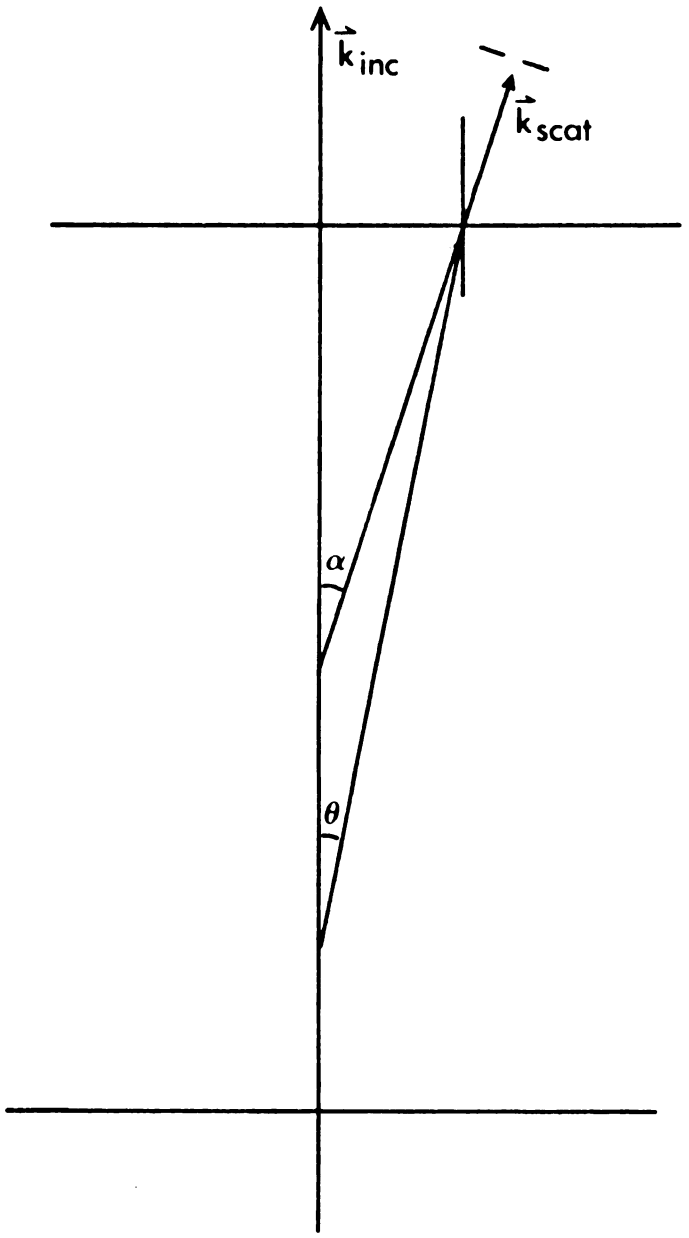

Figure A.1. Ray diagram for scattering angle correction.

it follows from the Snell law that the real scattering angle, θ, is given by:

$$\sin\theta = \sin\alpha/\langle n\rangle$$

or

$$\theta = \sin^{-1}(\sin\alpha/\langle n\rangle). \qquad (A.2)$$

The quantity s defined in equation (2.49a) is therefore:

$$s = 2\sin(\theta/2) = 2\sin[\sin^{-1}(\sin\alpha/\langle n\rangle)/2] \ .$$

The other error that is due to refraction arises from the fact that the cone of light perceived by the light pipe in the presence of the refracting sample is dependent on the apparent scattering angle, α. In Figure A.2, the angle confining the cone of light on the horizontal plane is represented by 2γ for the case of no refraction and by $(\epsilon + \delta)$ when there is refraction. From the figure, it can be seen that

$$BA >> AY$$

and

$$CS >> SR \ .$$

Hence,

$$\alpha >> \gamma \qquad (A.3)$$

and

$$\theta >> \delta \ . \qquad (A.4)$$

From triangles CSO and CSP, it is apparent that

$$CS = CO \tan\alpha \qquad (A.5)$$

and

$$CP = CS/\tan\theta \ . \qquad (A.6)$$

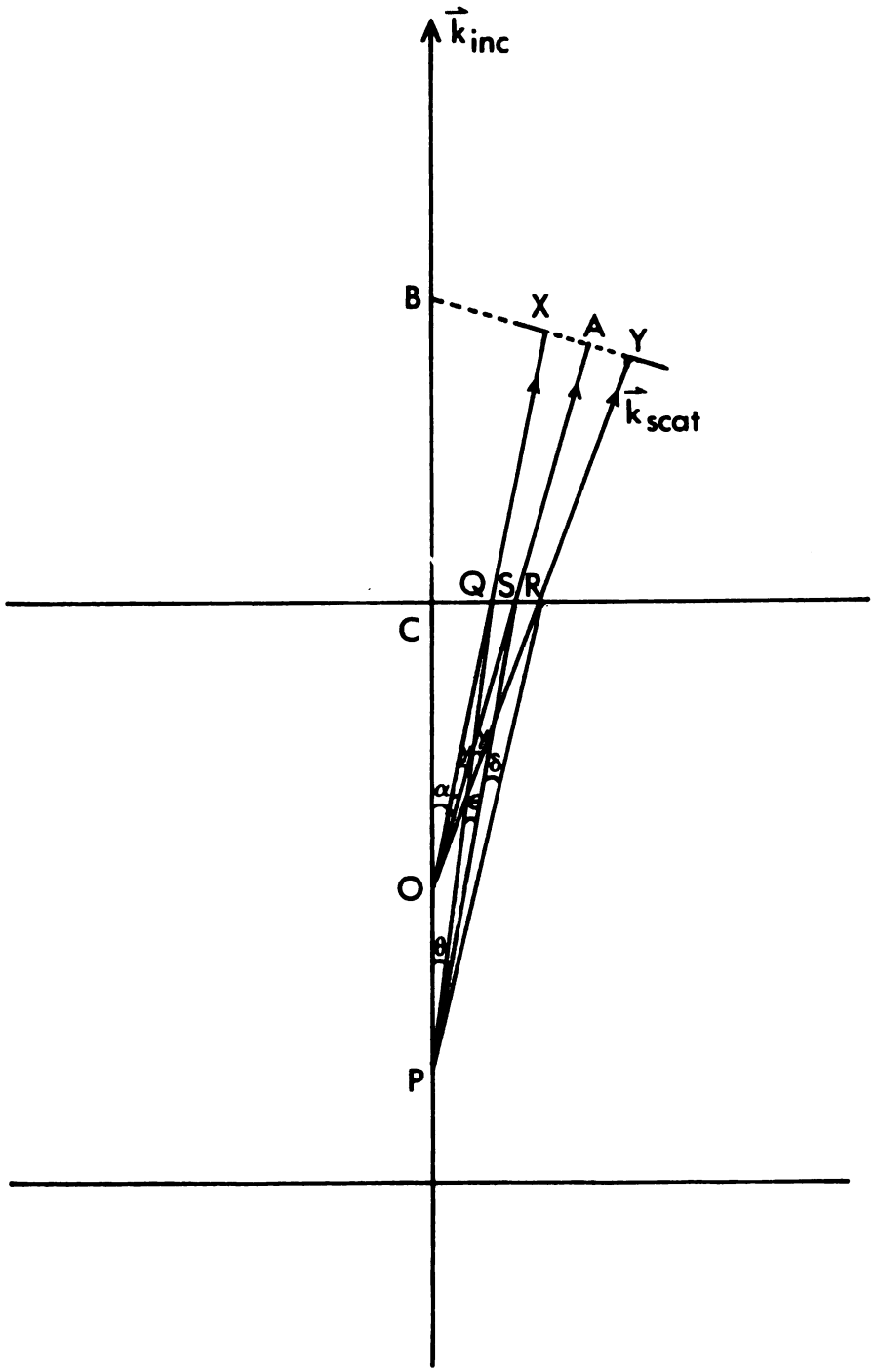

Figure A.2. Ray diagram for refraction correction.

Substituting equation (A.5) into equation (A.6) and with the aid of equation (A.2), it is found that

$$CP = CO\left[\frac{\sqrt{\langle n\rangle^2 - \sin^2\alpha}}{\cos\alpha}\right] \quad . \tag{A.7}$$

Furthermore, as is obvious from triangle CQO,

$$CQ = CO\,\tan(\alpha - \gamma) \quad . \tag{A.8}$$

Since

$$\tan(\theta - \epsilon) = CQ/CP \quad ,$$

it follows from equations (A.7) and (A.8) that

$$\epsilon = \theta - \tan^{-1}\left[\frac{\cos\alpha\,\tan(\alpha - \gamma)}{\sqrt{\langle n\rangle^2 - \sin^2\alpha}}\right] \quad . \tag{A.9}$$

By considering triangles CRP and CRO, the following can also be easily obtained:

$$\tan(\theta + \delta) = \frac{\cos\alpha\,\tan(\alpha + \gamma)}{\sqrt{\langle n\rangle^2 - \sin^2\alpha}}$$

or

$$\delta = \tan^{-1}\left[\frac{\cos\alpha\tan(\alpha + \gamma)}{\sqrt{\langle n\rangle^2 - \sin^2\alpha}}\right] - \theta \quad . \tag{A.10}$$

Adding equation (A.9) to equation (A.10) gives:

$$(\epsilon + \delta) = \tan^{-1}\left[\frac{\cos\alpha\,\tan(\alpha + \gamma)}{\sqrt{\langle n\rangle^2 - \sin^2\alpha}}\right] - \tan^{-1}\left[\frac{\cos\alpha\,\tan(\alpha - \gamma)}{\sqrt{\langle n\rangle^2 - \sin^2\alpha}}\right] \quad . \tag{A.11}$$

A Taylor series expansion of $\tan(\alpha + \gamma)$ yields:

$$\tan(\alpha + \gamma) = \tan\alpha + \gamma\sec^2\alpha + \gamma^2\sec^2\alpha\tan\alpha + \ldots \quad \text{(A.12)}$$

Since $\gamma << \alpha$ (see equation (A.3)), terms higher than the second in equation (A.12) can be neglected and hence,

$$\tan(\alpha + \gamma) = \tan\alpha + \gamma\sec^2\alpha = (\sin\alpha + \gamma/\cos\alpha)/\cos\alpha. \quad \text{(A.13)}$$

By the same token, it is found that

$$\tan(\alpha - \gamma) = \tan\alpha - \gamma\sec^2\alpha = (\sin\alpha - \gamma/\cos\alpha)/\cos\alpha. \quad \text{(A.14)}$$

Substituting equations (A.13) and (A.14) into equation (A.11) gives:

$$(\epsilon + \delta) = \tan^{-1}\left[\frac{\sin\alpha}{\sqrt{\langle n\rangle^2 - \sin^2\alpha}} + \frac{\gamma}{\cos\alpha\sqrt{\langle n\rangle^2 - \sin^2\alpha}}\right]$$

$$- \tan^{-1}\left[\frac{\sin\alpha}{\sqrt{\langle n\rangle^2 - \sin^2\alpha}} - \frac{\gamma}{\cos\alpha\sqrt{\langle n\rangle^2 - \sin^2\alpha}}\right]. \quad \text{(A.15)}$$

But,

$$\tan^{-1}\left[\frac{\sin\alpha}{\sqrt{\langle n\rangle^2 - \sin^2\alpha}} + \frac{\gamma}{\cos\alpha\sqrt{\langle n\rangle^2 - \sin^2\alpha}}\right] = \tan^{-1}\left[\frac{\sin\alpha}{\sqrt{\langle n\rangle^2 - \sin^2\alpha}}\right]$$

$$+ \frac{1}{\left[1 + \frac{\sin\alpha}{\langle n\rangle^2 - \sin^2\alpha}\right]} \cdot \frac{\gamma}{\cos\alpha\sqrt{\langle n\rangle^2 - \sin^2\alpha}} + O(\gamma'^2) + \ldots \quad \text{(A.16)}$$

and

$$\tan^{-1}\left[\frac{\sin\alpha}{\sqrt{\langle n\rangle^2 - \sin^2\alpha}} - \frac{\gamma}{\cos\alpha\sqrt{\langle n\rangle^2 - \sin^2\alpha}}\right] = \tan^{-1}\left[\frac{\sin\alpha}{\sqrt{\langle n\rangle^2 - \sin^2\alpha}}\right]$$

$$- \frac{1}{\left[1 + \frac{\sin\alpha}{\langle n\rangle^2 - \sin^2\alpha}\right]} \cdot \frac{\gamma}{\cos\alpha\sqrt{\langle n\rangle^2 - \sin^2\alpha}} + P(\gamma)^2 + \ldots \quad \text{(A.17)}$$

Terms higher than the second in equations (A.16) and (A.17) can again be neglected. Hence equation (A.15) reduces down to:

$$(\epsilon + \delta) = \frac{2\gamma}{\cos\alpha\sqrt{\langle n\rangle^2 - \sin^2\alpha}\left[1 + \frac{\sin^2\alpha}{\langle n\rangle^2 - \sin^2\alpha}\right]} = \frac{2\gamma\sqrt{\langle n\rangle^2 - \sin^2\alpha}}{\langle n\rangle^2 \cos\alpha}$$

or

$$\frac{2\gamma}{(\epsilon+\delta)} = \frac{\langle n\rangle^2 \cos\alpha}{\sqrt{\langle n\rangle^2 - \sin^2\alpha}} \quad . \tag{A.18}$$

Equation (A.18) takes care of the effect on the horizontal plane. It is apparent that the factor takes the value of $\langle n\rangle$ when normal incidence (i.e. when $\alpha = 0$) is achieved and is unity in the absence of the refracting sample. Since the photometer described in Chapter III restricts the scattered beam to be probed on the horizontal plane, the beam is always perpendicular to the vertical plane of the sample. Thus, for this plane, the error can be corrected for by a factor $\langle n\rangle$.

From the above considerations, the correction factor, C_n, for the effect due to refraction is therefore given by:

$$C_n = \frac{\langle n\rangle^3 \cos\alpha}{\sqrt{\langle n\rangle^2 - \sin^2\alpha}}$$

or

$$C_n = \frac{\langle n\rangle^2 \cos\alpha}{\sqrt{1 - \frac{\sin^2\alpha}{\langle n\rangle^2}}} \quad . \tag{A.19}$$

Volume Correction

Since the scattered light intensity is directly proportional to the scattering volume (see equation (2.50b)), any relative intensity measurements must be performed with

an identical volume in order to be meaningful. It can easily be visualized that probing the scattered intensity on a horizontal plane (see Chapter III) will involve a different scattering volume at a different scattering angle and thus, a correction must be applied to the measured intensity so that such an angular dependence of the volume can be taken into account.

In accord with the experimental set up described in Chapter III, the diameter of the incident beam (1 mm) is slightly smaller than the length of the entrance-rectangular slit of the light pipe (1.02 mm). Moreover, the scattered light perceived can be regarded as parallel having a width, W, equal to that of the slit. As a result, depending on the length and the mean refractive index of the sample, the scattering volume will assume several different shapes within the range of angles under study as follows:

Case I:- At a large real scattering angle, θ (or apparent angle, α), when both of the elliptical cut sections of the incident beam lie within the sample, the volume seen by the light pipe will be a slanting elliptical cylinder ABCD (Fig. A.3). By simple geometrical arguments, it is apparent that the volume, ABCD, is given by:

$$V_\theta = \pi r^2 (AD) \quad , \qquad (A.20)$$

where r is the radius of the incident beam. From the figure, it is also obvious that

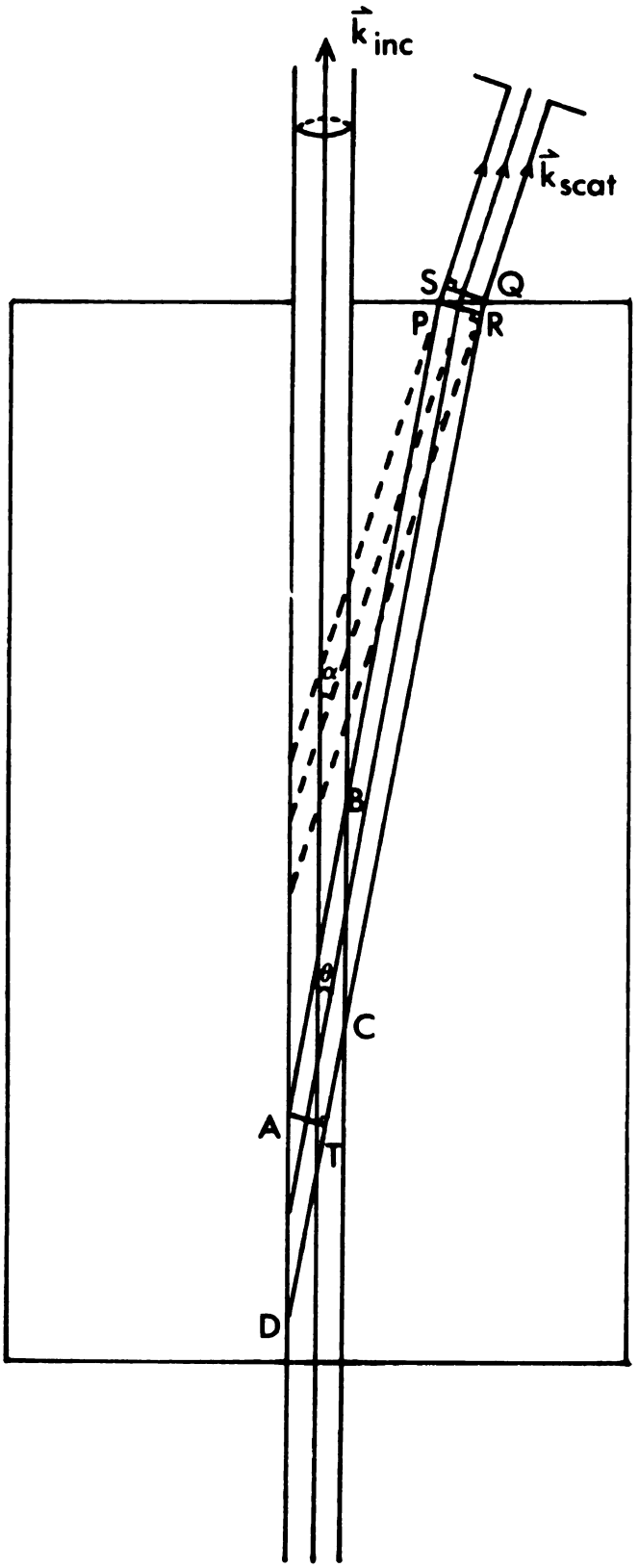

Figure A.3. Ray diagram for volume correction at large scattering angle.

$$AD = AT/\sin\theta = PR/\sin\theta \quad . \qquad (A.21)$$

The relationship between PR and the width of the perceived scattered beam, W, can be obtained by considering the triangles PRQ and PSQ as follows:

$$PR = PQ\cos\theta = SQ[\cos\theta/\cos\alpha] = W[\cos\theta/\cos\alpha] \quad .$$

Thus,

$$AD = W[\cos\theta/(\sin\theta\cos\alpha)],$$

and

$$V_\theta = \pi r^2 W[\cos\theta/(\sin\theta\cos\alpha)] \quad . \qquad (A.22)$$

Case II:- At a smaller real scattering angle, θ', the elliptical section, DC, (Fig. A.3) will cut the incident beam outside the sample. In this case, the scattering volume, $V_{\theta'}$, will be represented by ABCEFG as shown in Figure A.4-A and is given by:

$$V_{\theta'} = V_A - V_B \quad , \qquad (A.23)$$

where V_A is the volume bounded by ABHF with the incident beam and V_B the volume bounded by GCHE. Introducing the rectangular co-ordinates and denoting the distances from the entrance surface, FGHE, of the sample to the centers of the two ellipses, AIBJ and LGCE, by x_1 and x_2 respectively, it is seen that for any given z, points on the former ellipse can be described by:

$$x = mz + x_1 \quad , \qquad (A.24)$$

while those on the latter one satisfy:

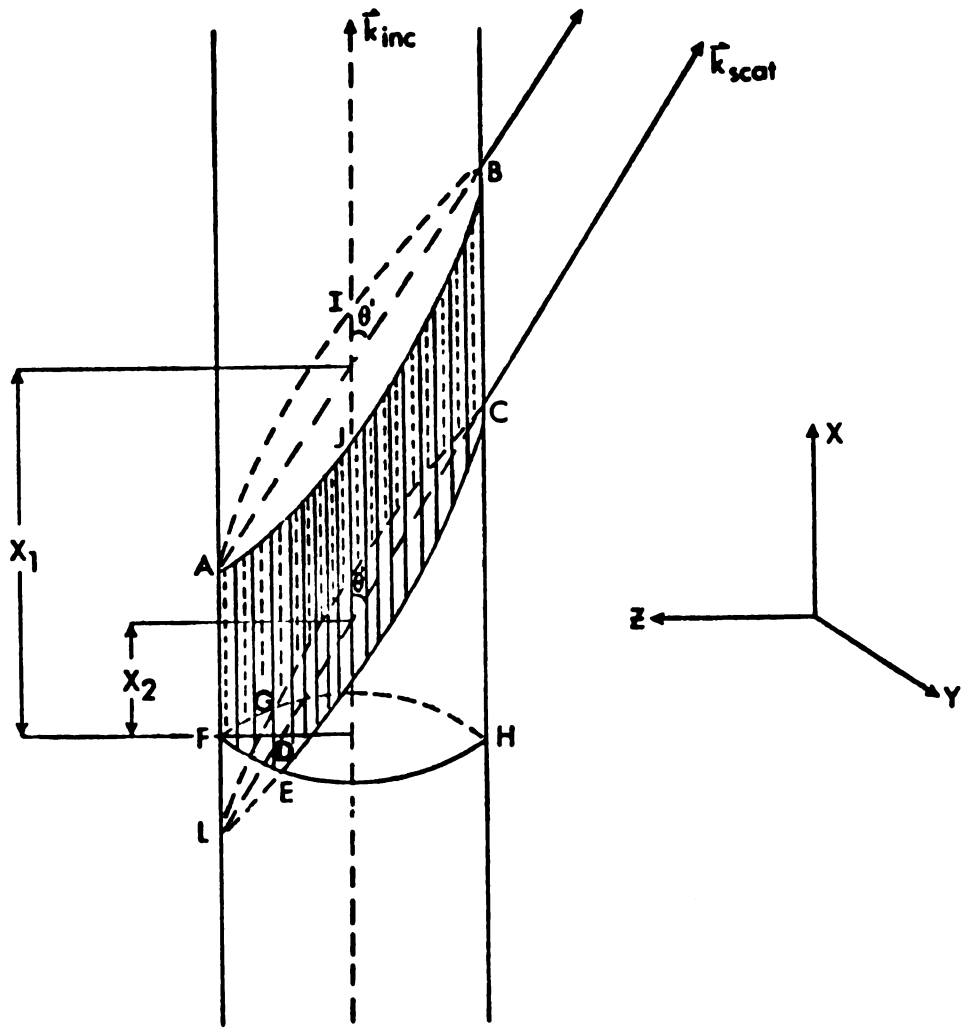

Figure A.4-A. Scattering volume at small scattering angle.

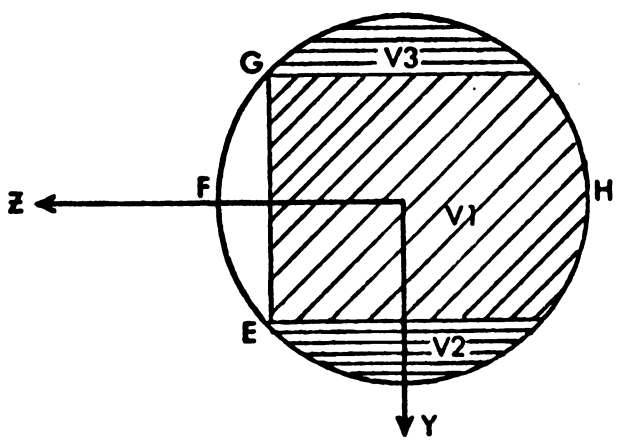

Figure A.4-B. Projection of scattering volume at small scattering angle.

$$x = mz + x_2 \quad , \tag{A.25}$$

where m is the slope of either AB or DC and

$$m = - \cot \theta' \quad . \tag{A.26}$$

The volume, V_A, is obviously equal to that of a circular cylinder with a height x_1 and is given by :

$$V_A = \pi r^2 x_1 \quad . \tag{A.27}$$

To compute V_B, it will be convenient to cosider the projection of GCED onto FGHE as shown in Figure A.4-B. From the figure, it is apparent that

$$V_B = V_1 + V_2 + V_3 \quad ,$$

or since V_2 and V_3 are symmetrical,

$$V_B = V_1 + 2V_2 \quad . \tag{A.28}$$

The volumes V_1 and $2V_2$ can be calculated as follows:

$$V_1 = \int_{-\sqrt{r^2-(\frac{x_2}{m})^2}}^{\sqrt{r^2-(\frac{x_2}{m})^2}} \int_{-\sqrt{r^2-y^2}}^{\frac{-x_2}{m}} (mz + x_2)\,dz\,dy$$

$$= - mr^2\tau + \frac{m}{3}\tau^3 - \frac{2x_2^2\tau}{m} + x_2 r^2 \gamma \quad , \tag{A.29}$$

and

$$2V_1 = 2\left[\int_{\sqrt{r^2-(\frac{x_2}{m})^2}}^{r} \int_{-\sqrt{r^2-y^2}}^{\sqrt{r^2-y^2}} (mz + x_2)\,dz\,dy\right]$$

$$= \pi r^2 x_2 - 2r^2 x_2 \gamma + \frac{2x_2^2\tau}{m} \quad , \tag{A.30}$$

where

$$\tau = \sqrt{r^2 - (x_2/m)^2}$$

$$\gamma = \sin^{-1}\left[\frac{\sqrt{r^2 - (x_2/m)^2}}{r}\right] \qquad (A.31)$$

and m is as defined in equation (A.26). Adding equations (A.29) and (A.30) yields:

$$V_B = \pi r^2 x_2 - r^2 x_2 \gamma - m r^2 \tau + \frac{m}{3}\tau^3 \ . \qquad (A.32)$$

Hence, from equations (A.23) and(A.27), the scattering volume, $V_{\theta'}$, is given by:

$$V_{\theta'} = \pi r^2 (x_1 - x_2) + (r^2 x_2 \gamma + m r^2 \tau - \frac{m}{3}\tau^3) \ , \qquad (A.33)$$

where x_1 and x_2 can be easily shown to be related to the length, ℓ, the mean refractive index, $\langle n \rangle$, of the sample and the width, W, of the entrance slit of the light pipe by the following equations:

$$x_1 = \ell - \frac{\langle n \rangle \ell \cos\theta'}{2\cos\alpha'} + \frac{W\cos\theta'}{2\sin\theta'\cos\alpha'}$$

$$x_2 = \ell - \frac{\langle n \rangle \ell \cos\theta'}{2\cos\alpha'} - \frac{W\cos\theta'}{2\sin\theta'\cos\alpha'} \ . \qquad (A.34)$$

Case III:- At an even smaller real scattering angle, θ'', one will encounter the situation when both the elliptical sections, AIBJ and LGCE (Fig. A.4-A), cut the incident beam beyond the entrance surface, FGHE, of the sample. Only the case when the intersections of both ellipses with the entrance surface lie on $z > 0$ (Fig. A.4-A) will be of

importance to the experiment described in Chapter III, for the other case, when the intersection of LGCE with the entrance surface lies on $z \leq 0$ occurs at an apparent scattering angle, $\alpha"'$, much smaller than 1^0 and is practically unobtainable with the instrument.

In the same way as V_B was obtained (equations (A.29) and (A.30)), the scattering volume, $V_{\theta"}$, can be shown to be given by:

$$V_{\theta"} = (\pi r^2 x_1 - r^2 x_1 \gamma_1 - mr^2 \tau_1 + \frac{m}{3}\tau_1^3) - (\pi r^2 x_2 - r^2 x_2 \gamma_2 - mr^2 \tau_2 + \frac{m}{3}\tau_2^3) , \quad (A.35)$$

where

$$m = - \cot \theta"$$

$$\tau_i = \sqrt{r^2 - (x_i/m)^2}$$

$$\gamma_i = \sin^{-1}\left[\frac{\sqrt{r^2 - (x_i/m)^2}}{r} \right]$$

and x_1 and x_2 are as defined in equation (A.34) with θ' and α' replaced by $\theta"$ and $\alpha"$ respectively.

From the above considerations, it follows that there will be three different volume correction factors, namely C_{V_θ}, $C_{V_{\theta'}}$, $C_{V_{\theta"}}$. Since the scattering volume seen at 90^0 is a constant:

$$V_{90} = \pi r^2 w,$$

it can be used as a reference for V_θ, $V_{\theta'}$, and $V_{\theta"}$. Thus, one obtains:

$$C_{V_\theta} = V_{90}/V_\theta = \cos\theta/(\sin\theta\cos\alpha)$$

$$C_{V_{\theta'}} = V_{90}/V_{\theta'} = \pi r^2 W/V_{\theta'}$$

$$C_{V_{\theta''}} = V_{90}/V_{\theta''} = \pi r^2 W/V_{\theta''} \quad . \qquad (A.36)$$

Reflection Correction

The reflection of the incident and the scattered light at the interfaces of the sample renders the measured scattered intensity lower than its actual value, $I(s)$. To correct for this effect, let β be the angle the $\bar{E}_s$ vector of the scattered beam makes with the plane of incidence (i.e. xy plane) at the exit surface of the sample as shown in Figure A.5. It follows then

$$\frac{I(s)^{\parallel}}{I(s)^{\perp}} = \frac{J_s \cos^2\beta}{J_s \sin^2\beta} = \cot^2\beta \quad , \qquad (A.37)$$

where J_s is the amount of energy in the scattered wave incident on a unit area of the boundary per second and the superscripts, $\parallel$ and $\perp$, refer to the components parallel and perpendicular to the plane of incidence respectively. Denoting the transmissivity at the exit surface of the sample by T_e, the ratio of the two components of the scattered intensity is also given by:

$$\frac{I(s)^{\parallel}}{I(s)^{\perp}} = \frac{T_e^{\perp} I_{meas}(s)^{\parallel}}{T_e^{\parallel} I_{meas}(s)^{\perp}} \quad . \qquad (A.38)$$

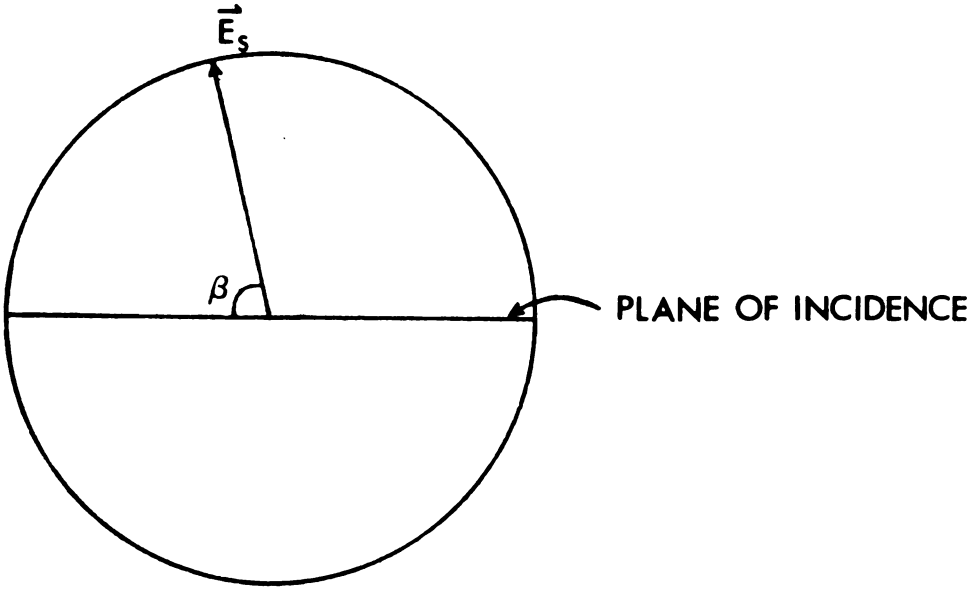

Figure A.5. Diagram for reflection correction.

Here $I_{meas}(s)$ is the measured scattered intensity.

Since the incident laser beam used for the experiment (see Chapter III) is vertically polarized, therefore, by definition,

$$\frac{I_{meas}(s)^{\parallel}}{I_{meas}(s)^{\perp}} = \rho_v \quad , \tag{A.39}$$

where ρ_v is the depolarization ratio of the sample. Combining equations (A.37), (A.38), and (A.39) gives:

$$\cot^2\beta = \rho_v \frac{T_e^{\perp}}{T_e^{\parallel}} \quad ,$$

or since the sum of the reflectivity, R_e, and the transmissivity, T_e, is unity,

$$\cot^2\beta = \rho_v \frac{(1 - R_e^{\perp})}{(1 - R_e^{\parallel})} \quad . \tag{A.40}$$

Hence,

$$\sin^2\beta = \frac{1}{1 + \rho_v \left(\frac{1 - R_e^{\perp}}{1 - R_e^{\parallel}}\right)}$$

and

$$\cos^2\beta = \frac{\rho_v \left(\frac{1 - R_e^{\perp}}{1 - R_e^{\parallel}}\right)}{1 + \rho_v \left(\frac{1 - R_e^{\perp}}{1 - R_e^{\parallel}}\right)} \quad . \tag{A.41}$$

Following Born and Wolf,[47] the total reflectivity, $R_e(\theta)$, of the scattered light at a real scattering angle θ is then given by:

$$R_e(\theta) = \cos^2\beta R_e^{\parallel}(\theta) + \sin^2\beta R_e^{\perp}(e) \quad , \qquad (A.42)$$

where

$$R_e^{\parallel}(\theta) = \frac{\tan^2(\theta - \alpha)}{\tan^2(\theta + \alpha)}$$

and

$$R_e^{\perp}(\theta) = \frac{\sin^2(\theta - \alpha)}{\sin^2(\theta + \alpha)} \quad . \qquad (A.43)$$

It is obvious that $R_e^{\perp}(\theta) > R_e^{\parallel}(\theta)$ and since the depolarization ratios of the samples under study are much smaller than unity (e.g. see Chapter IV), it can easily be seen that

$$\rho_v\left(\frac{1 - R_e^{\perp}}{1 - R_e^{\parallel}}\right) << 1 \quad . \qquad (A.44)$$

Therefore, from equation (A.41), it follows that

$$\sin^2\beta \approx 1$$

and

$$\cos^2\beta \approx 0 \quad .$$

Hence, the reflectivity in equation (A.42) becomes:

$$R_e(\theta) \approx R_e^{\perp}(\theta) = \sin^2(\theta - \alpha)/\sin^2(\theta + \alpha)$$

or

$$R_e(\theta) \approx \sin^2(\alpha - \theta)/\sin^2(\theta + \alpha) \quad . \qquad (A.45)$$

Thus, the factor by which the measured scattered intensity

must be multiplied in order to account for the reflection of the scattered light at the exit surface of the sample is:

$$\frac{1}{1 - R_e(\theta)} \quad . \tag{A.46}$$

The reflectivity of the incoming beam incident normally on the entrance surface of the sample, $R_i(0)$, is independent of the scattering angle and is given by:

$$R_i(0) = \left(\frac{\langle n\rangle - 1}{\langle n\rangle + 1}\right)^2 \quad , \tag{A.47}$$

where $\langle n\rangle$ is again the mean refractive index of the sample. Hence, the total correction factor becomes:

$$\frac{1}{(1-R_i(0))(1-R_e(\theta))} \quad . \tag{A.48}$$

Since it is the relative scattered intensity that is being examined, it will be more convenient to normalize the correction factor at any scattering angle, θ, to that at 0^0 (i.e. the factor for the directly transmitted beam). Thus,

$$C_R = \frac{(1 - R_i(0))(1 - R_i(0))}{(1 - R_i(0))(1 - R_e(\theta))} =$$

$$\frac{4\langle n\rangle}{(\langle n\rangle + 1)^2\left[1 - \frac{\sin^2(\alpha - \theta)}{\sin^2(\theta + \alpha)}\right]} \quad . \tag{A.49}$$

Attenuation Correction

In view of the opacity of the 0.03% and the 0.05% PS/PMMA blends, it is also appropriate to correct for the

effect due to attenuation within these two samples. Following equation (A.1), if the attenuation correction factor is denoted by C_{att}, the actual scattered intensity, $I(s)$, can be obtained from the measured value, $I_{meas}(s)$, by:

$$I(s) = I_{meas}(s) \times C_n \times C_V \times C_R \times C_{att} \quad . \quad (A.50)$$

Assuming the Lambert type of attenuation within the sample, the incident intensity, I_P^{inc}, at a scattering element P within the scattering volume, ABCD (Fig. A.6), which is at a distance x from the entrance surface, FH, of the sample is given by:

$$I_P^{inc} = I_0 \exp(-\tau x) \quad , \quad (A.51)$$

where I_0 is the intensity of the incident beam before transversing the sample which has a turbidity, τ. A portion, f, of this intensity will be scattered, however, along PQ whereupon attenuation again occurs. If PQ represents a path length y, the intensity at Q, where the scattered light leaves the sample, is therefore:

$$I_Q^{scat} = f\, I_P^{inc} \exp(-\tau y) = f\, I_0 \exp[-\tau(x+y)]$$

or since

$$y = (\ell - x)\sec\theta$$

$$I_Q^{scat} = f\, I_0 \exp\{-\tau[x(1 - \sec\theta) + \ell \sec\theta]\} \quad . \quad (A.52)$$

The measured intensity, $I_{meas}(s)$, must be represented by the average of I_Q^{scat} over all possible path lengths of $(x + y)$. Thus,

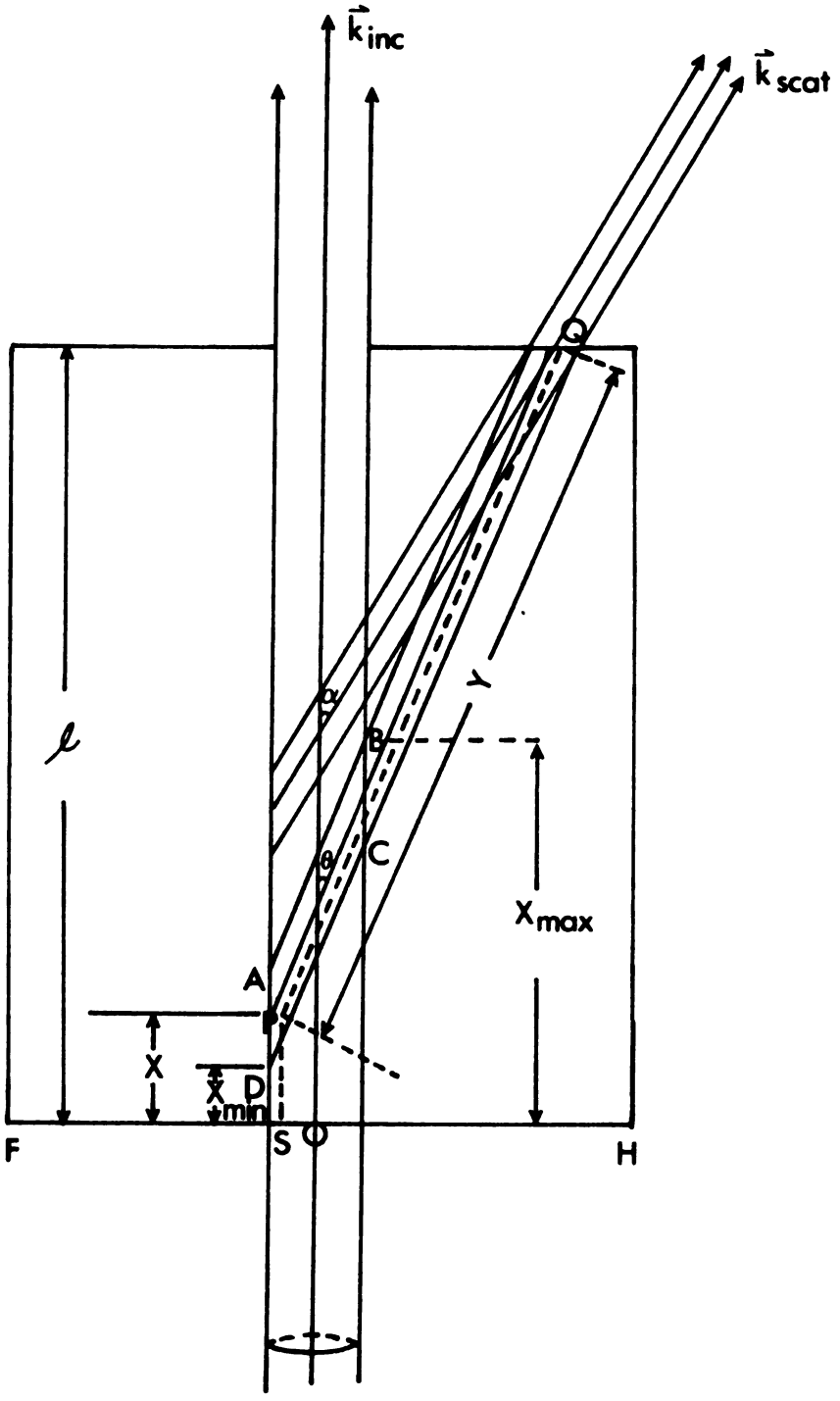

Figure A.6. Ray diagram for attenuation correction.

$$I_{meas}(s) = f\, I_0 \langle \exp\{-\tau[x(1-\sec\theta) + \ell \sec\theta]\} \rangle_x \quad \text{(A.53)}$$

An exact evaluation of the average in the above equation will be very difficult because of the slanting nature of the scattering volume and hence the complexity of the weight function that has to be used. A calculation of the exponential function in equation (A.52) over the range of x (i.e. between x_{min} and x_{max}) in the scattering volume shows that it varies by at most ±3% from the simple average of its extremes (e.g. at large θ). Since the function is varying very smoothly and monotonically over the range of x and the weight function is almost as mild-mannered, the exactly calculated average (equation (A.53)) may be expected to lie well within the extremes. In fact, in the case where the spread of the exponential function between the two extremes of x is largest, the weight function is seen to be symmetric and thus will have the least effect in shifting the exact average away from the average of the extremes. Hence, the uncertainty involved in taking the average of the extremes as the exact one may, with confidence, be estimated to be less than 1% . Furthermore, since calculations also show the difference between

$$\exp\{-\tau[\langle x \rangle(1 - \sec\theta) + \ell \sec\theta]\}$$

and the average of the extremes over the regions investigated to be in the order of 0.1% or less, it follows then:

$$\langle \exp\{-\tau[x(1 - \sec\theta) + \ell \sec\theta]\}\rangle_x \approx$$

$$\exp\{-\tau[\langle x\rangle(1 - \sec\theta) + \ell \sec\theta]\} \quad . \qquad (A.54)$$

From Figure A.6, $\langle x\rangle$ is the distance of the center of the scattering volume from the entrance surface, FH, of the sample and is given by:

$$\langle x\rangle = \ell\left(1 - \frac{\langle n\rangle \cdot \cos\theta}{2\cos\alpha}\right) \quad , \qquad (A.55)$$

where $\langle n\rangle$ is the mean refractive index of the sample, and θ and α are the real and apparent scattering angles respectively. Thus, equation (A.53) can be written as:

$$I_{meas}(s) = f\, I_0 \exp\{-\tau\ell[(1 - \frac{\langle n\rangle\cos\theta}{2\cos\alpha})(1-\sec\theta)+\sec\theta]\}$$

$$= f\, I_0 \exp\{-\tau\ell[1 + \frac{\langle n\rangle(1 - \cos\theta)}{2\cos\alpha}]\} \quad . \qquad (A.56)$$

Since in the absence of any attenuation, the scattered intensity is equal to $f\, I_0$, it follows then the attenuation correction factor,

$$C_{att} = f\, I_0/I_{meas}(s) \approx \exp\{-\tau\ell[1+ \frac{\langle n\rangle(1 - \cos\theta)}{2 \cdot \cos\alpha}]\}. \qquad (A.57)$$